Optical Properties of Spherical Silica-Based Greenhouse Coatings: Comparing Experimental Measurements with Monte Carlo Simulations

Masters Thesis

R.M.(Robert) Ingham

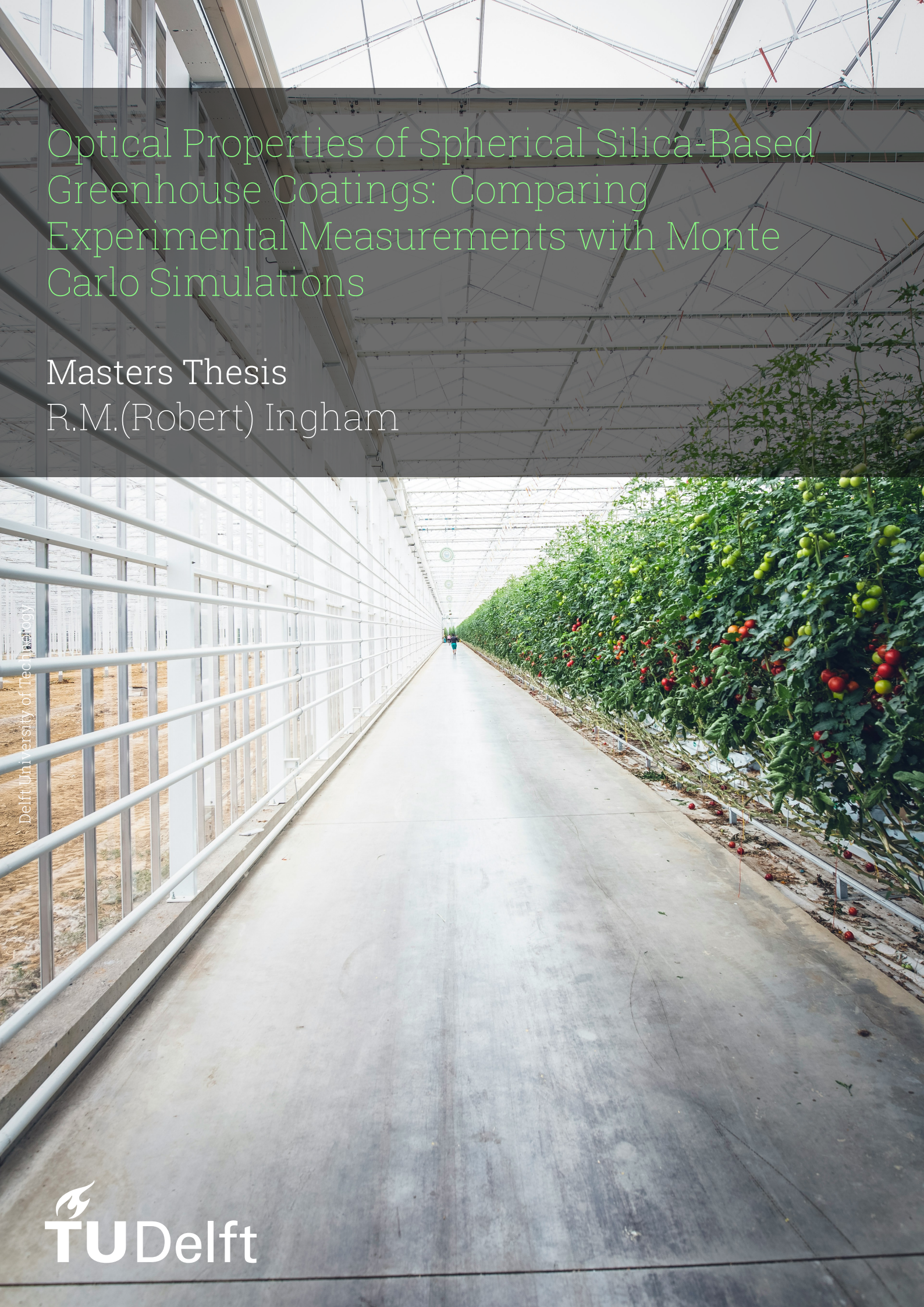

TU Delft

Optical Properties of Spherical Silica-Based Greenhouse Coatings: Comparing Experimental Measurements with Monte Carlo Simulations

by

R.M.(Robert) Ingham

Student Name	Student Number
Robert Martijn Ingham	4962613

Daily Suupervisor:	Dr. E.(Erik) van der Kolk
2nd Examiner:	Prof. Dr. P.(Pieter) Dorenbos
3rd Examiner:	Dr. M.(Marlies) Goorden
Faculty:	Faculty of Applied Physics, Delft

Cover: Greenhouse in Kulmbacher Land, Upper Franconia, Bavaria, Germany. Picture obtained from [1].

TU Delft

Preface

As I reach the culmination of my Master's thesis project, eight months from the day I began, I would like to express my deepest gratitude to those who made this journey possible.

First and foremost, I want to thank my daily supervisor, Erik. Your open-door policy and willingness to engage in lengthy discussions, without ever once indicating that you didn't have time, made this process incredibly smooth and rewarding for me.

I am also immensely grateful to the Luminescence Materials group. Having completed my Bachelor's thesis with the same group, I was thrilled to return for my Master's. Johan, thank you for working your magic on the experimental setups that constantly needed fixing. And Pieter, thank you for hosting a wonderful barbecue at the end of the year, which was a perfect closing event for me. My thanks also go to all the PhD candidates—the lunches and our sometimes unnecessarily long coffee or tea breaks made the days fly by, sometimes too quickly. Special thanks to Casper, whose ”hobbying” phase often led to distractions in the student area. However, your fun discussions and readiness to help always made up for it. A particular thank you goes to Justin for sharing his knowledge on the experimental setups and assisting whenever necessary.

I would also like to thank the other students I had the pleasure of working with. Giles, sharing the student room with you for six months was a joy; your company made the time enjoyable, even when it was just the two of us. Isaak, who I convinced to join us despite being from a different group—the ping pong matches were a great distraction, even though you won most of them.

My gratitude also extends to Fotoniq, especially Giacomo and Chiara, for sharing their expertise and knowledge whenever needed.

Lastly, I want to express my heartfelt gratitude to my parents. Your emotional support and financial assistance made this journey a smooth one, even during my busiest times when I was not the best at communicating.

Thank you all.

R.M.(Robert) Ingham
Delft, June 2024

Abstract

This thesis investigates the optical properties of monodisperse spherical silica-based coatings through experimental measurements and Monte Carlo ray tracing simulations. The aim is to compare these experiments and simulations to identify potential improvements. The study focuses on quantifying diffusivity and transmittance, related to Hortiscatter (HS) and Hemispherical Light Transmission (HLT), respectively, which are essential for optimizing greenhouse light conditions to enhance plant growth.

For HLT, simulations and measurements aligned more closely for low-scattering coatings, especially with smaller particles (160 nm and 400 nm), often showing less than 1% difference. However, for high-scattering coatings with larger particles, the difference was much larger, reaching up to 9%. This discrepancy highlights the possible importance of surface scattering and potential measurement setup limitations, such as the beam size being too small.

Significant discrepancies were observed between measured and simulated HS values, with measured values consistently higher by 5% to 80%, likely due to simulations not accounting for surface roughness. Smaller particles showed similar wavelength dependence of HS between simulation and measurement, while larger particles (5 µm) indicated the presence of complex scattering interactions that simulations did not account for.

Future work should refine simulation models to include surface roughness and obtain precise input parameters, such as refractive indices, to improve accuracy. Enhancing experimental setups, for example by reducing the signal-to-noise ratio, will also ensure more reliable measurements. This research offers valuable insights into optimizing greenhouse coatings, demonstrating the potential of theoretical models to predict practical outcomes under specific conditions. Continued advancements in simulation and experimental methodologies are crucial for effective greenhouse design to enhance plant growth.

Contents

Nomenclature

Abbreviations

Abbreviation	Definition
CV	Coefficient of variation
DI water	Deionized water
HLT	Hemispherical Light Transmission
HS	Hortiscatter
PAR	Photo-synthetically Active Radiation
TDF	Transmittance Distribution Function
TDF_s	Sample Transmittance Distribution Function
TDF_r	Reference Transmittance Distribution Function
TDF_L	Lambertian Transmittance Distribution Function

Symbols

Symbol	Definition	Unit
A_λ	Plant Efficiency Spectrum	[-]
dA_0	sample acceptance area detector	[m]
$dA_\perp$	perpendicular sample acceptance area detector	[m]
d	particle diameter	[nm]
d_p	chosen particle diameters	[nm]
E	Electric Field	[NC^{-1}]
H	Magnetic Field	[T]
$I_s(\theta)$	Angle dependent Intensity of Sample	[W/m^2]
$I_r(\theta)$	Angle dependent Intensity of Reference	[W/m^2]
k	Extinction coefficient	[-]
n	Refractive Index	[-]
$n*$	Complex Refractive Index	[-]
r	Position Vector	[m]
T_L	Perpendicular Transmission	[%]
T_λ	Wavelength Dependent Transmission	[%]
$T_{\phi,\theta}$	Angle Dependent Transmission	[%]
$T_{\lambda,\phi,\theta}$	Angle & Wavelength Dependent Transmission	[%]
t	Time	[s]
t_{dry}	Dry coating thickness	[μm]
t_{wet}	Wet coating thickness	[μm]
$vol\%$	Volume percentage	[%]
$wt\%$	Weight percentage	[%]
θ	Angle of Incidence	[deg]
θ_C	Critical Angle	[deg]
θ_T	Angle of Transmission	[deg]
ϕ	Hemispherical Orientation	[deg]
ω	Angular Frequency	[deg/s]
σ_{sca}	Scatter Cross Section	[cm^2]
σ_{abs}	Absorption Cross Section	[cm^2]

Symbol	Definition	Unit
λ	Wavelength	[nm]

1

Introduction

The global population is on the rise and is expected to increase by nearly 2 billion persons in the next 30 years [2]. This increase in population is accompanied by a rise in food demand, projected to increase by 35% to 56% [3]. To meet this demand, innovative methods need to be developed to increase food production. One such method is by increasing the plant growth per area in greenhouses. For example, this can be done by applying a coating to the glass of existing greenhouses that diffuses more sunlight. It has been shown that more diffuse light can penetrate more deeply into the crop, thus increasing plant yield [4][5]. The light of importance is often called photosynthetically active radiation (PAR), which is defined as the wavelength range of visible light between 400 and 700 nm. PAR light is proven to play a critical role in maximizing plant yield [6][7]. Therefore, when implementing a diffuse coating, it is crucial that the transmittance of PAR light is not significantly decreased.

Two metrics used to quantify the interaction of PAR light on coatings are Hemispherical Light Transmission (HLT) and Hortiscatter (HS), which respectively give values for the amount of transmission and diffusive scattering of a certain coating. These metrics, defined by the Nederlandse Normalisatie Instituut (NEN) in their standard NEN 2675 [8], are designed to evaluate the performance of greenhouse coatings. While more diffuse light is generally beneficial for plant growth, excessive scattering can result in light scattering out of the greenhouse, thus decreasing transmission. Therefore, the challenge is to find an optimal balance between diffusivity (HS) and transmittance (HLT) to achieve the greatest increase in plant yield.

Fotoniq, a company based in Delft, specializes in horticultural spray coatings that enhance diffusivity without losing grow light. The Luminescence Materials (LM) group and Fotoniq collaborate extensively to research and develop coatings that improve greenhouse yield. The coatings under investigation utilize scatter particles dispersed in a polymer. Parameters such as the particle size, the particle-to-polymer ratio, and the coating thickness significantly influence light behavior, leading to an interest in finding optimal coating compositions.

In the past, computer simulations have been conducted using LightTools software, which employs Monte Carlo ray tracing combined with Mie theory to predict how light interacts with spherical scatter particles. From this, the behavior of certain coatings and their impact on light transmission and scattering was analyzed. Using an optimization process combined with the software, it was found that under certain conditions, a theoretical increase of 10% in crop yield is achievable [9]. While this is a promising result, there was a lack of experimental evidence on the accuracy of the simulations. To be able to use simulations as a predictive manner in coating optimization, the overlap between measurements and simulations of certain coatings needs to be explored.

The main research objective of this thesis is therefore: How well do simulations and measurements compare for self-made particle-based coatings? In this thesis, coatings will be made containing spherical silica particles embedded in a polymer. Multiple coatings will be produced, varying the particle size and coating thickness. The diffusivity and transmittance, defined by HS and HLT, will be simulated as well as measured using two in-house experimental setups. From this, the overlap between

measurements and simulations will be explored.

The structure of this thesis will start of in chapter 2 with relevant theory such as optics at interfaces, Mie-theory, and light properties for greenhouses. This will be followed by Chapter 3 including the methods used starting with the computational method showing the structure of the model and how HLT and HS are simulated. Afterwards, the optimization of the physical HS setup will be explained as well as how the final HS setup and the used HLT setup work. Lastly the coating production optimisation will be shown as well as how the coatings were produced. In the following chapter, the results of the simulations and measurements are given, where it was found that measurements expect much larger scattering, raising a question about the accuracy of the simulations. These results are discussed in chapter 5 which is followed by a short conclusion in the final chapter on how well measurements and simulations of HS and HLT compare.

2 Theory

2.1. Optics at Interfaces

The interaction of light with glass surfaces is central to understanding the optical properties of materials. This subsection will go over some foundational laws of optics, using electromagnetic principles from Zangwill's work [10].

2.1.1. Snell's Law

When light encounters a boundary between two media, its direction can change, leading to reflection and refraction. The angle of incidence (θ_i) is equal to the angle of reflection (θ_r), and the refracted light follows Snell's Law:

$$n_1 \sin(\theta_i) = n_2 \sin(\theta_t), \tag{2.1}$$

Here, n_1 and n_2 are the refractive indices of the respective media. When light passes from a denser to a rarer medium ($n_1 > n_2$), and the incidence angle exceeds the critical angle (θ_c), total internal reflection occurs, described by:

$$\theta_c = \arcsin\left(\frac{n_2}{n_1}\right). \tag{2.2}$$

2.1.2. Electromagnetic Nature of Light

Light, an electromagnetic wave, is characterized by its electric (E) and magnetic (H) field components. These fields oscillate perpendicularly to each other and to the direction of wave propagation and can be described mathematically as:

$$E(r,t) = E\exp(i(k \cdot r - \omega t)), \tag{2.3}$$

$$H(r,t) = H\exp(i(k \cdot r - \omega t)), \tag{2.4}$$

where E and H represent the magnitudes of the electric and magnetic fields, r is the position vector, k is the wave vector indicating the direction of propagation and the wavenumber, t represents time, and ω is the angular frequency of the wave. These fields interact with materials in ways described by Snell's Law and the Fresnel equations.

2.1.3. Fresnel Equations

The Fresnel equations are pivotal in determining how an incident EM wave's polarization has an effect on the exact behavior at surface interactions.

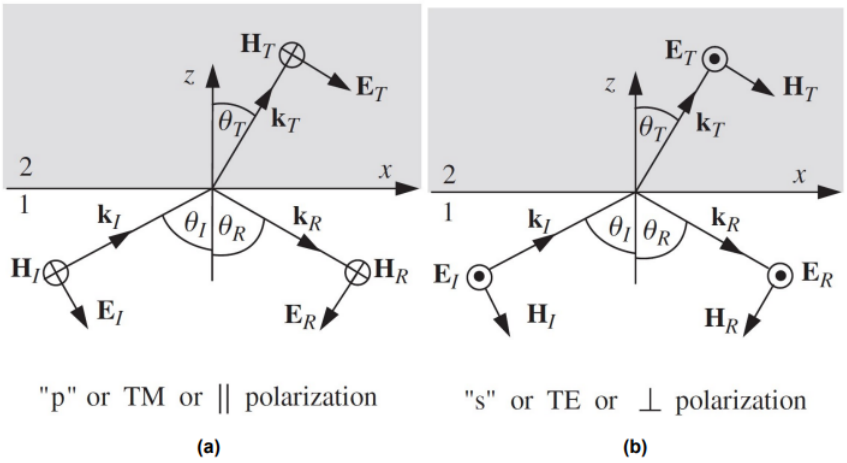

Figure 2.1: Both figures show two media, labeled as 1 and 2. Incident light enters with wave vector k_I and angle of incidence θ_I. It is reflected with wave vector k_R and angle of reflection θ_R, while also being transmitted with wave vector k_T and angle of transmission θ_T. (a) For a p-polarized wave, the electric field $\mathbf{E}$ is oriented parallel to the plane of incidence, while the magnetic field $\mathbf{H}$ is oriented perpendicular to the plane of incidence (into the paper). (b) For an s-polarized wave, $\mathbf{E}$ is oriented perpendicular to the plane of incidence (out of the paper), while $\mathbf{H}$ is oriented parallel to the plane of incidence. This figure has been obtained from [10].

These modifications can be inferred from the geometry shown in Figure 2.1 from Zangwill's book, where the incident light is polarized into two components: p-polarized, where the electric field oscillates in the incidence plane, and s-polarized, where it oscillates perpendicular to this plane.

For p- and s-polarized light, the reflection coefficients at an interface are respectively given by:

$$r_p = \frac{n_1 \cos(\theta_i) - n_2 \cos(\theta_t)}{n_1 \cos(\theta_i) + n_2 \cos(\theta_t)}, \tag{2.5}$$

$$r_s = \frac{n_1 \cos(\theta_t) - n_2 \cos(\theta_i)}{n_1 \cos(\theta_t) + n_2 \cos(\theta_i)}, \tag{2.6}$$

Similarly, the transmission coefficients for p- and s-polarized light are given by:

$$t_p = \frac{2n_1 \cos(\theta_i)}{n_1 \cos(\theta_i) + n_2 \cos(\theta_t)}, \tag{2.7}$$

$$t_s = \frac{2n_1 \cos(\theta_i)}{n_1 \cos(\theta_t) + n_2 \cos(\theta_i)}, \tag{2.8}$$

where t_p and t_s are the transmission coefficients for p- and s-polarized light, respectively. These coefficients describe the ratio of the transmitted electric field's amplitude to that of the incident field, providing a measure of how much light is transmitted through the interface.

By examining the polarization changes of reflected light across various incident angles, and utilizing the Fresnel equations, one can extract the refractive indices of unknown media. This analytical approach forms the basis of ellipsometry, a non-destructive optical technique used to ascertain the optical constants of a material, including complex refractive index and film thickness.

2.1.4. Complex Refractive Index and Extinction Coefficient

The comprehensive understanding of light interaction with materials necessitates considering not only the refractive index n, but also the material's ability to absorb light, quantified by the extinction coefficient k, in the complex refractive index $n^* = n + ik$.

The addition of k to the refractive index to form $n^* = n + ik$ does not change the form of Snell's Law or the Fresnel equations but extends their application to include the effects of material absorption. This reflects a more comprehensive understanding of how light interacts with media, particularly in scenarios where absorption is non-negligible. While the formulas are technically unchanged, their interpretation becomes more complex due to the need to consider the absorption (imaginary component) effects.

2.1.5. Lorentz-Lorentz relations

When a material has a porous structure, this has an effect on the refractive index. The Lorentz-Lorentz relations relate the microscopic structure and polarizability of a material to its macroscopic refractive index [11]. In the case the pore size is smaller than the wavelength of light, the following formulas can be used:

$$f(n) = pf(n_2) + (1-p)f(n_1) \tag{2.9}$$

$$f(n) = \frac{n^2 - 1}{n^2 + 2} \tag{2.10}$$

Here n_1 is the refractive index of the bulk material, n_2 is the refractive index of the material inside the pores, and finally p is the porosity of the medium which can be found in equation 2.11 below.

$$p = 1 - \frac{\rho}{\rho_0} \tag{2.11}$$

Here ρ_0 is the density of the non-porous material and ρ is the density of the same material with pores.

2.2. Mie Theory

Until now only surface interactions of light have been discussed. However to understand and predict how light will interact with certain particles, and not only surfaces, it is important to expand the current theory. Mie theory is the classical problem for light scattering on a spherical particle [12] [13] and is named after Gustav Mie who first published his paper on the scattering of an electromagnetic wave on a sphere in 1908 [14]. Mie theory describes scattering and absorption of harmonic plane waves of on a spherical particle.

Using the wave number of the incident wave on the outside of the particle k_e (external field), one can find the scatter and absorption probabilities as their corresponding cross sections with the following formulas taken from [15].

$$\sigma_{\text{sca}} = \frac{2\pi}{k_e^2} \sum_{l=1}^{\infty} (2l+1) \left(|a_l|^2 + |b_l|^2 \right) \tag{2.12}$$

$$\sigma_{\text{abs}} = \frac{2\pi}{k_e^2} \sum_{l=1}^{\infty} (2l+1) \left[\text{Re}\left(a_l + b_l\right) - \left(|a_l|^2 + |b_l|^2 \right) \right] \tag{2.13}$$

Where a_l and b_l are known as the "Mie coefficients" which depend on the the wave number, the dielectric constant of the medium and of the spherical particle and the particle radius. These coefficients are rather complex to calculate and make use of for example Riccati–Bessel functions. The full equations needed can be found in [15].

In Mie theory, the angular distribution of scattered light, or the scattering phase function, is calculated using the Mie coefficients a_l and b_l. The intensity of light scattered at a particular angle θ is influenced by the magnitude of these coefficients, which represent the contribution of each spherical harmonic to the scattering process. The scattering intensity pattern is often complex, with peaks and troughs resulting from the constructive and destructive interference of waves:

$$I(\theta) \propto \left| \sum_{l=1}^{\infty} \frac{2l+1}{l(l+1)} (a_l \pi_l(\cos\theta) + b_l \tau_l(\cos\theta)) \right|^2 \tag{2.14}$$

Here, π_l and τ_l are the angle-dependent scattering functions, related to the associated Legendre polynomials. The detailed calculation of these angular distributions is a non-trivial task, involving special functions and the extensive series expansion dictated by Mie theory. For a comprehensive derivation and discussion of the scattering phase function, the reader is referred to [16].

Mie theory represents a general framework for understanding light scattering by particles of any size, bridging the gap between the Rayleigh scattering regime, applicable to particles much smaller than the wavelength of light, and the geometric scattering regime, relevant for much larger particles. It encompasses the size parameter's entire spectrum, providing a continuous transition from the wave-like behavior of scattering at small size parameters to the ray-like behavior at large size parameters, thus capturing the complex interplay between the wave nature of light and the physical geometry of the scattering particles.

The size parameter, denoted as α, is a critical factor in light scattering, defined by $\alpha = 2\pi r/\lambda$, where r is the particle radius and λ is the wavelength of incident light. In the Rayleigh scattering regime ($\alpha \ll 1$, typically $r < \lambda/10$), scattering is isotropic and independent of the direction, as illustrated on the left side of Figure 2.2. Mie scattering occurs when α approaches 1, which is when the particle size is comparable to the wavelength of light ($r \approx \lambda/10$ to $r \approx \lambda$), resulting in the complex angular scattering pattern shown in the center of Figure 2.2. For larger particles ($\alpha \gg 1$, $r > \lambda$), the scattering pattern transitions to geometric optics, demonstrating directional shadowing and reflection, depicted on the right side of Figure 2.2.

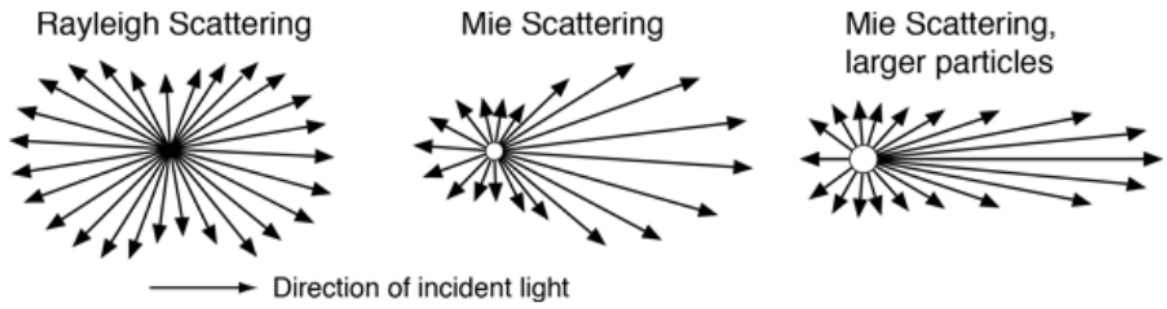

Figure 2.2: Scattering patterns for different size parameters: Rayleigh scattering for $\alpha \ll 1$, Mie scattering for $\alpha \approx 1$, and geometric optics for $\alpha \gg 1$ obtained from [17].

2.3. Light Properties for Greenhouses

2.3.1. Perpendicular Transmittance

One important aspect of a coating is the direct transmittance of light, or perpendicular transmission defined by the Nederlandse Normalisatie-Instituut (NEN) [8]. This assessment is defined for light within the PAR spectrum which includes wavelengths between 400 and 700 nm which are essential for photosynthesis. Equation 2.15 shows how the perpendicular transmittance can be found.

$$T_{\mathrm{L}} = \frac{\int_{400\ \mathrm{nm}}^{700\ \mathrm{nm}} A_\lambda \cdot T_\lambda d\lambda}{\int_{400\ \mathrm{nm}}^{700\ \mathrm{nm}} A_\lambda d\lambda} \times 100\% \tag{2.15}$$

T_{L} is the perpendicular transmittance over the PAR spectrum, T_λ is the wavelength dependent perpendicular transmittance and A_λ is the wavelength dependent plant efficiency which is the efficiency with which the plant can utilize the light of a certain wavelength.

NEN gives values of A_λ in discrete 10 nm increments over the PAR spectrum which can be seen in table 2.1. They also give a corresponding sum that approximates the integral, this can be seen below in equation 2.16.

$$T_{\mathrm{L}} = 0.000438 \sum_{\lambda \in I} A_\lambda \cdot T_\lambda \times 100\% \tag{2.16}$$

Here T_{L} is calculated for all λ in the set I = {400 nm, 410 nm, ..., 700 nm}. As this NEN method is widely used and most known to the agricultural business, this will be the method used to calculate the perpendicular transmittance throughout this thesis.

λ (nm)	A_λ	λ (nm)	A_λ	λ (nm)	A_λ
400	23.64	500	78.11	610	78.08
410	47.28	510	78.54	620	77.68
420	53.59	520	77.84	630	74.96
430	53.25	530	81.54	640	76.54
440	65.91	540	80.54	650	74.31
450	75.22	550	81.75	660	75.63
460	77.42	560	80.00	670	78.75
470	77.12	570	78.44	680	76.04
480	79.49	580	79.37	690	68.72
490	76.17	590	74.75	700	35.80

Table 2.1: The plant efficiency (A_λ) is per wavelength (λ) in 10 nm increments, with the data sourced from NEN [8].

2.3.2. Hemispherical Transmittance

Hemispherical light can be described as light coming from a hemisphere over the observer or target and which is distributed equally over the hemisphere surface [18]. The hemispherical transmittance (HLT) is then the total transmission of hemispherical light. This measure is often used as it gives more insight into the behaviour of sunlight as this comes from all directions compared to perpendicular transmittance.

The NEN provides a standard calculation method for (HLT) corresponding to certain measurements. Firstly wavelength dependent transmittance (T_λ) is measured with various angles of incidence θ = 0°, 15°, 30°, 40°, 45°, 50°, 60°and 75°. The transmittance at an angle of 90°is taken to be zero and a piecewise polynomial interpolation is applied to the angle dependent transmittance values for every orientation to create a curve for the angles of 0° to 90° with a 1° interval.

HLT is then determined according to equation 2.17.

$$HLT = \frac{\int_0^{360} \int_0^{90} T_{\phi,\theta} \sin(\theta)\cos(\theta) d\theta d\phi}{\int_0^{360} \int_0^{90} \sin(\theta)\cos(\theta) d\theta d\phi} \times 100\% \tag{2.17}$$

where $T_{\phi,\theta}$ is the angle dependent transmittance, θ the angle of incidence and ϕ is the orientation angle. These angles can be seen in a schematic overview given in figure 2.3.

$T_{\phi,\theta}$ in its turn can be determined according to equation 2.18.

$$T_{\phi,\theta} = \frac{\int_{400\ \mathrm{nm}}^{700\ \mathrm{nm}} A_\lambda \cdot T_{\lambda,\phi,\theta} d\lambda}{\int_{400\ \mathrm{nm}}^{700\ \mathrm{nm}} A_\lambda d\lambda} \times 100\% \tag{2.18}$$

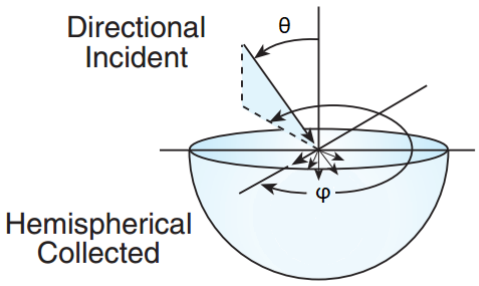

Figure 2.3: Schematic overview of the angled geometry used to calculate HLT taken and adjusted from [19].

Where $T_{\lambda,\phi,\theta}$ represents the angle-dependent transmittance for a specific wavelength λ. Again the discrete wavelength dependent plant efficiency A_λ from NEN can be used which gives the following sum approximating the bottom integral.

$$T_{\phi,\theta} = 0.000438 \int_{400\ \text{nm}}^{700\ \text{nm}} A_\lambda \cdot T_{\lambda,\phi,\theta} \times 100\% \tag{2.19}$$

As defined by NEN, $T_{\phi,\theta}$ should be found for θ = 0°, 15°, 30°, 40°, 45°, 50°, 60°and 75°. By taking the $T_{\phi,\theta}$ at θ = 90° to be zero, a piecewise polynomial interpolation is applied to get the transmittance at each integer angle θ. Finally, when a sample exhibits isotropy which is assumed for calculating HLT, there is no ϕ angle dependence. Then the HLT can be found with the following formula:

$$HLT = \frac{\sum_{\theta=0^\circ}^{90^\circ} T_\theta \cdot cos(\theta) sin(\theta)}{\sum_{\theta=0^\circ}^{90^\circ} cos(\theta) sin(\theta)} \tag{2.20}$$

Combining all formulas in discrete format with the above assumptions we get the final formula for calculating the hemispherical transmittance which can be seen below in equation 2.21.

$$HLT = 0.000876 \int_0^{90^\circ} \left[\sum_{\lambda \in I} A_\lambda \cdot T_{\lambda,\theta} \sin(\theta) \cos(\theta) \right] d\theta \times 100\% \tag{2.21}$$

2.3.3. Hortiscatter

Another characteristic defined by NEN is Hortiscatter, which is designed to give insight into the degree of light scattering of a coating. 100% would resemble 'perfect' Lambertian scattering whereas 0% would mean that no scattering has taken place.

For the calculation of Hortiscatter defined by NEN the measurement of an isotropic scattering material is independent of the azimuth angle ϕ. Therefore this angle can be arbitrarily taken and will not be part of the formulas. The angles mentioned can be seen in figure 2.4.

To measure and find the Hortiscatter value of a certain coating, NEN defines a few calculation steps that need to be done. Firstly the transmittance distribution function (TDF) of the sample needs to be found which is used together with the theoretical sample TDF and Lambertian TDF to calculate the Hortiscatter.

A TDF is the normalised intensity distribution found at each exit angle of light passing through a sample, or for the reference without a sample. In this case, the light beam is collimated and enters the sample perpendicularly. To give more insight, theoretical distributions are shown for a scattering sample, a perfect reference measurement and finally a perfect Lambertian scatterer. These can be seen in figure 2.5.

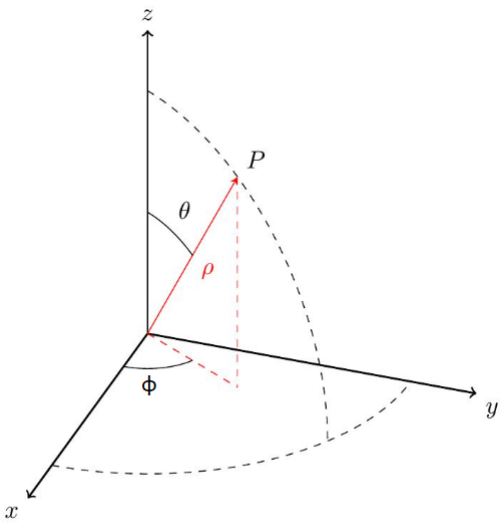

Figure 2.4: Indication of the coordinates used to measure Hortiscatter where the sample on the x-y axis is illuminated from the -z direction and P is the scattering direction of light. This image is taken and adjusted from [20].

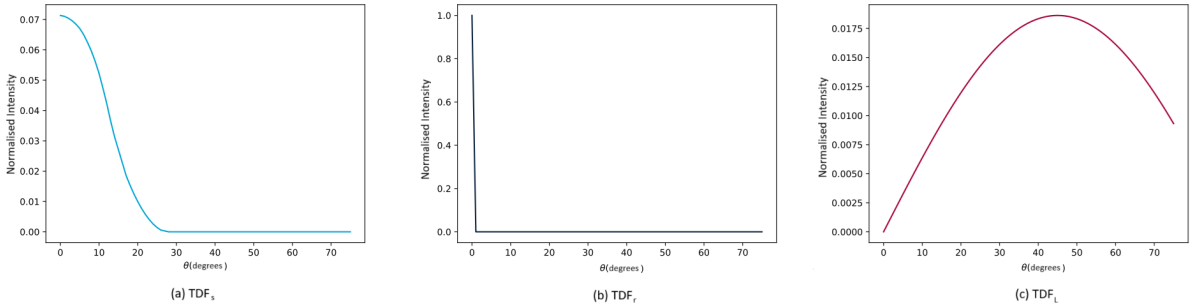

Figure 2.5: Examples of transmittance distribution functions (TDFs). (a) A theoretical sample TDF with some amount of scattering, (b) a perfect reference TDF and (c) a theoretical Lambertian TDF. Taken from [21].

To find the TDF of the sample (TDF_s), a measurement needs to be done which is depicted schematically in figure 2.6. The intensity is measured between θ = 0° and θ = 75° in 1-degree increments which will be denoted as $I_s(\theta)$ with the sample in place and $I_r(\theta)$ with no sample in place as a reference.

Then TDF_s can be found with the following equation:

$$\mathrm{TDF_s}(\theta) = \begin{cases} \sum_{\theta=0}^{\theta=75} \sin(\theta) \cdot \left(\frac{I_\mathrm{S}(\theta=0)}{I_\mathrm{R}(\theta=0)} \cdot I_\mathrm{R}(\theta) \right) & \text{for } \theta = 0, \\ \sin(\theta) \cdot \left(I_\mathrm{S}(\theta) - \frac{I_\mathrm{S}(\theta=0)}{I_\mathrm{R}(\theta=0)} \cdot I_\mathrm{R}(\theta) \right) & \text{for } \theta \neq 0. \end{cases} \tag{2.22}$$

Where $I_s(\theta)$ and $I_r(\theta)$ are the angle dependent intensities with θ corresponding to the angle shown in figure 2.4. Here the reference measurement is used to try and adjust the sample measurement such that it gets as close to the theoretical value as possible. It is important to note that the reference measurement, in reality, is also not perfect, measuring for example small intensities at θ = 1°. For the further calculation of Hortiscatter, the theoretical reference measurement is taken which for a perfectly collimated beam is only nonzero at θ = 0°. This can be seen in figure 2.5(b). Equation 2.23 below gives the mathematical formulation.

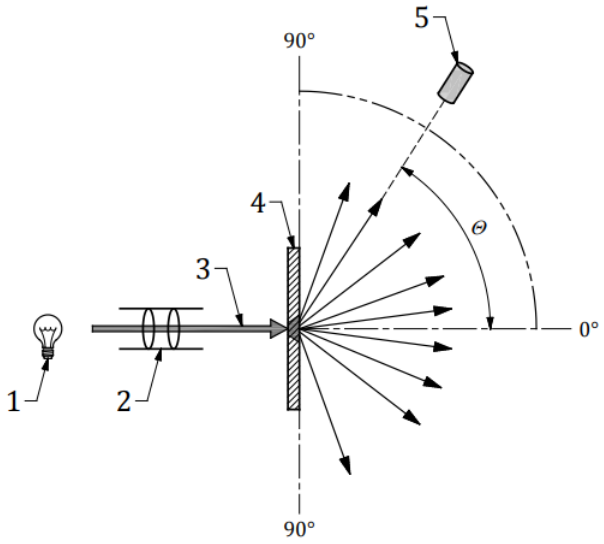

Figure 2.6: Schematic view of angle dependent intensity measurement of the sample before a light source taken from NEN [8]. θ is the scattering angle. 1 = light source, 2 = optics, 3 = light beam, 4 = sample, 5 = detector.

$$\mathrm{TDF_r}(\theta) = \begin{cases} 1 & \text{for } \theta = 0, \\ 0 & \text{for } \theta \neq 0. \end{cases} \tag{2.23}$$

The theoretical Lambertian scatterer is also used to calculate Hortiscatter which can be seen in figure 2.5(c). The mathematical formulation is given in equation 2.24 below:

$$TDF_{\mathrm{L}}(\theta) = \frac{\sin(\theta)\cos(\theta)}{\sum_{\theta=0}^{\theta=75}[\sin(\theta)\cos(\theta)]}. \tag{2.24}$$

All TDFs are normalized according to equation 2.25 to get the wavelength dependent relative scatter distributions.

$$TDF(\theta) = \frac{TDF(\theta)}{\sum_{\theta=0}^{\theta=75} TDF(\theta)}. \tag{2.25}$$

To calculate Hortiscatter the standard deviations of TDF_r and TDF_s subtracted by TDF_l are calculated given below.

$$\sigma_r = \sqrt{\frac{1}{76} \times \sum_{\theta=0}^{75} \Big((TDF_R(\theta) - TDF_L(\theta)) - \overline{TDF_R(\theta) - TDF_L(\theta)} \Big)^2}, \tag{2.26}$$

$$\sigma_s = \sqrt{\frac{1}{76} \times \sum_{\theta=0}^{75} \Big((TDF_S(\theta) - TDF_L(\theta)) - \overline{TDF_S(\theta) - TDF_L(\theta)} \Big)^2}. \tag{2.27}$$

Finally using these standard deviations the Hortiscatter value (HS) can be found.

$$HS = (1 - \frac{\sigma_s}{\sigma_r}) \cdot 100\%. \tag{2.28}$$

Note that this can be done for each wavelength. To get a final HS value, a weighted average must be taken of the wavelengths between 300 and 1100 nm using a black body radiator at 3200K as a weight function.

3

Methods

This chapter will first discuss the simulation software, which input parameters are used as well as the 3D space created to simulate HLT and HS. Next, the process for optimizing the experimental setup for measuring HS is detailed, as the preexisting setup was found to have some flaws such as alignment issues and spectrometer over-saturation disrupting the results. This is followed by an explanation of the final HS and HLT measuring setup. Finally, the optimization of the coating production process is presented, which needed to account for particles in solution instead of in dry form. Lastly, the coating production process is described.

3.1. Computational method

To assess the coating's properties, a 3D structure is defined within LightTools, an optical design and analysis software that incorporates Monte Carlo ray tracing and Mie theory [22]. As the goal of this thesis is to validate simulations and experiments, the structure was copied from a previous master's thesis that did similar simulations [9].

3.1.1. Anatomy of the Physical Structure

The structure consists of four main components: the light source, the detector cage, the glass, and the coating. Rays emitted from the light source interact with the coated glass and end up somewhere on the detector cage. Using the location of which the light rays end up in the detector cage, properties such as transmission can be simulated. A schematic representation of this structure is illustrated in Figure 3.1.

3.1.2. Light source

A circular light source composed of numerous point sources, mimicking for example the sun, is placed 5mm above the glass surface, with a diameter of D = 200mm. The exact spectral emittance can be adjusted, as well as the angle of the emitted light relative to the glass normal depending on which effects want to be simulated.

The light source can be set to have an aim sphere determining at which angles light is emitted from the various point sources. This can be seen in a schematic shown in Figure 3.2. When an aim sphere of lower angle 0 °and higher angle 1 °is set, an equal amount of photons will be emitted between these angles. The total amount of photons can be chosen for each simulation. Typical numbers are between $1{\cdot}10^5$ and $1{\cdot}10^7$ photons.

While in this case, the sun is circular, it is important to note that any form would give near identical results as long as all the rays that exit the source interact with the coated glass. This is because LightTools exclusively employs statistical methods and does not account for spatial dependence.

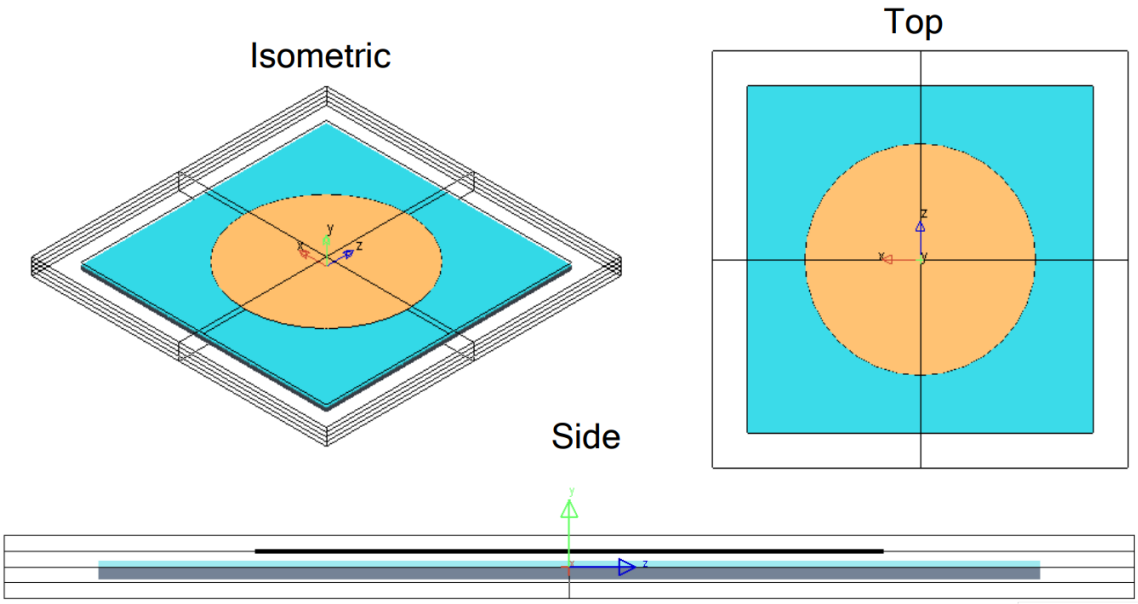

Figure 3.1: This schematic taken from [9] illustrates the structure with different views. The components that have been given colors for illustration purposes are the light source (light brown circle), coating (turquoise square), and glass (dark blue square). The transparent box with certain contour lines indicates the detector cage.

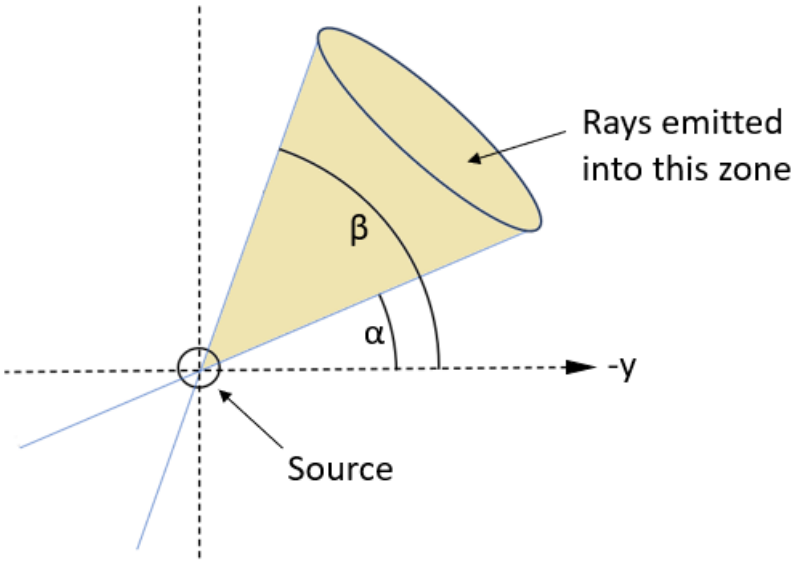

Figure 3.2: This is a schematic made based on the LightTools manual [22] showing how a light source with a certain aim sphere emits. Here α is the lower angle and β is the upper angle.

3.1.3. Glass

The glass, which can be identified as the dark blue rectangle on the side view of Figure 3.1 is set to have the same dimensions as the experimental glass used measuring 300 x 300 x 4 mm. The surface of the glass is set to have the 'smooth optical' property which implies zero surface roughness. All light interactions are thus defined by the Fresnel equations making the only parameter of interest the complex refractive index. The glass used is a low iron glass Pilkington Optiwhite^{TM} made by NSG group [23]. The used wavelength dependent n and k for this type of glass were taken from

Refractiveindex.INFO [24] which got their data from variable-angle ellipsometer measurements done by R. E. Treharne [25].

3.1.4. Coating

The coating is placed on top of the glass shown in light blue in Figure 3.1. While the thickness in the y direction is variable, the other dimensions match those of the glass (300 x 300 mm). The coating surface is also set to have the 'smooth optical' property and consists of a polymer with a density of 1.06 mg/mm3 and a refractive index of n = 1.4052 as determined by Fotoniq. Homogeneously dispersed spherical particles can be added to the coating with their own complex refractive index, radius and coating weight- or volume percentage. The particles used, together with their respective variables, will be discussed in the choice of particles and coating production seen in section 3.4.

3.1.5. Detector cage

As shown in Figure 3.1, the entire structure is contained in a detector cage. This cage can detect the location and angle of photons that are either reflected or transmitted through the coated glass. This information is used to determine how light interacts and can be used to calculate the simulated HLT and HS. For these simulations, only the bottom detector surface is used which detects the transmitted photons.

3.1.6. Simulating hemispherical light transmission

When simulating HLT, the light source is set to emit the solar spectrum AM1.5g taken from [26]. This was arbitrarily chosen as NEN only defined the need for a non-polarized light source with spectral emittance between 400 and 700 nm.

The angle dependent transmittance per wavelength is found by setting the aimsphere to have the same upper and lower bound angle, thus only emitting at a single angle, corresponding to the same angles defined by NEN given in chapter 2.

Finally the angle dependent transmittance $T_{\lambda,\theta}$ is found by collecting the intensity on the bottom of the detector cage resembling the intensity that passed through the sample. From this, the HLT can be calculated according to chapter 2.

3.1.7. Simulating hortiscatter

To simulate Hortiscatter, the light source is set to be a black body radiator of 3200K according to NEN [8]. In this case, the emitted photons are chosen according to the weight function defined by the black body distribution. A single HS value for each wavelength can also be calculated. In this case, the light source is set to emit a single wavelength.

Using the angle of the photons that reach the bottom detector cage, corresponding to their angle of exit from the sample, the angle dependent intensity can be found. This is stored in bins with integer degree values as bin centers. For the bins, a slice is taken in the solid angle space as shown in Figure 3.3, taken from the user manual. Each bin along the slice is the same size in solid angle space. In this case, due to the isotropic symmetry of the system, only one slice needs to be taken into account. It is important to note that for the reference beam consisting of an aim sphere with a lower angle of 0° and a higher angle of 1°, the counts of the angle 0 bin will be twice as large as those of the angle 1 bin. This is because the zero angle bin can collect photons from -0.5° to 0.5° where photons can be found in the full range, whereas the angle 1 bin can collect photons from 0.5° to 1.5° of which photons can only be found in the first half.

The main difference between simulation and measurement is that in LightTools it is possible to use wavelength dependence when collecting the angle dependent intensities to calculate HS. This approach can be done due to the light source being a black body radiator of 3200K.

As this cannot be achieved in reality, a different light source is used for physical measurements. Using this, the HS is individually calculated for each wavelength. To find a single value, the wavelength dependent HS spectrum is averaged using the black body radiator as a weight function. However, to be able to compare the wavelength dependent angular distribution, the light source of the simulation can also be set to a singular wavelength before calculating the HS value corresponding to that wavelength.

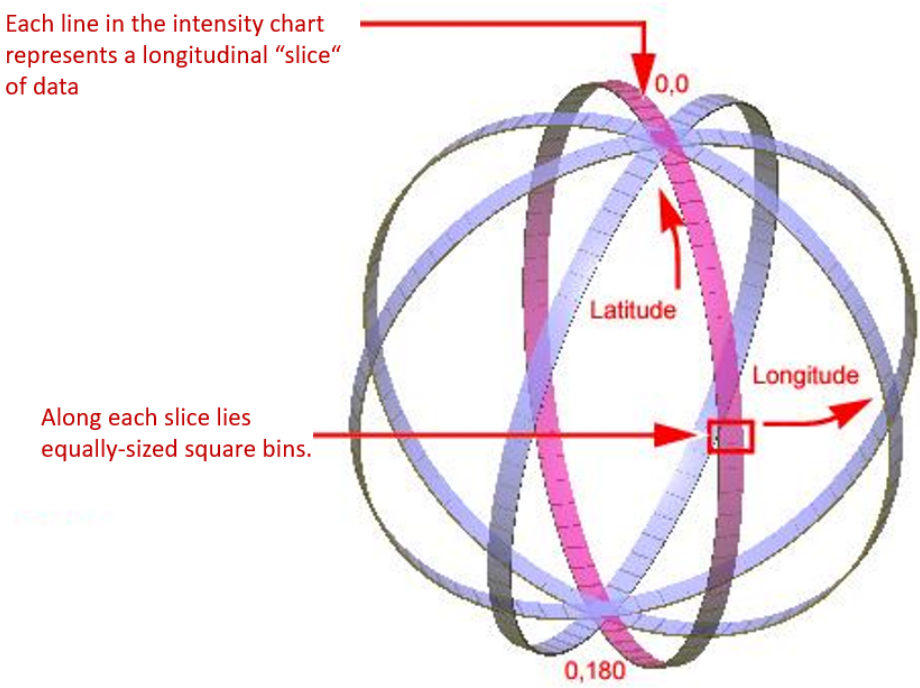

Figure 3.3: How the Intensity Slice Data Collection Method Works, taken and adapted from the LightTools software built-in user guide.

This process can be iterated over the same wavelengths as measured in the physical setup. While using this method it is possible to compare the wavelength dependent HS values, these simulation times are much longer.

3.2. Experimental method

This section details the experimental methods used to measure hemispherical transmission (HT) and Hortiscatter (HS) of coated glass samples. The first part describes the optimization process for the Hortiscatter setup, addressing issues identified in a previous design. This includes improvements in light collimation, alignment, and detector positioning to improve angular scattering measurements. The final optimized HS setup is then presented. Following this, the section outlines the experimental setup for measuring hemispherical transmission using an adapted double-beam method.

Next, the selection of particles for the coatings is discussed, highlighting the importance of particle properties such as size and sphericity. The rationale behind choosing specific particle types and sizes is explained, and supported by simulation data.

Finally, the coating production process is described. This includes optimisation and adaptation of existing formulation to prepare various coating thicknesses and compositions which are used for subsequent measurements

3.2.1. Optimizaion of Hortiscatter setup

To measure HS, a setup was built by a previous master’s student E.P. Vernhout [21]. As described in his thesis, this design still has some flaws. Combined with some discrepancies discovered during the process, a new design was built to improve the overall functionality. The process of optimizing the setup will be described.

The preexisting setup

As defined by NEN, and explained in the Theory, the basis of a HS setup needs a collimated beam with a light spectrum between 300-1100 nm. This collimated beam is to then pass through a sample, where the exit plane of the sample is the rotation point for a detector. The detector should be able to move

across a 2D semi-circle indicated with angle θ to be able to capture the intensity of scattered light at each angle. (see Figure 2.6). To incorporate these basic design characteristics, a design was created by E.P. Vernhout which can be seen in Figure 3.4

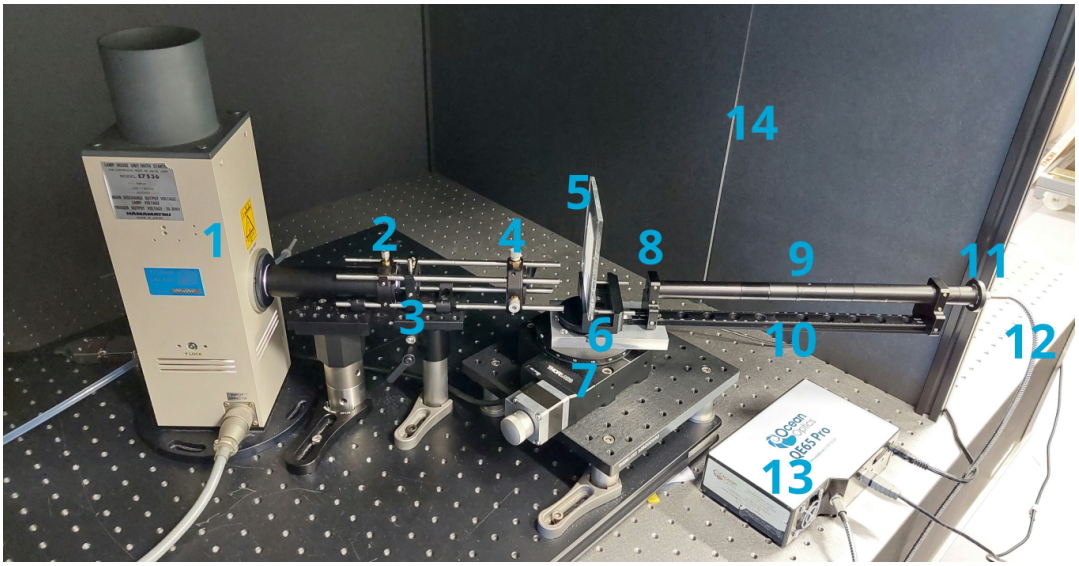

Figure 3.4: Preexisting setup directly taken from [21]. 1. Lamp (house), 2. Left lens, 3. Left pinhole, 4. Right lens, 5. Coated glass sample, 6. Sample holder, 7. Rotating stage, 8. Right pinhole, 9. Tube, 10. Rotating arm, 11. Fiber/Detector opening, 12. Fiber, 13. Spectrometer, 14. Ambient light blocking box.

The lenses (2)(4) collimate the light from the lamp (1). A pinhole (3) is placed between the lenses to remove unwanted light and mimic a point source. The collimated beam enters the sample (5) where the rotating stage (7) can move the following elements to a desired angle θ with respect to the stationary sample. These rotated elements are another pinhole (8) and tube (9) designed to increase the resolution by decreasing the acceptance area of entering light. finally, the detector opening (11) is connected to the spectrometer (13) by an optical fiber (12).

In the next few parts, certain parts of the setup will be explained together with underlying issues.

Collimation

The light source is a Hamamatsu L2273 Xenon lamp and it is placed in a Hamamatsu lamp house unit of model E7536. As the ignition takes place via an anode and cathode, the light source can be approximated as a point source. However, due to the housing reflecting light, as well as the light emitted from the anode and cathode material, the presence of a point source is disrupted. To overcome this issue a first lens was placed to focus the light onto a pinhole, again mimicking a point source for the light exiting the pinhole. By placing another lens with the focal point at the pinhole, the light can be focused into a collimated beam.

The main issue with the creation of this collimated beam is the diffraction patterns observed in the beam, disrupting the uniformity. The reason for the importance of a uniform beam will become clear when looking at the detector acceptance area.

Detector acceptance area for the sample

The detector acceptance area for the sample, or in other words the area of the sample that is seen by the detector, can be visualised by reversing the path of light from the end of the spectrometer onto the sample with a laser. This is done by shining a laser back through the optical fiber onto the area of the sample that would be visible by the detector. From this, the acceptance area of the spectrometer can be observed. For measuring scattering effects, it is important that the acceptance area of the spectrometer is located on a part of the coating that is inside the collimated beam. While discussed in more detail later, this can be seen in Figure 3.6. The location of the acceptance area can vary when changing the angle. There are three main effects that are important in this case, namely:

1. Viewing angle effect
2. Misalignment effect
3. Glass refraction effect

The viewing angle effect arises when looking at the sample from an angle. While starting off as a circular acceptance area $dA_{\perp}$ when perpendicularly looking at the glass at $\theta = 0°$, increasing θ will increase the surface area of the circle in one direction, causing the formation of an ellipsoidal shape dA_0. This is shown in a schematic in Figure 3.5a. Thus for higher angles, the acceptance area increases.

The misalignment effect takes place when the angle of rotation is not exactly at the surface of the sample where the collimated beam exits. In that situation, the acceptance area will shift location when increasing the viewing angle. This is purely due to misalignments where minimal variations can have significant results. This is schematically demonstrated in Figure 3.5b

Finally glass refraction effect is the difference in the acceptance area on either side of the glass due to light being bent by the difference in refractive index of the glass with respect to the air. This shows the importance of looking at the acceptance area after passing through the glass to determine whether the acceptance area of the coating is inside the collimated beam.

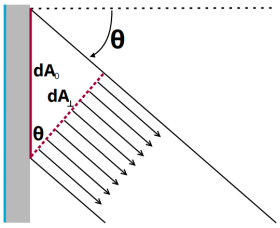

(a) Schematic showing the viewing angle effect taken from [21]. The increased acceptance area of the detector dA_0 is shown with respect to the perpendicular case $dA_{\perp}$ when increasing the angle θ

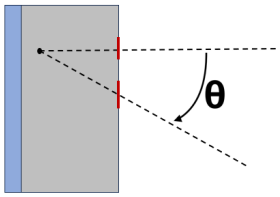

(b) Schematic showing the misalignment effect due to the rotation point not being on the most right surface of the glass. Due to this misalignment, the acceptance area is shifted in position at large angles θ.

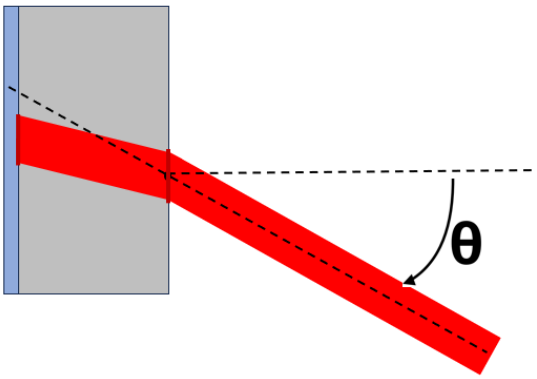

(c) A schematic of the glass refraction effect, where the acceptance area on either side of the glass is shifted.

Figure 3.5: Schematics showing three effects that take place that determine the exact detector acceptance area of the sample. In all three schematics, the glass is depicted as a gray rectangle, the coating as a blue rectangle to the left of the glass. The detector is to the right and The rotation point is indicated by the black dot at the intersection of the two lines that form the angle θ: a solid line and a dashed line in (a), and two dashed lines in (b) and (c).

Both the formation of an ellipse shape as well as the shifting in location are documented in Figure 3.6. Here a piece of paper is placed at the location of the sample to be able to see light from the beam as well as the laser projected on the paper from two different sides.

Both the viewing angle effect and the misalignment effect have been visualised in Figure 3.6. Here a glass sample was placed in the sample holder with a piece of paper on the surface where a coating

would otherwise be located. By illuminating the sample with the Xenon light source, as well as the laser coming from the opposite direction, it can be verified if the acceptance area of the spectrometer is inside the collimated beam at the detector side of the glass. As the effect is expected to be largest at θ = 75, it was chosen to only look at θ = 0°and 75°. In this case, the glass refraction effect is not taken into account and ideally, the picture must be taken from the other side to see if the detector acceptance area of the coating side of the sample is inside the collimated beam projection.

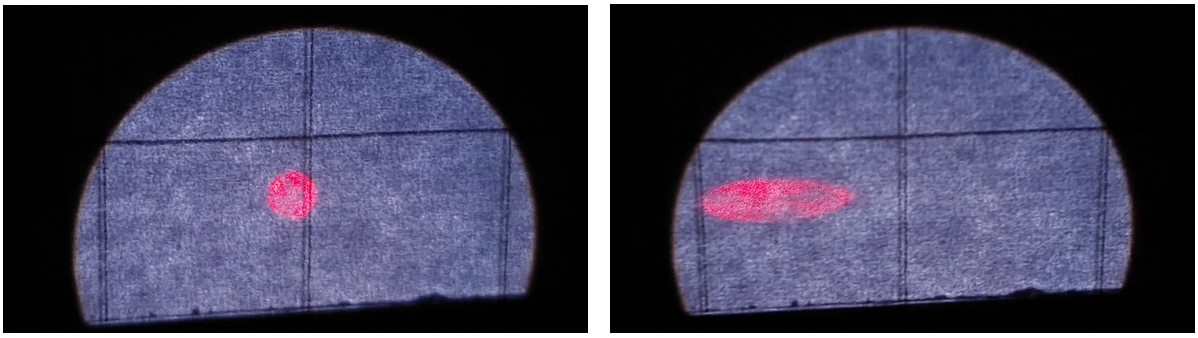

(a) θ = 0° **(b)** θ = 75°

Figure 3.6: Pictures of the acceptance area of the detector on the side of the glass facing the detector visualised with the use of a red laser taken from [21]. To show the light coming from 2 directions, a piece of paper is placed on the surface of the glass. The blue/white partial sphere is the collimated beam projecting onto the paper. The red part is the projection of the laser onto the paper. This has been done for θ = 0°(a) and θ = 75°(b)

The change in the acceptance area of the sample from the perspective of the spectrometer indicates the importance of having a collimated beam that is homogeneous, as otherwise, the spectral intensities will change while varying the angle θ, altering the values of TDF_s used to calculate the wavelength dependent Hortiscatter.

The shifting of the spectrometer acceptance area also shows the importance of good alignment, where the rotation point needs to be on the surface of the glass. If the acceptance area shifts too much at higher angles due to bad alignment, it can end up viewing a portion of the sample that is not in the path of the collimated beam. This will decrease the counts measured at higher angles, giving lower values of HS. The shift due to the glass refraction effect must also be taken into account.

When aligning the setup and choosing the beam size, it is important to check if the acceptance area of the coating side of the glass remains inside the beam area. It is also desired that the acceptance area shifts as little as possible. This can be checked by visualising the acceptance area with a laser at θ = 0°and θ = 75°as shown in Figure 3.6.

Detector view area of the reference

When doing a reference measurement, where no sample is placed in the sample holder, it is important to check if the highest intensity is measured for θ = 0°. This gives an indication on if the setup is aligned correctly as the highest intensity is expected when the detector tube is parallel to the collimated beam. Apart from this, it is also important that the view area of the spectrometer, for angles higher than θ = 0°, does not look into any of the lenses used to collimate the beam. As the lenses are not perfect and emit light in unwanted directions, light will be measured when viewing part of the glass. This will give a reference measurement with high counts at θ > 0°, disrupting the measurement due to counts not coming from the collimated beam. Unfortunately, this was the case for the setup described. A schematic can be seen in Figure 3.7.

Over-saturation

When measuring the angle dependent intensities, it is important that the spectrometer does not over-saturate. Due to the high intensity of the Xenon light source, this was a problem at θ = 0°, where the highest intensity is present. When using the shortest integration time, the spectrometer is still over-saturated at 825 nm where the Xenon lamp spectrum has the largest intensity. To overcome this, E.P. Vernhout wrote a code that corrected for saturation by fitting the known spectrum into the measured

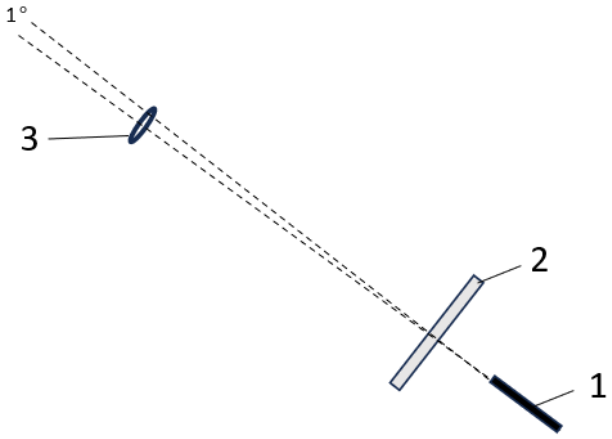

Figure 3.7: Schematic of reference measurement acceptance area at θ = 0°and 1°. 1. Detector tube, 2. Sample and 3. Lens. Preferably the 1°viewpoint does see the lens.

spectrum. This is however undesirable as artificial data points are created which differ from the true spectrum.

Problem statement

The above-mentioned issues of the setup that need to be resolved are:

1. Beam collimation which showed diffraction patterns
2. Sample acceptance area shift due to misalignment
3. Reference detector view area on the lens at θ > 0°
4. Over saturation spectrometer at θ = 0°

To overcome the diffraction due to the pinhole, a new mechanism for creating a collimated beam was designed. Instead of using two lenses and a pinhole, which caused diffraction issues, it was chosen to use a parabolic mirror to create a collimated beam from the Xenon lamp. Due to the light-emitting surface between the anode and cathode being about 0.3 x 0.5 mm, it can be approximated as a point source [27]. When a point source is placed in the focal point of an Off-Axis Parabolic (OAP) mirror, a collimated light beam is created. This is shown in a schematic depicted in Figure 3.8.

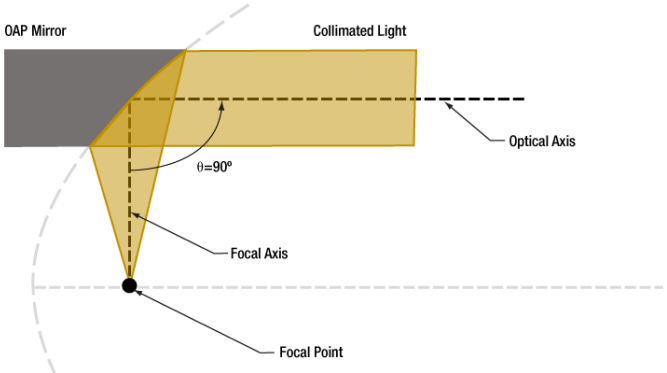

Figure 3.8: Schematic parabolic mirror taken from [28].

Due to reflection by the lamp housing, as well as light emitted by the anode and cathode disrupting the point source assumption, a diaphragm is placed at a large enough distance from the beam source so that light not originating from the point source, has diverged out of the otherwise collimated beam. To

increase the distance travelled, a mirror was placed to make use of the space available for the setup. This can be seen in the schematic of the final setup shown as number 3 in Figure 3.9.

It was found in the old setup that the rotation point was on the wrong side of the glass. As shown in Figure 3.5b, this causes the acceptance area of the sample to move. Therefore the rotation point needed to be adjusted to be on the most right surface of the glass closest to the detector. To achieve this, the estimated offset was milled out of the sample holder, enabling the sample to move 4 mm further away from the detector. While not perfectly positioned, the acceptance area moved less far at higher angles in comparison to before.

Also the viewpoint of the reference measurement at $\theta > 0°$needed to not look into any type of mirror, glass, or light emitting materials. To achieve this, it was chosen to place the above-mentioned diaphragm as far as possible from the detector opening. While in combat with the diaphragm needing to be far from the source to remove unwanted light, it was chosen to make use of the full diagonal space available as the distance between the detector and the diaphragm. This was done with a mirror, seen as number 3 in Figure 3.9, to redirect the collimated beam, making full use of the table.

While decreasing the diaphragm size would also help with the $\theta = 1°$reference viewpoint from going through the diaphragm, this in its turn decreases the beam size on the sample. If decreased too much, the sample viewpoint may partially move out of the area of the sample in the beam at high angles due to the effects depicted in Figure 3.5. Thus a balance needs to be found between decreasing the beam size, which keeps the acceptance area out of unwanted elements, and increasing the beam size which keeps the acceptance area of the sample inside the collimated beam.

Finally, to solve the over-saturation problem, a neutral density filter was placed in the path of the collimated beam before the diaphragm. The neutral density filter blocks a fairly constant 90% of the light in the visible spectrum coming from the Xenon lamp. While solving the over-saturation issue, the downside is that light below 350 nm is largely blocked. While NEN defined HS to be calculated between 300 and 1100 nm, the over-saturation issue was found to give more negative consequences, and its prevention was prioritised.

With the above-mentioned adjustments, a new setup was created to measure HS which will be discussed in the next section.

3.2.2. Hortiscatter setup

To measure the angle-dependent intensities needed to calculate Hortiscatter, a new setup was built based on a previous setup created by E.P. Vernhout [21]. This was done by making the adjustments mentioned above, while still adhering to the design specifications indicated by NEN.

To obtain a collimated beam, a parabolic mirror was used with a Xenon lamp placed at its focal point. A mirror was placed to redirect the collimated beam, increasing the distance travelled to allow non-collimated light to diverge from the beam. To prevent over-saturation of the spectrometer, a neutral-density filter, blocking 90% of visible light, was placed in the path of the collimated beam. Next, a diaphragm was used to decrease the size of the beam, which then passed through the sample with the coating facing the light source. The optical fiber was attached to the end of a detector tube, which could automatically rotate around the rotation point (where the scattered beam exits the sample). Finally, the optical fiber was connected to an Ocean Insight QEPro spectrometer to measure the wavelength-dependent intensity at each angle. A schematic of the setup is shown in Figure 3.9. The collimated beam, after passing through the neutral density filter, entered an enclosed box through the diaphragm to reduce light interference from the Xenon lamp.

As described in the Hortiscatter theory, the spectrometer measures the angle-dependent intensities for different wavelengths needed to calculate HS. For the reference measurement, the only difference was that no sample was placed. Each measurement was followed by a noise measurement, where the light beam was blocked at the diaphragm. This noise measurement was subtracted from the original measurement to minimize the effects of stray light reaching the detector that did not originate from the collimated beam.

To check the alignment of the setup, a laser beam was used to visualise the detector acceptance area from both the detector and the coating side of the glass. This is very similar to Figure 3.5, where a

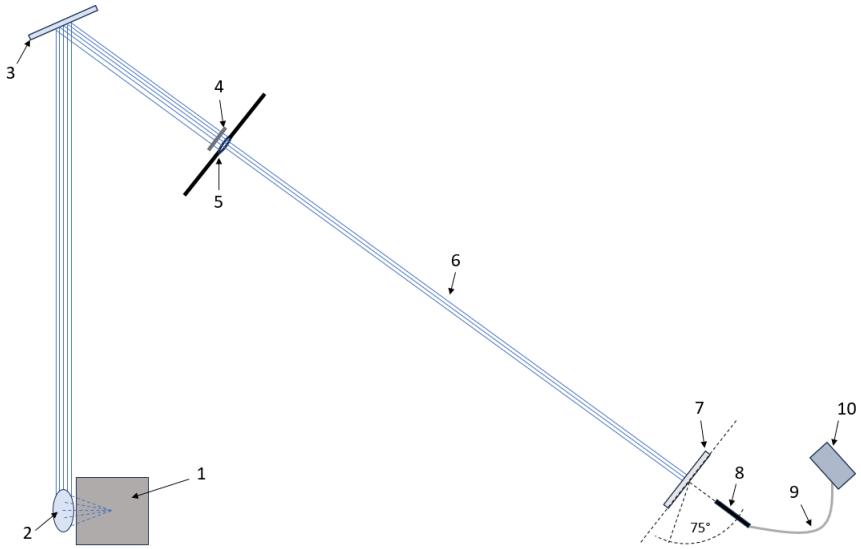

Figure 3.9: Schematic drawing of the setup used to measure Hortiscatter. 1 = Xenon light source, 2 = Parabolic mirror, 3 = Mirror, 4 = Neutral-density filter, 5 = Diaphragm, 6 = Collimated beam, 7 = Sample, 8 = Tube, 9 = Optical fiber, 10 = Spectrometer.

piece of paper was placed on the otherwise coated surface of the glass and a laser was pointed back through the optical fiber. From the opposite direction, the collimated beam illuminates a semi-sphere on the glass. It can be confirmed that the setup meets these requirements by checking if the laser is inside the collimated beam from both viewpoints at both angles θ = 0° and 75°. A schematic showing the direction of the viewpoint from the detector side and the coating side can be seen in Figure 3.10.

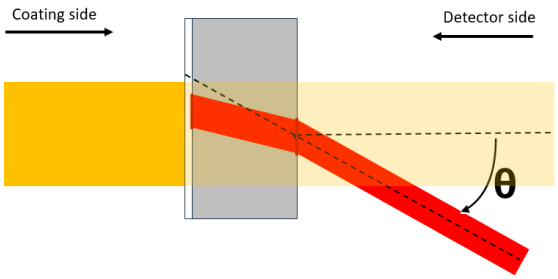

Figure 3.10: A schematic showing a correctly aligned setup where laser pointed back through the optical fiber, depicted in red, reaches the coated side of the glass within the area lit up by the collimated beam depicted in yellow. This must be true for θ = 0° and 75°. From which direction the coating and detector side are viewed are shown with black arrows.

Pictures of the detector acceptance area corresponding to the final alignment can be seen in Figure 3.11. Here it can be seen for the θ = 75°, scatter and reflection effects take place giving a lower intensity second and even higher order red acceptance area laser beam spots. It can be seen that for all images, the acceptance area lies within the illuminated part of the sample.

When looking at the view area of the spectrometer during the reference measurement, it was found that at θ = 1°, half of the view area still passed through the diaphragm onto the glass. While not perfect, fixing this problem would include changing the setup location to accompany the needed extra space. For this reason, it was chosen to accept and keep the described setup.

Finally, in the alignment process, it is crucial to check if the highest intensity is measured for θ = 0°.

When choosing the spectrometer integration time for each angle, it is important to find an integration time with enough counts but without the risk of over-saturation. This has to be checked for each angle.

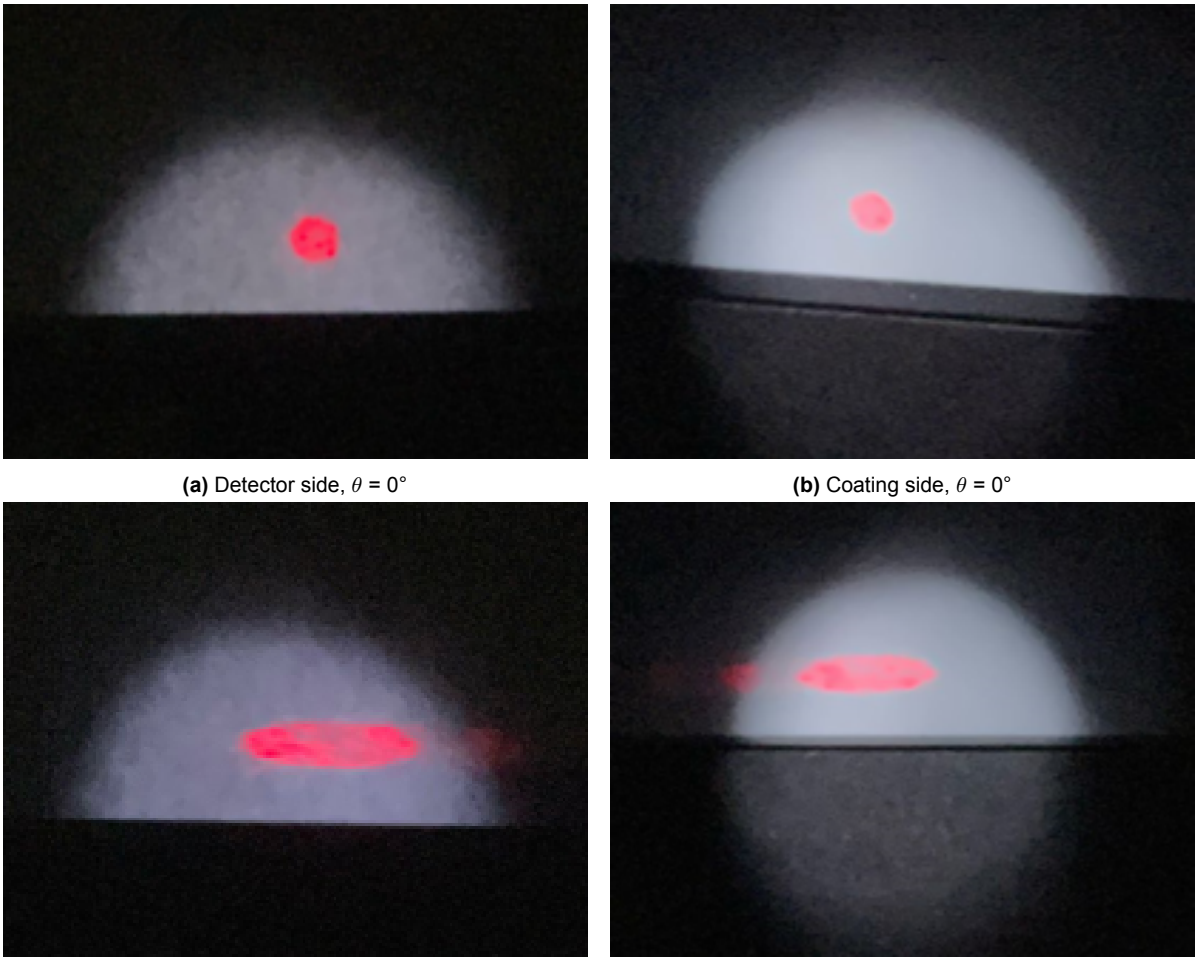

(a) Detector side, θ = 0°

(b) Coating side, θ = 0°

(c) Detector side, θ = 75°

(d) Coating side, θ = 75°

Figure 3.11: The acceptance area of the sample at both the coating side as well as the sample side for θ = 0°and 75 °. The collimated beam was reduced in intensity with an additional low-density filter relative to the actual setup to help visualise the position of the red laser beam.

It is important to note that this optimum might change for coatings that scatter light differently as the angle dependent intensities will change.

The Python code used to analyse the spectrometer data and calculate HS, which was self-written, can be found in Appendix C.1

3.2.3. Hemispherical Light Transmission setup

To measure the hemispherical transmission, a double-beam experiment was conducted according to the measurement protocol defined by NEN [8]. However, a slight adaptation was made. According to NEN, the angle-dependent transmittance for a specific wavelength, $T_{\lambda,\phi,\theta}$, can be calculated using Equation 3.1.

$$T_{\lambda,\phi,\theta} = \frac{I_1}{I_2} \cdot \frac{I_3}{I_4} \tag{3.1}$$

Here, I_1 is the light intensity measured with the sample port illuminated and the sample in place. I_2 is the light intensity measured with the sample port illuminated but no sample in place. I_3 is the light intensity measured with the reference port illuminated and no sample in place, and I_4 is the light intensity measured with the reference port illuminated and the sample in place. In all measurements, the sample was placed with the coating facing the outside of the integrating sphere. A schematic can be seen in

Figure 3.12.

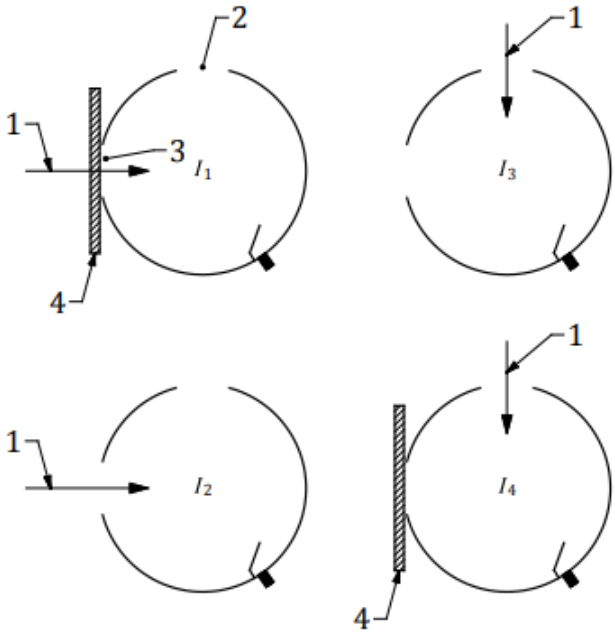

Figure 3.12: A schematic overview of the determination of I_1, I_2, I_3, and I_4, taken from NEN [8]. 1 is the light beam, 2 is the reference port, 3 is the sample port, and 4 is the sample.

However in this case, due to the difficulty of making a system that is able to consistently move the light source from the sample port to the reference port, as well as the difficulty of making an integrating sphere that can rotate over 2 axis, an adjustment was made. Instead of moving the light from the sample port to the reference port, the sample is moved from the sample port to the reference port. This is shown in an adjusted schematic in Figure 3.13. This new measurement where the sample is placed over the reference port will be called I_5. As the beam is not moved, there are no two reference measurements possible. In this case equation 3.1 is simplified to equation 3.2.

$$T_{\lambda,\phi,\theta} = \frac{I_1}{I_5} \tag{3.2}$$

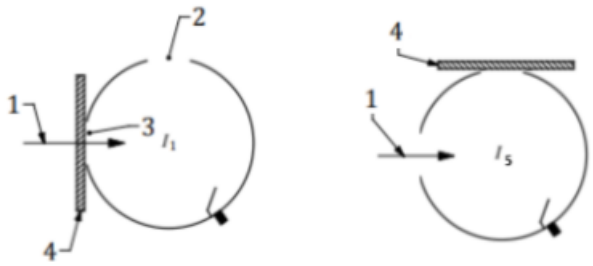

Figure 3.13: A schematic overview of the adjusted measurement of NEN, where I_1 is taken from NEN and I_5 replaces I_2 - I_4. 1 is the light beam, 2 is the reference port, 3 is the sample port, and 4 is the sample.

The integrating sphere used had a sample port, a reference port, and a port for the optical fiber. The inside of the sphere was coated with a diffuse reflective coating. The rest of the equipment used included an Avantes FC-UVIR600-0.5-BX 1909042 optical fiber, a deuterium-halogen lamp, and a QE65Pro

Ocean Optics Inc. scientific-grade spectrometer to analyze the data. Everything was placed on a rotating stage with the center of rotation at the sample port of the integrating sphere. A schematic showing the rotation can be seen in Figure 3.14.

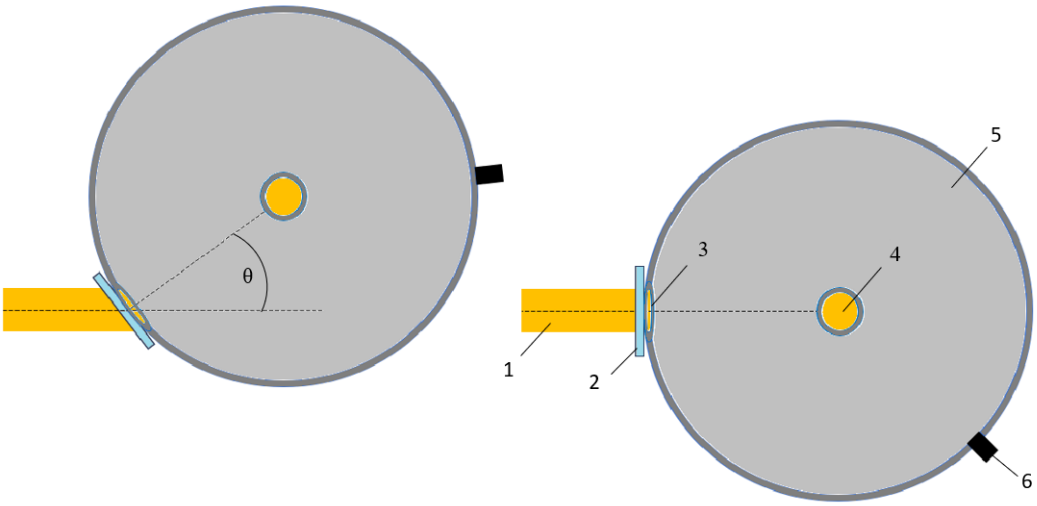

Figure 3.14: A schematic top view of how the integrating sphere is rotated with respect to the light beam, where θ is the rotation angle. 1. Collimated beam, 2. Sample, 3. Sample port, 4. Reference port, 5. Integrating sphere, 6. Detector.

It is important that the sample is perpendicular to the light beam at θ = 0° and that the whole sample port is illuminated. Additionally, at high angles, no light must enter the side of the glass, as this would result in inaccurate results. To resolve this, a piece of black tape was placed on the side of the glass where the beam might shine at large angles.

Finally, Equation 3.1 can be combined with Equation 2.21 from the theory to calculate the hemispherical transmission using the wavelength-dependent intensities measured by the spectrometer. Here, $T_{\lambda,\phi,\theta}$ is equal to $T_{\lambda,\theta}$, as isotropy is assumed as mentioned in the theory.

The Python code used to analyse the spectrometer data and calculate HLT, which was self-written, can be found in Appendix C.2

3.3. Choice of particles

For the purpose of comparing simulations to experiments of particle-based coatings, the choice of particles is of great importance. The most important aspect is the sphericallity, as LightTools implements Mie-Theory which is based on spherical particles. Silica-based spherical particles are known for their chemical stability and are also commercially available as spherical nano/microspheres [29] [30]. Also due to the fact that Fotoniq has used silica as scatter particles in the past led to the choice to use spherical silica particles.

The next choice was the particle sizes. For this LightTools simulations were done where an arbitrary but realistic particle volume percentage and coating thickness were chosen as a constant and the particle radius was varied. From this, the expected HS and HLT values were found as a function of particle radius d. This can be seen in Figure 3.15.

Based on the availability of certain particle diameters, 3 particle sizes were chosen to encapsulate the most variance in HT and HS. Firstly a particle with diameter d = 160 nm was chosen to have a low HS value, then a particle with d = 400 nm was chosen to have an average HS and low HLT, and finally, a particle with d = 5 µm was chosen to have the highest HS. While the exact simulation parameters were premature, it was found that the general behaviour of HLT and HS seemed fairly constant and these particle sizes were expected to give the most variation in results. By testing the simulation under

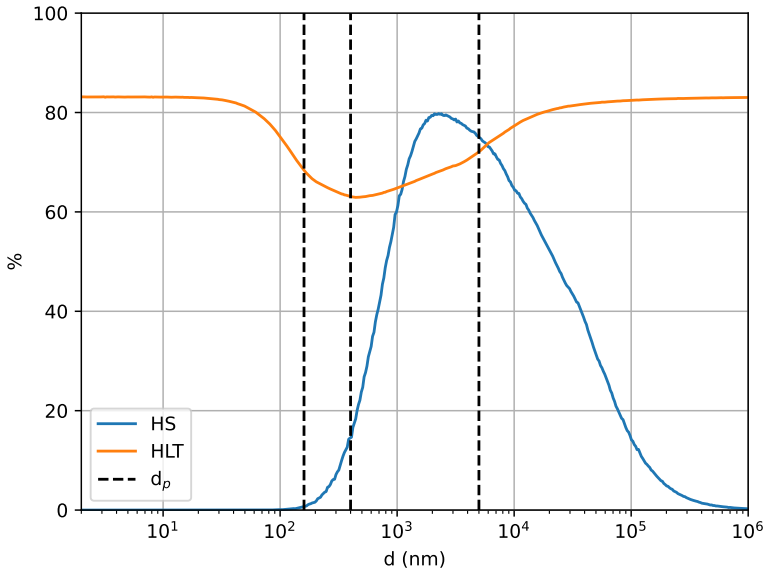

Figure 3.15: LightTools simulation of HS and HLT over particle diameter d_p. Here the dry coating thickness t_{dry} was set to a constant of 200 µm and the silica particle loading was set to a volume percentage (vol%) of 30.

diverse conditions, you can identify its strengths and limitations more effectively. This ensures that the model is not only accurate under a narrow set of conditions but also robust across a broader spectrum of scenarios.

Monodisperse silica nano/microspheres with these diameters were sourced from Alpha Nanotech due to their confirmed sphericality and monodispercity. These particles exhibit a confirmed 2.0 g/cm^3 density and are suspended in a 50 mg/ml DI water solution. Having nanoparticles in solution enhances dispersion, prevents aggregation, and has safety benefits compared to dry formats [31] [32]. The particles used are Hydroxyl-terminated, use no surfactants, and have a coefficient of variation (CV) of less than 3% indicating high monodispercity. While a low CV value is not needed for accurate simulations, it can help enhance the effects of different particle sizes. TEM and SEM images confirming their sphericality can be seen in Figure 3.16. For the simulations, the particle size was entered as a distribution around the mentioned diameter with a CV of 3%.

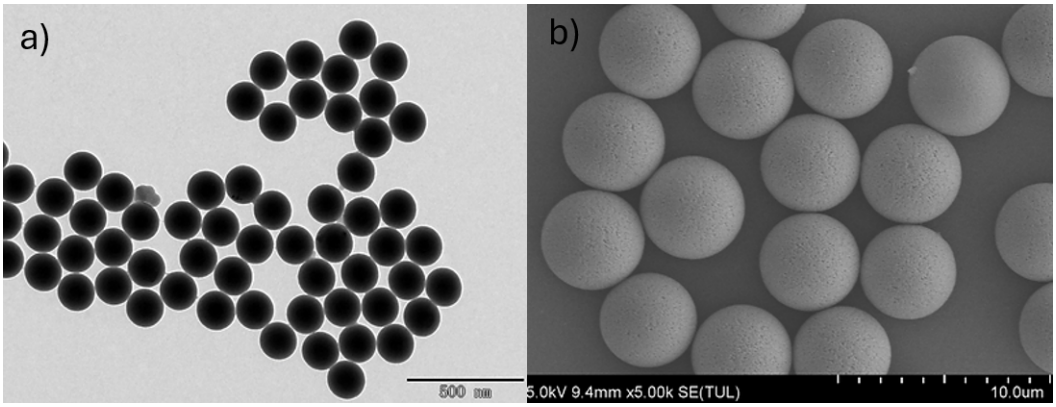

Figure 3.16: Micrographs taken from Alpha Nanotech [33]. a) is a Transmission Electron Micrograph of d = 160 nm silica nanospheres. b) is a Scanning Electron Micrograph of d = 5 µm silica microspheres.

While most parameters are well-defined for these particles, the refractive index is less known. This is mainly due to the density given by the manufacturer. The particles from Alpha Nanotech are produced

using the Stöber method, which is known to form amorphous silica [34] [35]. While bulk amorphous silica is known to have a density of around 2.2 g/cm^3 [36], the particles mentioned have a density of 2.0 g/cm^3.

This gives an indication that there is certain porosity present, which is known to have an influence on the refractive index. Assuming the porosity is homogeneous throughout, a new refractive index can be determined using the Lorentz-Lorentz relations given in chapter 2. For this thesis, it will be assumed that the pores retain water, even after drying. This is not uncommon and is mentioned in the book: "The Physics and Chemistry of Sol-Gel Processing" [37], where it is discussed that mesoporous structures (2-50 nm pores) in particular tend to retain water due to these capillary effects, as well as the fact slow drying at ambient conditions often leaves water trapped in the pores of silica.

While it is known that the particles have a different surface structure, the OH termination forms only a very thin layer on the surface of the silica particles. Given the nanometer scale of this layer compared to the overall particle size, its contribution to the overall refractive index is relatively small. According to Zhao et al [38], the surface modification of silica nanoparticles with various functional groups, including hydroxyl, results in negligible changes in bulk properties such as refractive index due to the thinness of the surface layer.

For this reason, the refractive index of the silica particles will be approximated using the Lorentz-Lorentz relations where it is assumed that water is trapped in the pores. The refractive index of fused silica is taken from Malison [39] and of water from Daimon [40]. These, including the newly calculated refractive index, can be seen in Figure 3.17.

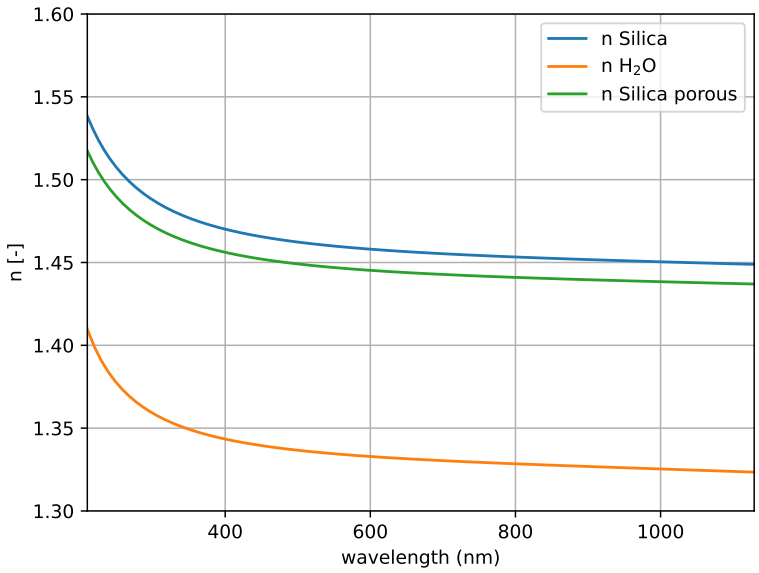

Figure 3.17: The refractive index of fused silica taken from [39], of H_2O at 20°C taken from [40] and the refractive index of porous silica containing water calculated using the Lorentz-Lorentz relations

To solve the non-linear nature of the Lorentz-Lorentz equations, the Python scipy.optimize.fsolve function is implemented returning the roots of the (non-linear) equations given a starting estimate. To match the exact wavelengths of the refractive indexes, linear interpolation is applied to one of the two wavelength dependent refractive indexes.

3.4. Coating production

Coating optimization

Fotoniq has experience and well-developed formulations for creating particle-based polymer coatings. More specifically, they have a formula for silica particles in dry form with size in the micron range. This

formula from Fotoniq can be seen in table 3.1.

Key components included:
Dispersing agent: NeoCryl BT-24
Defoamer: FoamStar SI-2292
Binder/Polymer: NeoCryl XK-99
Thickener 1: Acrysol TT-935
Thickener 2: ReoBYK H-3300 VF

Table 3.1: Coating formula from Fotoniq for a 10wt% silica content when dry. This formula is based on silica in dry form

Components	Weight (g)	Density (g/cm³)	Solid Content (%)	Dry weight (%)
Dry silica	1.000	2.2	100	10.00
Dispersant	1.169	1.1	45	5.26
Water	1.169	1.0	0.0	0.0
Ammonia	0.060	0.09	0.0	0.0
Defoamer	0.010	0.91	9.00	0.09
Binder	19.163	1.04	44.00	84.32
Thickener 1	0.034	1.06	30.00	0.1
Thickener 2	0.091	1.06	25.00	0.23
Total	**22.787**	-	-	**100.00**

After the coating polymer mixture is made, it is applied to a glass sample using a bar coater. This stainless steel bar can create a gap of 50, 100, 150, or 200 µm gap on the surface of the glass. When the bar is dragged over the glass, a coating is applied with the desired thickness. Here the viscosity of the coating is an important characteristic. If the coating is not viscous enough, the coating will spread out after being applied to the glass. If too viscous the coating is not easily applied via the bar coat method.

While the formula created by Fotoniq is well adapted, it is based on the use of silica particles in dry form. However, in this case, the silica particles in question come in a DI water solution. This necessitated formula adaptation to incorporate the changes, where the increased amount of water was the most significant. As the silica particles provided by Alpha Nanotech are dispersed in a DI water solution, the need for a dispersing agent is eliminated. Because the Water and Ammonia in the formula are intended to activate the dispersant, they can also be removed, simplifying the formula.

However, the main hurdle is adapting to the difference in water content when using silica particles in solution. While the formula provided by Fotoniq only uses 1.169g of water to 1g of silica, the silica particles in solution have 20mg/ml silica. If taking into account that the silica has a density of 2.0 g/cm^3 and that of water 1.0 g/cm^3, then that would equate to 19.5g of water to 1g of silica. The main issue of having more water is its effect on the viscosity, as this is the most important characteristic of a good formula. For this reason, the water content of the silica solution was reduced via evaporation. AlphaNanotech's data suggest that particle suspensibility ranges from a silica volume percentage of 20%-30%, thus by employing a heated plate at 70°C with magnetic stirring enabled, a 200 mg/ml silica concentration was achieved while retaining solubility. Now 1g of silica would equate to 4.5g of water. While the amount of water was reduced, it was still 4 times more than the formula designed by Fotoniq. To retain the desired viscosity, the amount of thickeners 1 and 2 needed to be increased. Also, the amount of defoamer needed to be increased as more water would otherwise start creating foam which would leave bubbles in the coating.

As there is no true formula for finding the perfect ratios, a few attempts were done varying the amount of thickener 1, thickener 2 and defoamer. Also, the amount of binder was varied to experiment with different particle weight percentages. In this process, the silica was left out and the amount of water corresponding to 0.25g of silica in a 200 mg/ml solution was used. After a few attempts, the desired viscosity was achieved for a silica-based coating with a dry wt% of 15. The exact formula and process will be discussed in the next section.

Achieving uniform homogeneity in coating solutions is critical for replicating theoretical models. As before mixing was done by hand, which is prone to discrepancies when reproducing mixing conditions, a mixed blade was designed and 3D-printed. This not only helped with the reproducibility of the mixing but also improved material integration due to the mixer blade precisely matching the mixing cup dimensions. Concerns regarding the potential chemical interaction between the 3D-printed blade and the coating mixture were addressed by coating the blade with a two-component epoxy, selected for its documented mechanical robustness, chemical inertness, and adhesion capabilities [41]. The design for the mixer blade can be seen in Figure 3.18.

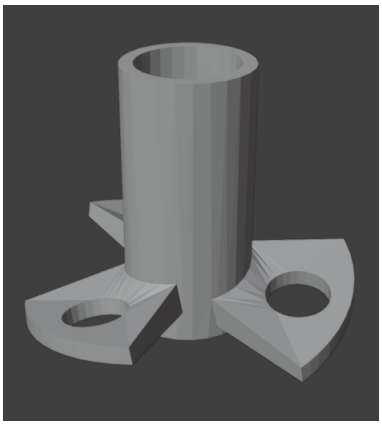

Figure 3.18: 3D printed mixer blade design for reproducible polymer mixture homogenization.

Coating production method

The optimised formula for creating a silica particle-based coating with a weight percentage of 15 can be seen in table 3.2.

Table 3.2: Coating formula used to create a 15% particle loading

Components	Wet weight (g)	Density (g/cm³)	Solid Content (%)	Dry weight (%)
Silica solution	1.37500	1.10	18.18	15.00
Defoamer	0.03000	0.91	9.00	0.16
Binder	3.18978	1.04	44.00	84.21
Thickener 1	0.01000	1.06	30.00	0.18
Thickener 2	0.03000	1.06	25.00	0.45
Total	**4.635**	-	-	**100.00**

The production formula involves sequential component mixing as specified in Table 3.2. Firstly the desired amount of silica with an increased concentration of 200 mg/ml is added to a small cup. After being combined with the defoamer, the solution is mechanically mixed at medium speed for 2 minutes. The binder is added and again mixed at medium speed for 2 minutes. The corresponding amount of thickener 1 is added and now the solution is mixed at low speed for 5 minutes. After the desired homogeneity is achieved thickener 2 is added which is first mixed by hand using a spatula and finally mechanically mixed at low speed for 5 minutes. After mixing and the coating mixture having the correct viscosity, it is applied to glass using a bar coater and left to dry for 24 hours in a fume hood.

The bar coater used could produce 4 wet thicknesses (t_{wet}), namely 50,100,150, and 200 µm. For this reason, these 4 thicknesses were made for each of the three particle diameters with a dry weight percentage of 15. Coatings were also made for each thickness where the silica was left out of the production process. In other words, the silica solution used in the formulation shown in table 3.2 was replaced by the equivalent amount of water. The process was further unaltered. These coatings were made to explore the effects of coating consisting of only the polymer without scatter particles. Pictures of all the coatings for t_{wet} = 100 µm can be seen in Appendix B.

Apart from the 16 above-mentioned coatings, for each particle size, a double coating was made. The goal was to explore the possibility of particles extruding from the coating and its potential effects, as the particle size is in the same order of magnitude as the dry coating thickness. To do this, for each particle size, a layer of t_{wet} = 50 µm was applied. This was then dried for 24 hours before applying another coating over the top where again t_{wet} = 50 µm. One of the layers was only the polymer mixture whereas the other layer was a particle-based coating. Both combinations were made. A schematic can be seen in Figure 3.19.

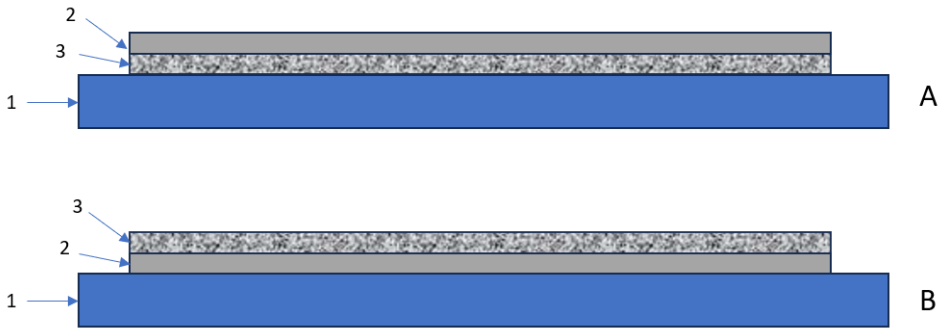

Figure 3.19: Double coating schematic. 1. Optiwhite glass, 2. Only polymer (t_{wet} = 50um) , 3. 15wt%, (d= 5 µm, t_{wet} = 50 µm). A = Only polymer on top and B = Only polymer on the bottom.

Before applying the second coating, the sides were removed by about 5mm to make room for the bar coater as this needed to be level on the glass.

Determining Coating Thickness

To be able to simulate the coatings created, the dry thickness needed to be determined. It turns out that this is not a trivial task, as this needed to have accuracy in the micron range. With the only profilometer available being in a cleanroom, measuring each coating was not an option. Luckily 1 coating was able to be measured, which was chosen to be the polymer coating without silica particles made with a wet thickness of t_{wet} = 100 µm. The profilometer result, accompanied by a schematic overview of the measured path can be seen in Figure 3.20.

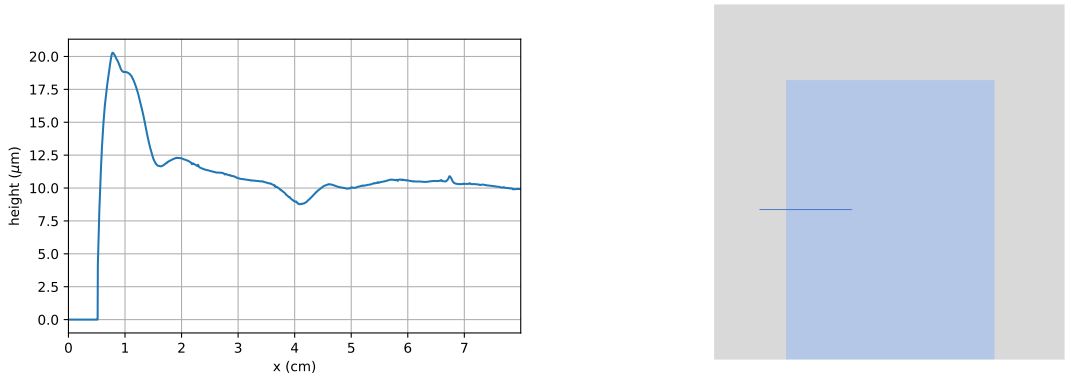

Figure 3.20: Profilometer data of a coating without silica with t_{wet} = 100 µm with (a) the measurement of the height over position and (b) a schematic showing the measurement line of the profilometer. The grey square is the glass, the light blue square is the coating and the solid line is the profilometer path.

It can be seen that while the edges of the coating have a larger value, the middle of the coating is approximately 10 µm. This shows that for polymer coatings without silica, about 10% of the wet thickness remains after drying. This fact is used to estimate the thickness of all coatings. In the case of

coatings containing a 15 weight percentage silica, which corresponds to an 8.55 volume percentage, the remaining 91.45% is reduced by a factor of 10.

4

Results

4.1. Hortiscatter Results

In the following section, the Hortiscatter (HS) results will be discussed comprehensively. First, some general results and remarks on the optimized HS setup will be provided. This will be followed by a detailed documentation of both measurement and simulation results of HS.

The discussion will begin with the results for plain Optiwhite glass, providing a baseline for subsequent comparisons. Following this, the HS results for coatings without silica particles will be shown for the four different coating thicknesses produced. Next, the results for coatings containing silica particles will be presented, starting with the smallest particle size and progressing to larger sizes. Each subsection will provide insights into how particle size influences HS outcomes. Finally, the HS results for double coatings will be discussed for all particle sizes, examining how the layering affects scattering properties.

This structured approach will allow for a clear comparison between different coatings and particle sizes, facilitating a deeper understanding of the scattering behavior under various conditions. For all simulations, $1 \cdot 10^5$ photons were used. While using more photons would yield less noisy results, the simulations took 4 hours each due to the need to simulate the HS for each wavelength individually. As the general shape was visible, it was decided not to increase the number of photons.

4.1.1. Measurement Reproducibility

It was found that when conducting HS measurements, slight movements of the sample could lead to vastly different results, affecting the HS values by up to $\pm 20\%$. This is assumed to be due to the non-homogeneity of the coatings, where inconsistencies such as small air bubbles were visible to the naked eye. These inconsistencies significantly influenced the scattering of the coating. As the acceptance area of the detector on the sample is in the mm^2 range, a local inconsistency could greatly affect the scattering effects. Therefore, it was important to avoid any coating inconsistencies when choosing the measurement location.

4.1.2. Reference Measurement

Examining the reference measurement can indicate the quality of aspects of the setup. The angle-dependent intensity measured with the HS setup is shown in Figure 4.1, normalized to the zero angle intensity.

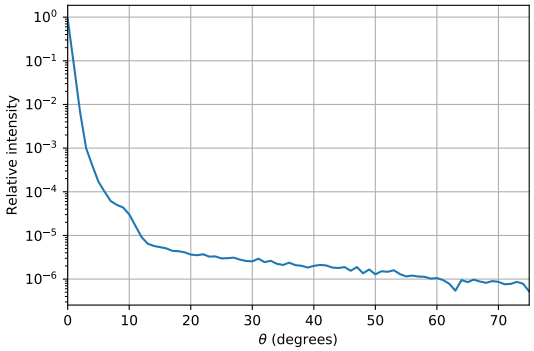

Figure 4.1: Reference measurement of the HS setup. The intensity is normalized to the zero angle intensity.

As mentioned in section 3.2.2, where the final HS setup was discussed, the detector view area during the reference measurement was still partially looking through the diaphragm at $\theta = 1°$. This allowed unwanted light to be detected. In this case, the intensity at $\theta = 1°$ was 9% of what was detected at $\theta = 0°$. This number reduced to 0.7% for $\theta = 2°$. Additionally, a small plateau is present at around $\theta = 10°$, indicating that somehow light is disturbing the measurement.

The possible consequences of these effects, as well as recommendations for improvements, are detailed in section 5.1.

4.1.3. No Coating

First, the HS values were measured for Optiwhite glass, which can be seen in Figure 4.2. It shows that noise is present in the measurement values at lower and higher wavelengths, disrupting the results. While the reason for this noise will be discussed in section 5.1, it was decided to show only the HS values between 400 and 1000 nm for all subsequent sample measurements. The simulation consistently shows noisy data due to the number of photons simulated.

Furthermore, when looking at Figure 4.2, it is remarkable that the simulation gives near-zero values while the measurement gives much higher values. For the measurement, it starts at 10% and linearly decreases towards 2% at 1000 nm. For the simulation, the HS is not wavelength-dependent and gives values around $1 \cdot 10^{-4}$%. Initial thoughts for the measured scatter of Optiwhite include potential surface roughness scattering or impurity scattering, both of which are not implemented in the simulation. These possibilities will be discussed further in section 5.2.1.

Finally, it can be seen that there is a small peak at 825 nm. This was present in almost all HS measurements done for the different coatings and was found to be due to over-saturation of the spectrometer. The reason it was not possible to remove this effect will be discussed in section 5.1.

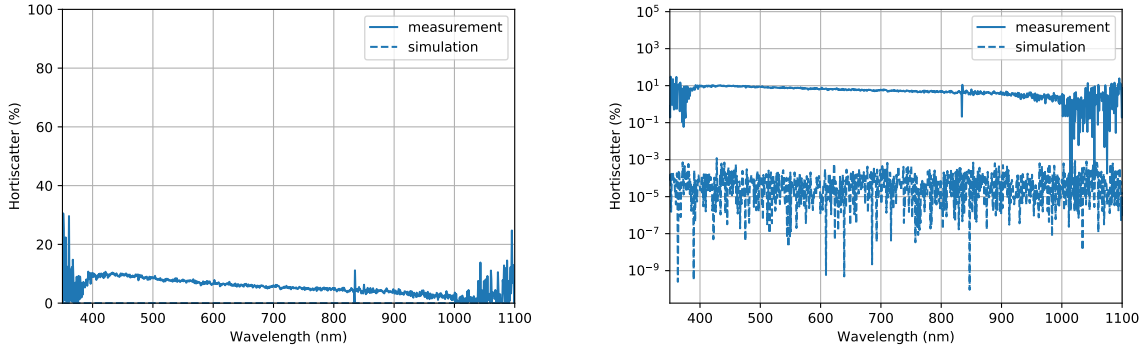

(a) Normal scale **(b)** Log scale

Figure 4.2: Hortiscatter measurement and simulation of Optiwhite glass shown in (a) normal scale and (b) log scale.

4.1.4. Coating Without Silica

Next, the HS results for the coatings without silica for all four thicknesses will be presented. The wavelength-dependent HS values between 400 and 1000 nm can be seen in Figure 4.3. Again, it is noticeable that the simulations give much lower values than the measurements.

For the simulations, there is no visible difference in HS between thicknesses, with values similar to that of Optiwhite around $1 \cdot 10^{-4}$% with noisy data. As with plain Optiwhite, no scattering is implemented in the simulation due to the absence of silica scatter particles. Thus, the simulations are still solely based on the Fresnel equations.

From viewing the measurement values, it can be seen that, unlike plain Optiwhite, almost no wavelength dependence is present in the HS values. Except for t_{wet} = 200 µm, the HS values are similar to the largest HS value found for plain Optiwhite. This indicates that new elements, which are not simulated, such as surface roughness, play a role. This will be discussed in further detail in section 5.3.1.

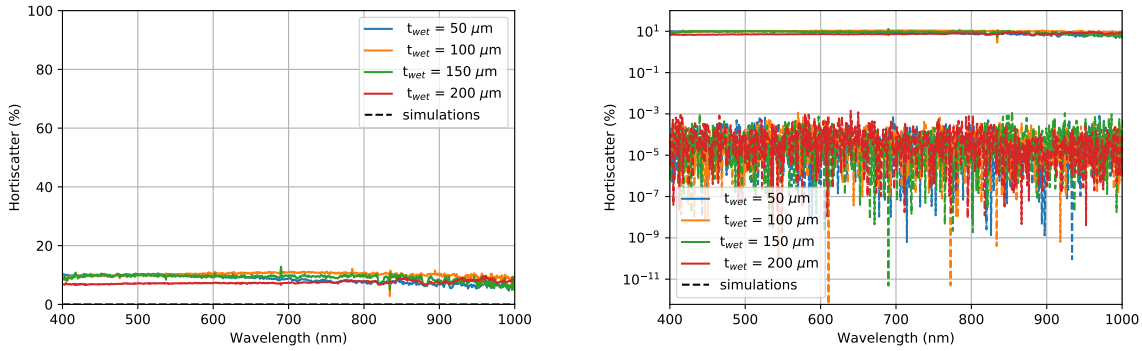

(a) Normal scale **(b)** Log scale

Figure 4.3: Hortiscatter measurement and simulation of coatings without silica shown in (a) normal scale and (b) log scale.

For the thickest coating with t_{wet} = 200 µm , which stands out in the HS measurements, inconsistent results were found. Looking through the sample revealed a warped view. While this effect was present in all coatings, it was much more pronounced here. This was attributed to large-scale surface roughness in the range of 1 mm^2, showing characteristic of non-homogeneous drying, although difficult to capture by camera. The profilometer measurement in Figure 3.20a shows that micron-scale surface roughness is also present in the coating with t_{wet} = 100 µm. While visible with the naked eye, more scattering was

observed for the t_{wet} = 200 µm coating. How this visible enhanced large-scale surface roughness might play a role in giving inconsistent HS results will also be discussed in further detail in section 5.3.1.

4.1.5. Coating with d = 160 nm

Silica particles with a diameter of d = 160 nm are now added to the coatings. Minimal particle agglomeration is visible with the naked eye, spread throughout the coating. The coating appears hazy with very fine white particles dispersed on average a few mm apart.

As with previous samples, measurements again yield much higher HS values than simulations, as shown in Figure 4.4. They also show a clear thickness dependence, with higher HS values corresponding to increased t_{wet}. This is expected, as thicker coatings contain more silica scatter particles. This trend is most evident at shorter wavelengths. Simulation results also show a thickness dependence, which now incorporates scattering due to silica particles.

While a similar shape is observed in measurements and simulations, they occur on different scales, with measurements showing much larger values. The HS for measurements decreases steeply at wavelengths shorter than 550 nm, followed by a less steep decrease at longer wavelengths, showing some characteristics of exponential decay, although minimal. This is confirmed by the slowly decreasing, straight line in the log scale plot in Figure 4.4b.

Simulations, however, show much lower HS values and an exponential decrease towards longer wavelengths. This significant difference between simulation and measurement indicates that the simulation does not fully capture all relevant physical properties of the coatings. To gain more insight into the origin, simulation input parameters will be varied in section 5.4.1.

Additionally, at longer wavelengths, disturbances between 675 and 900 nm can be seen in the measurements. This was slightly visible in the coatings without silica, as seen in Figure 4.3a, but is now more apparent. This is likely due to the signal-to-noise ratio, discussed in section 5.1 on the general HS setup. Also, noise in HS simulations becomes more visible at lower HS values.

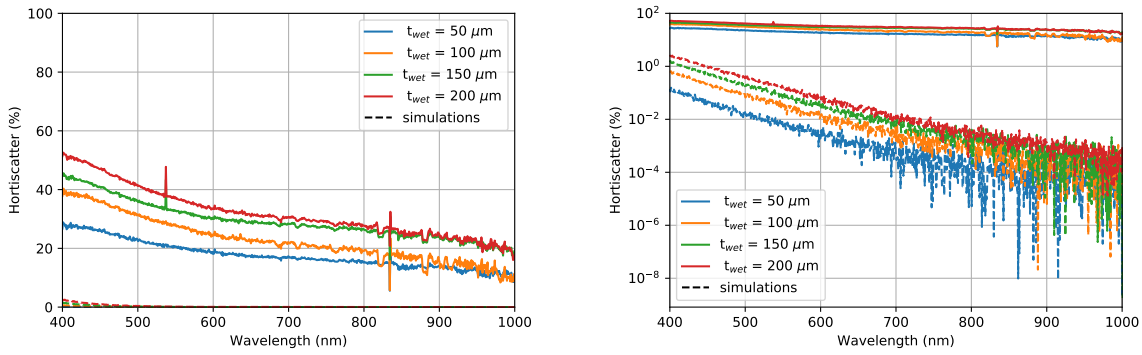

(a) Normal scale **(b)** Log scale

Figure 4.4: Hortiscatter measurement and simulation of d = 160 nm coatings shown in (a) normal scale and (b) log scale.

4.1.6. Coating with d = 400 nm

For the particles with a diameter of d = 400 nm, a similar trend in HS is seen compared to d = 160 nm, as shown in Figure 4.5. Measurements yield much higher HS values than simulations, but both measurements and simulations show an increase in HS with larger thicknesses. Additionally, an exponential decay is observed, visible as an almost straight line on the log scale. Comparing the log scale plots, it can be seen that the exponential decrease is slightly less steep than for d = 160 nm, but HS values are larger. The similarities and differences will be discussed in more detail in section 5.5.1.

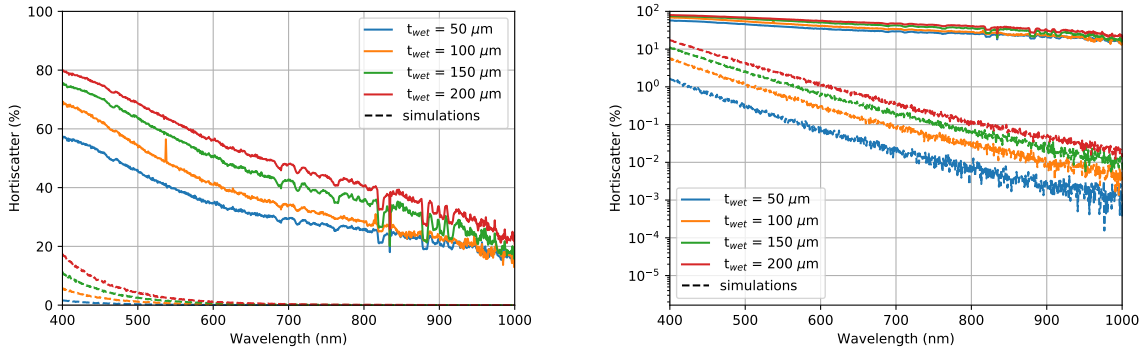

(a) Normal scale **(b)** Log scale

Figure 4.5: Hortiscatter measurement and simulation of d = 400 nm coatings shown in (a) normal scale and (b) log scale.

4.1.7. Coating with d = 5 µm

For the largest particle size with a diameter of d = 5 µm, vastly different results occur compared to the other particle sizes, as shown in Figure 4.6.

Firstly, the measurements show large and almost wavelength-independent HS values. A clear increase in HS corresponding to the coating thickness is visible, similar to the other coatings containing silica. While for most coatings, the HS shifts towards lower values for increasing wavelengths, for t_{wet} = 50 µm a different shape can be seen, slightly increasing HS when heading to longer wavelengths. For the other thicknesses, while minimal, the opposite is true. This indicates a small difference in the properties of the thinnest coating, which will be discussed in further detail in section 5.6.1.

For the simulations, a new shape is observed compared to the exponentially decaying HS seen for the smaller particle sizes. While exponential decay is still present for wavelengths above 600 nm, visible as a straight line in Figure 4.6b, a less clear, non-exponential pattern is seen for shorter wavelengths.

For d = 160 nm and d = 400 nm, both measurement and simulation showed exponential decay, albeit with different magnitudes and speeds of decay. However, for d = 5 µm, the measurements show almost no decay, and the simulations diverge from exponential decay at shorter wavelengths. The potential reasons for these effects will be discussed in section 5.6.1.

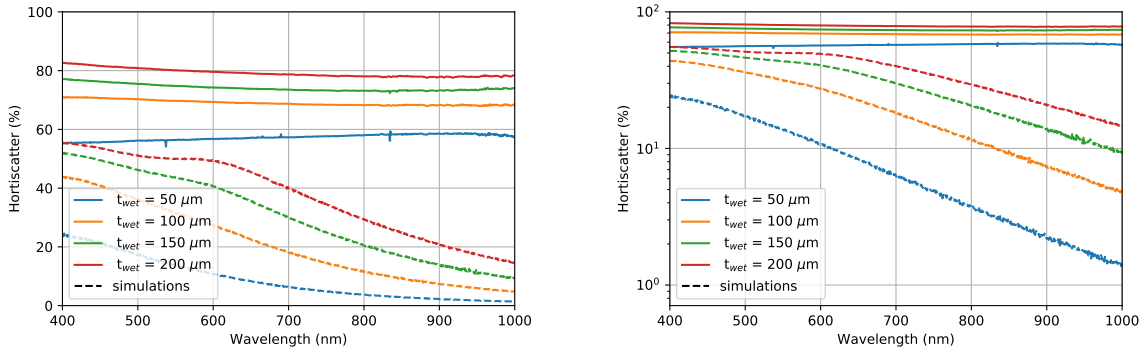

(a) Normal scale **(b)** Log scale

Figure 4.6: Hortiscatter measurement and simulation of d = 5 µm coatings shown in (a) normal scale and (b) log scale.

4.1.8. Double Coatings

Finally, the HS of the double coatings for each particle size is shown in Figure 4.7. The reason for producing these coatings was the assumption that when the diameter of the particles approached the same order of magnitude as the coating thickness, they might extrude from the polymer.

For the silica with d = 160 nm and d = 400 nm, there is minimal difference between the two coatings. However, for d = 5 µm, a significant difference is observed. For coating A, where there is only silica in the bottom layer, the HS values are about 10% higher than for coating B. Coating A matches the shape of the HS measured for the single coatings of d = 5 µm shown above for t_{wet} = 100 µm, 150 µm, and 200 µm. On the other hand, coating B matches the shape of t_{wet} = 50 µm, which differed from the rest. Both the magnitude and shape of coating A would replace t_{wet} = 50 µm well in the single coating HS measurement based solely on the pattern seen when decreasing the coating thickness.

From this, it can be seen that indeed something different happens for the largest particle size. How this exactly explains the observations will be discussed in further detail in section 5.6.1.

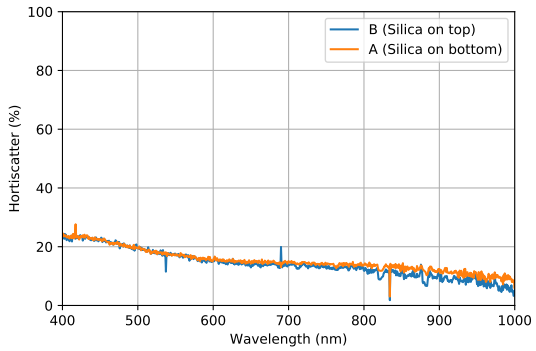

(a) d = 160 nm

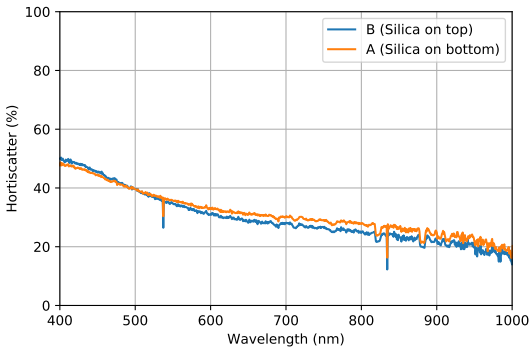

(b) d = 400 nm

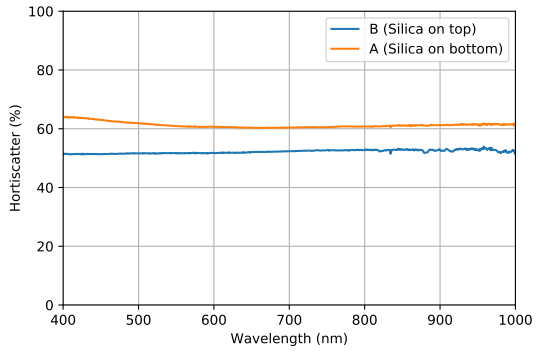

(c) d = 5 µm

Figure 4.7: HS measurements of double coatings

4.2. Hemispherical Transmittance Results

In this section, the results of both measurements and simulations of the Hemispherical Light Transmission (HLT) will be documented. To facilitate a thorough comparison, both the HLT values and the angle-dependent transmission will be presented.

The structure will follow the same order as the HS results. First, the HLT results for plain Optiwhite glass will be shown. Next, the HLT values for coatings without silica particles will be presented, covering the four produced coating thicknesses. Following this, the HLT results for coatings containing silica particles will be discussed, starting with the smallest particle size and progressing to larger sizes. Finally, the

HLT results for double coatings will be examined for all particle sizes. For all of the following HLT simulations, the amount of Monte Carlo rays was set to $1 \cdot 10^6$.

4.2.1. No Coating

To start with the most simplistic case, the simulated and measured transmittance values of plain Optiwhite are compared. These can be seen together with a measurement done by Wageningen University & Research (WUR), which also measured Optiwhite glass with their HLT setup. The results can be seen in Figure 4.8.

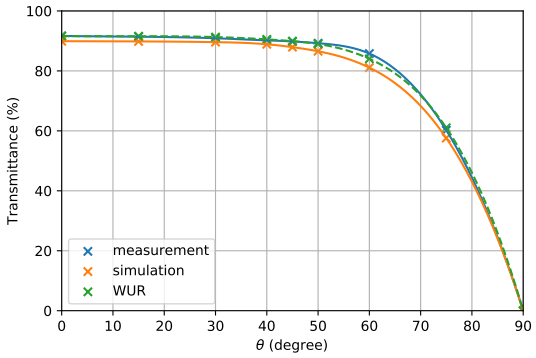

Figure 4.8: Angle-dependent transmittance according to formula 2.19 for the simulation, measurement, and measurement done by WUR. The crosses represent the measured or simulated data, and the solid lines are the cubic interpolated data.

It can be seen that the transmittance is not 100% with a perpendicular angle of incidence $\theta = 0°$. As θ increases, the transmission decreases. This behaviour aligns with the Fresnel equations shown in equation 2.7, which indicates reflection at normal incidence (θ = 0°) due to a difference in refractive index between two surfaces. This reflection increases with increasing θ.

The HLT values corresponding to the angle-dependent transmission are:

Measurement:	84.48 %
Simulation:	82.09 %
Measurement WUR:	84.33 %

It can be seen that the measured values are very similar to those from WUR, which is reflected in the HLT value. On the other hand, the simulation consistently gives lower values across each angle, with the largest difference at $\theta = 60°$. The difference in HLT value between simulation and measurement is 2.24%.

Since the simulation only uses Fresnel equations at this point, there is an indication that the input parameters for n and k of Optiwhite in the simulation may be incorrect. This will be discussed in further detail in section 5.2.2.

4.2.2. Coating Without Silica

Next, the coatings without silica are compared. This will be done for all four thicknesses: t_{wet} = 50 µm, 100 µm, 150 µm, and 200 µm. First, the measurements are plotted together in one figure and the simulations in another. These can be seen in Figures 4.9a and 4.9b, respectively. The corresponding HLT values for each can be found in Table 4.1. Finally, to compare the measurement and simulation directly, the t_{wet} = 200µm results will be shown together in one graph, which can be seen in Figure 4.10. The largest thickness was chosen for comparison, as it is expected to show the most effect when particles are added. This method of comparing measurements and simulations will be repeated for the rest of the coatings.

From Figure 4.9, it can be seen that both simulations and measurements expect minimal to no difference in HLT when increasing coating thickness. This is reflected in the HLT values seen in Table 4.1,

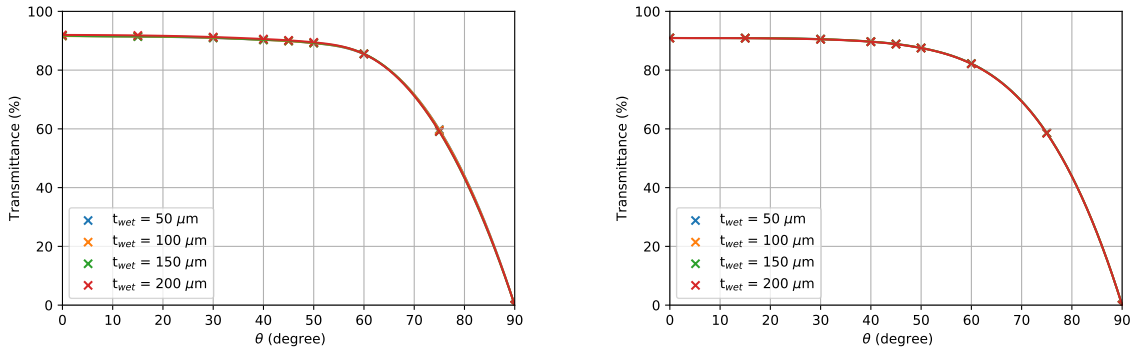

(a) Measurement **(b)** Simulation

Figure 4.9: Angle-dependent transmittance according to formula 2.19 for the simulation and measurement for the four thicknesses t_{wet} of the coatings made without silica.

where minimal differences are observed. While the simulations expect a decrease of 0.01% when increasing t_{wet} from 100 µm to 200 µm, this is of the same order of magnitude as the HLT simulations and is not considered significant.

While the measurements show a similar pattern, the t_{wet} = 200 µm measurement appears to have slightly larger transmission. As discussed in the HLT results in section 4.1.4, this coating visually showed more large-scale surface roughness than the other coatings. How this might cause a minimal increase in HLT will be discussed in section 5.3.2.

t_{wet} (µm)	t_{dry} (µm)	HLT measurement (%)	HLT simulation (%)
50	5	84.37	83.13
100	10	84.37	83.13
150	15	84.34	83.12
200	20	84.49	83.12

Table 4.1: Comparison of HLT measurement and HLT simulation for different sample configurations.

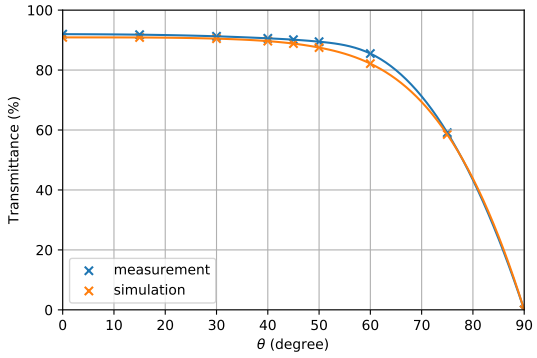

Figure 4.10: Angle-dependent transmittance according to formula 2.19 for the simulation and measurement for t_{wet} = 200 µm for the coating without silica.

From Figure 4.10, it can be seen that, like for Optiwhite glass, the simulation consistently gives lower transmission values. However, the difference is smaller than before, which can be seen in the HLT values. The differences in HLT between measurement and simulation are all less than 1.5%, whereas for Optiwhite the difference was 2.24%. However, similarly to the situation without coating, this indicates that the simulation input parameters may be slightly incorrect, as at this point the simulation only uses

Fresnel equations on smooth surfaces. This will be discussed in more detail in section 5.3.2, where relevant simulation parameters will be varied.

4.2.3. Coating with d = 160 nm

Now, silica particles with a diameter of d = 160 nm are added to the coating.

When looking at the HLT values in Table 4.2, it can be seen that the differences between simulations and experiments are all below 1%. However, there seems to be a better match for the smaller coating thicknesses, where the difference increases with increasing coating thickness. As mentioned in the HS results in section 4.1.5, the simulation now takes particle scattering due to silica into account. This may indicate that the coating thickness used for the simulations is incorrect. The possibility of varying the input parameters to explain the slight mismatch of HLT will be discussed further in section 5.4.2.

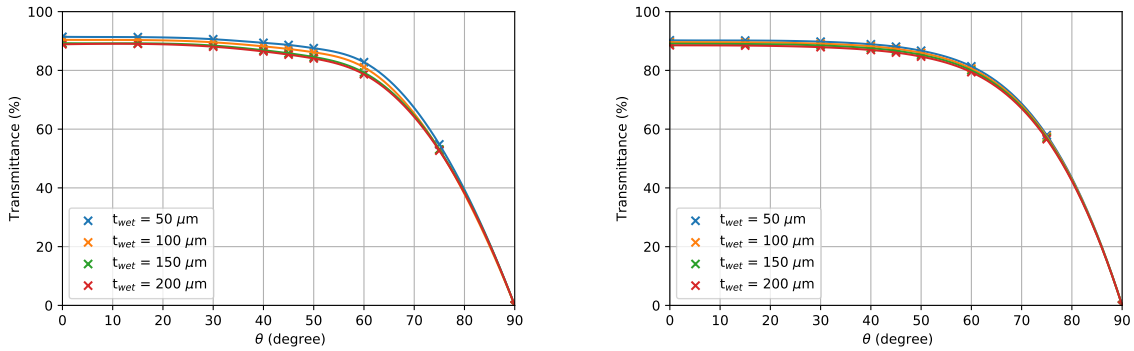

(a) Measurement **(b)** Simulation

Figure 4.11: Angle-dependent transmittance according to formula 2.19 for the simulation and measurement for the four thicknesses t_{wet} of the coatings made with silica with d = 160 nm.

t_{wet} (µm)	t_{dry} (µm)	HLT measurement (%)	HLT simulation (%)
50	8.9	82.68	82.31
100	17.7	81.33	81.64
150	26.5	80.15	81.04
200	35.4	79.73	80.49

Table 4.2: Comparison of HLT measurement and HLT simulation for d = 160 nm.

When looking at the transmission data from the measurements in Figure 4.11a, it can be seen that for lower angles, the most difference in transmission between the thicknesses is observed. At $75°$, the difference is the smallest. When looking at the corresponding simulation data in Figure 4.11b, the same shape can be seen. However, the variation in transmission between the thicknesses is less pronounced, which is most visible when comparing at $\theta = 60°$. This may have a similar origin as described above for the single HLT values.

Finally, when comparing both simulation and experiment in Figure 4.12, it can be seen that there is good overlap at all data points except at $75°$. Until now, the largest differences were seen at $\theta = 60°$. It is also noticeable that the measurement gives lower transmittance values at certain angles compared to the simulation, whereas for the cases without particles or without coating, this was never true. The effect of varying the simulation input parameters on the shape of the angle-dependent transmission curves will be discussed in section 5.4.3.

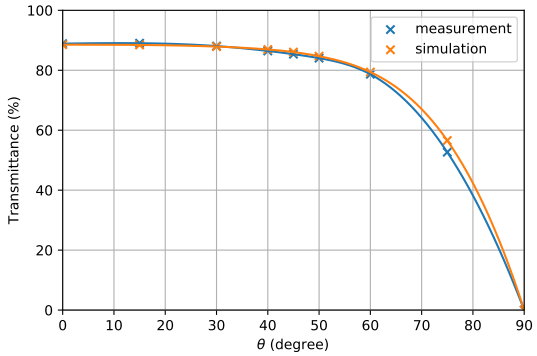

Figure 4.12: Angle-dependent transmittance according to formula 2.19 for the simulation and measurement for t_{wet} = 200 µm for the coating with silica with d = 160 nm.

4.2.4. Coating with d = 400 nm

When looking at the coatings containing particles with a diameter of d = 400 nm, the spread in angle-dependent transmission between thicknesses follows a similar pattern for both measurement and simulation, as seen in Figure 4.13. For both, the largest thickness dependence can be seen at angles $\theta = 50°$ and $60°$, whereas the least thickness dependence can be seen at $\theta = 75°$. As also seen for the particles with d = 160 nm, the spread between thicknesses is again larger for the measurements compared to the simulations. From the HLT values shown in Table 4.3, it can be seen that the match decreases with increasing coating thickness.

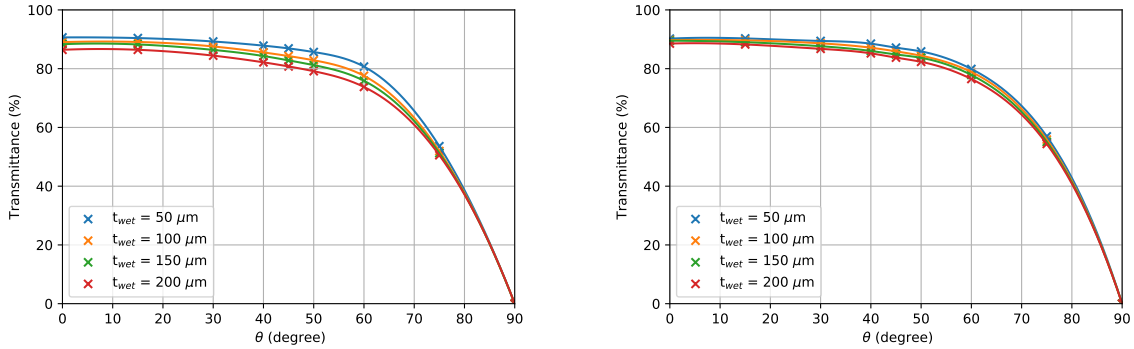

(a) Measurement **(b)** Simulation

Figure 4.13: Angle-dependent transmittance according to formula 2.19 for the simulation and measurement for the four thicknesses t_{wet} of the coatings made with silica with d = 400 nm.

t_{wet} (µm)	t_{dry} (µm)	HLT measurement (%)	HLT simulation (%)
50	8.9	80.47	81.64
100	17.7	79.00	80.56
150	26.5	77.77	79.64
200	35.4	75.95	78.80

Table 4.3: Comparison of HLT measurement and HLT simulation for d = 400 nm.

Finally, when looking at the comparison between measurement and simulation in Figure 4.14, it can be seen that the simulation consistently gives higher values for the transmission. This is the opposite of what was seen for the coatings without silica, where the simulation gave lower transmittance values. Besides the constant offset, the biggest mismatch is again seen at $\theta = 75°$, but also slightly between $40°$ and $50°$.

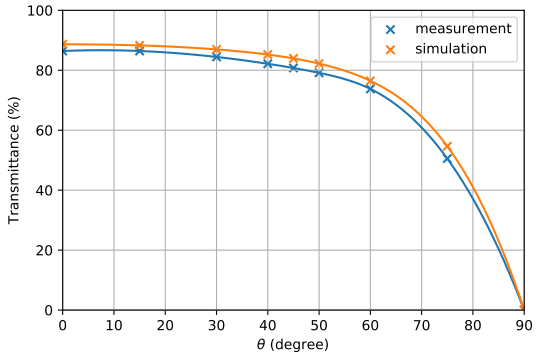

Figure 4.14: Angle-dependent transmittance according to formula 2.19 for the simulation and measurement for t_{wet} = 200 µm for the coating with silica with d = 400 nm.

4.2.5. Coating with d = 5 µm

For the final particle size, it can be seen in Figure 4.15 that there is little overlap between measurement and simulation. The general shape of the angle-dependent transmission, as seen before, is largely disturbed.

For the simulations in Figure 4.15b, the transmittance at lower angles is independent of thickness, whereas at larger angles, the transmission decreases for thicker coatings. When looking at the measurements in Figure 4.15a, this pattern is not seen. Firstly, an increase in transmission is seen when going from $\theta = 0°$ to $\theta = 15°$. Secondly, a strong decrease is seen for angles above $\theta = 40°$. As these effects differ largely from what is seen in the simulations, it is expected that this is due to effects not implemented in the simulation. This will be discussed in more detail in section 5.6.3.

From the HLT values shown in Table 4.4, it can be seen that the match between simulation and measurement strongly decreases with increasing thickness.

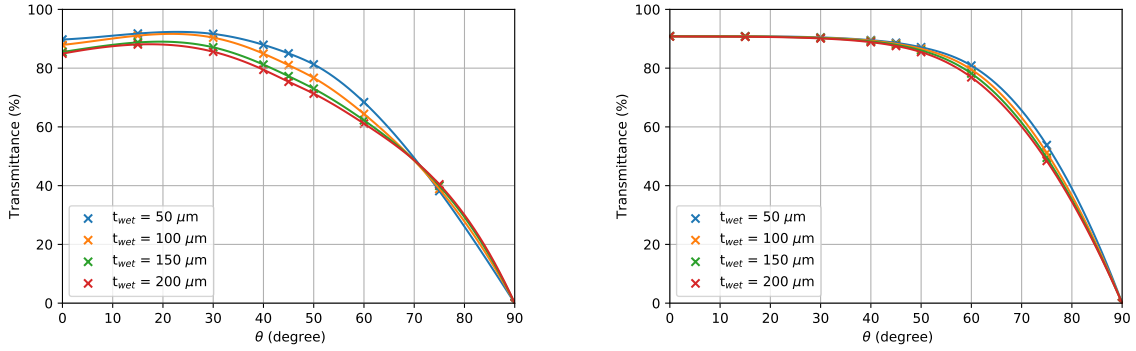

(a) Measurement **(b)** Simulation

Figure 4.15: Angle-dependent transmittance according to formula 2.19 for the simulation and measurement for the four thicknesses t_{wet} of the coatings made with silica with d = 5 µm.

t_{wet} (µm)	t_{dry} (µm)	HLT measurement (%)	HLT simulation (%)
50	8.9	76.61	82.03
100	17.7	74.38	81.26
150	26.5	71.96	80.61
200	35.4	70.80	80.05

Table 4.4: Comparison of HLT measurement and HLT simulation for d = 5 µm.

When directly comparing measurement and simulation in Figure 4.16, it is clear that the measurement shows much lower values at angles $\theta = 45°$, $50°$, and $60°$. The increase seen in the measurement when going from $\theta = 0°$ to $\theta = 15°$ seems to decrease the difference. As this increase is difficult to explain using theory, there is an indication that this might be an effect of the measurement setup. This will be discussed in more detail in section 5.6.3.

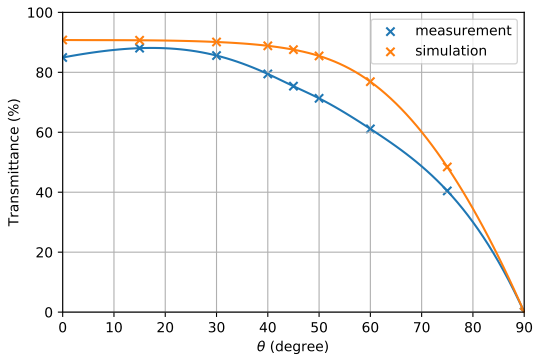

Figure 4.16: Angle-dependent transmittance according to formula 2.19 for the simulation and measurement for t_{wet} = 200 µm for the coating with silica with d = 5 µm.

4.2.6. Double Coatings

As mentioned in section 3.4 on the coating production, double coatings were made for each particle size to explore the possibility of particles extruding from the coating and its potential consequences. The measurements of these double coatings can all be seen in Figure 4.17. It can be seen that for the particles with diameter d = 160 nm and 400 nm, there is minimal difference in the angle-dependent transmission. However, when looking at d = 5 µm, a difference can be seen. There, at higher angles $\theta = 60°$ and $75°$, the transmission decreases strongly in the coating where the layer containing silica is on the top. The origin of the found difference will be discussed in further detail at the end of section 5.6.3.

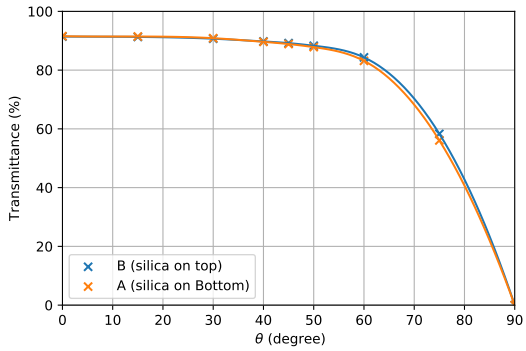

(a) d = 160 nm

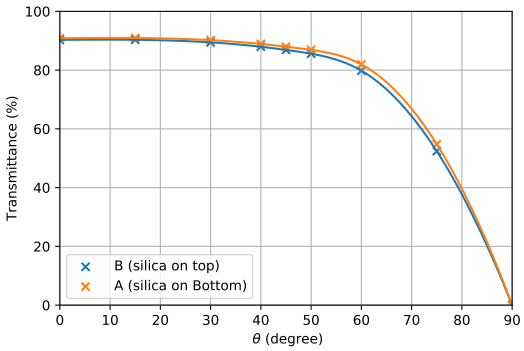

(b) d = 400 nm

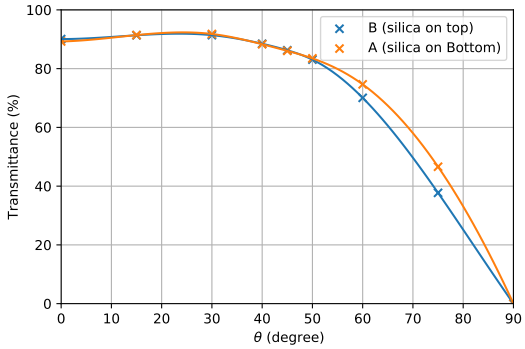

(c) d = 5 µm

Figure 4.17: HLT measurements of double coatings.

5

Discussion & Recommendations

This section will consist of a discussion of the found results. First of all, the general HS setup will be discussed where issues arose concerning for example the signal-to-noise ratio. Afterwards, the results of HS and HLT will be discussed in the same order for each sample type starting off with plain Optiwhite, then for the coatings without silica and finally the coatings containing silica in order of increasing particle size. A list of all recommendations detailed in this discussion is summarised together in Appendix A.

5.1. HS setup

First, the general results of the HS setup will be discussed. Initially, the measurement reproducibility will be examined as this turned out to be an issue. Next, the effects of the reference view area still looking through the diaphragm will be reviewed. Finally, the discovered problem with the signal-to-noise ratio will be addressed.

Reproducibility

An issue that arose during HS measurements was the inconsistency depending on the measurement location. This was found to be due to a combination of the non-homogeneity of the coatings and the small acceptance area of the detector. A way to improve this would be to measure at multiple locations and take the average. However, with the current setup, this would take 36 minutes per measurement at each new location. If the integration time could be reduced using the above-mentioned suggestions, this time may be decreased. While this might result in an average spatial dependence of the coating, the scatter is still measured across only a single azimuth angle ϕ. This would be no problem if the coatings scatter light isotropically, but in reality, this may not always be the case. Due to the coatings only reaching the edge of the glass at one location, it was not possible to simply rotate the glass. Thus, creating a sample holder that allows for the rotation of the coating to average out the scattering distribution over multiple angles ϕ may further improve results.

Reference view area

From the reference measurement shown in Figure 4.1, it was found that 9% of the measured intensity at θ = 0° was still visible at θ = 1°, which further decreased to values below 0.7% more slowly at higher angles. This relatively high 9% is assumed to be due to the detector view area still partially passing through the diaphragm, detecting unwanted light. While at this point it is unclear if further reducing this number would significantly improve the HS results, it can easily be fixed in future setups by increasing the distance between the detector and the diaphragm as described in Figure 3.7.

From the reference intensity in Figure 4.1, it can also be seen that there is a small plateau present at around 10°. It seems that the intensity temporarily stops decreasing with increasing angle. By looking at the wavelength-dependent intensities, it was found that the size of this bump scaled with the intensity from the source. This indicates that light was leaking from the source into the detector via unintended paths. As the box created around the setup, with the goal of only letting in light through

the diaphragm, was not perfect, it would be advisable in future setups to improve the isolation from external light, allowing only light to enter through the diaphragm.

Signal-to-noise ratio

When performing HS measurements, issues arose due to the signal-to-noise ratio. Looking at the HS measurement results in Figure 4.2a, noise can be seen on both sides of the figure. This can be attributed to the low intensity of the source, as shown in the zero-angle reference measurement in Figure 5.1.

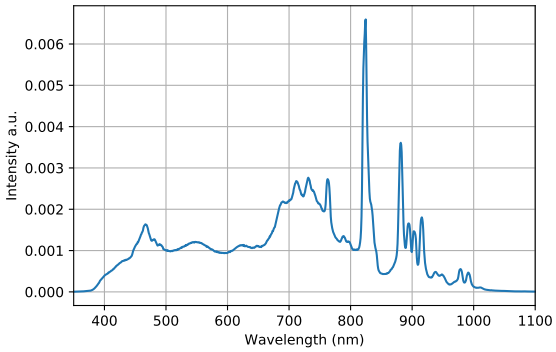

Figure 5.1: Beam source spectrum taken from the HS reference measurement at $\theta = 0°$.

Measuring HS in a wavelength regime where the source has relatively low intensity seems to cause issues. With the correct intensity, assuming nonzero scattering and no background noise, more counts are found for the sample with respect to the reference measurement at all angles above $\theta = 0°$. However, when the intensity of the source is low and (minimal) background noise is present, the counts from sample scattering can enter the same regime as the background noise for higher angles. In this case, there will be little to no measured scattering from the sample at higher angles, resulting in a lower HS value. This can be seen in Figure 4.2a as a decrease in the HS value when going to shorter wavelengths than 400 nm. This is also the regime where the source rapidly starts decreasing in intensity, as seen in Figure 5.1, which shows the beam source spectrum. When the intensity of the source continues to decrease, the scattered photons will enter the noise regime at even lower angles. In this case, the found values are almost completely determined by noise, giving extremely fluctuating values due to the use of a normalized angle-dependent spectrum. This can be seen in Figure 4.2a for wavelengths below 400 nm and above 1000 nm. The angle-dependent intensity for three wavelengths in the three discussed regimes from the HS measurement of Optiwhite can be seen below in Figure 5.2.

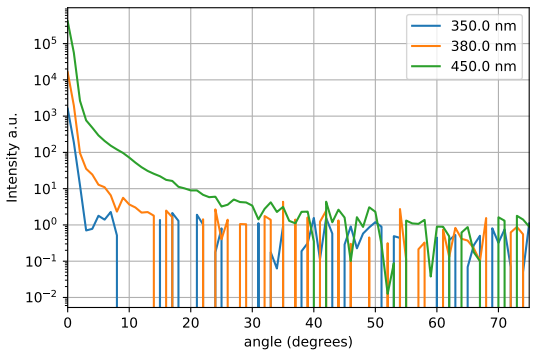

Figure 5.2: The angle-dependent intensity measured from the HS setup of plain Optiwhite for three wavelengths.

From this, it can be seen that for decreasing wavelengths, the intensity of the source decreases, re-

sulting in the measured intensities entering the background regime starting from lower angles. For this reason, the wavelength-dependent HS values will only be discussed between 400 nm and 1000 nm as these give the best result.

This demonstrates the importance of a good signal-to-noise ratio in this setup, where a higher-intensity source would give better results. While increasing the integration time may help the signal-to-noise ratio, this is strongly limited by the wavelengths with a high intensity of the source, in this case, the peak at 825 nm. This can already be seen in almost all HS measurements where an unexpected peak is visible at 825 nm, which is due to (near) oversaturation of the spectrometer. This highlights the difficulty of a strongly varying intensity of the source, which, without a neutral-density filter, causes oversaturation at certain wavelengths for the shortest spectrometer integration time but gives very low intensities for other wavelengths. Ideally, a source should be found with a more constant spectrum where no neutral-density filter is needed, thus not blocking UV in the 300-350 nm range. This would increase the intensity at lower wavelengths, and due to the more constant wavelength dependence of the intensity, the integration time of the spectrometer can be better matched to all wavelengths.

5.2. No coating

The results of measurements and simulations of plain Optiwhite will be compared, and potential explanations for the differences will be discussed. This section is divided into three parts: the wavelength-dependent HS, the single-valued HLT comparison between measurement and simulation, and a detailed discussion of the angle-dependent transmission, highlighting discrepancies in the angle dependence.

5.2.1. Hortiscatter

From the HS results of plain Optiwhite glass, as shown in Figure 4.2a, it was found that between 400 and 1000 nm, measurements indicated a nonzero HS value while simulations showed a wavelength-independent near-zero HS. For the measurements, a seemingly linear decrease is observed, starting at 10% at 400 nm and decreasing to around 2% at 1000 nm. In contrast, the simulations yielded a fairly constant HS. Currently, the simulation does not account for any type of scattering and only uses Fresnel equations applied to smooth surfaces. A small HS value of around $1 \cdot 10^{-4}$% is found due to the source having an aim sphere between 0 and 1 degrees, as discussed in section 3.1.2.

This mismatch between measurement and simulation strongly indicates that some kind of scattering is present in the plain Optiwhite sample. The two potential types of scattering are impurity scattering within the glass and surface scattering due to surface roughness. Both are not implemented in LightTools and will be discussed individually.

Impurity scattering

Glass is produced to have low scattering and high transmission, but it is known to have impurities with sizes often smaller than the wavelength of visible light, causing Rayleigh scattering [42]. Rayleigh scattering typically results in larger scattering for shorter wavelengths [43], which is observed in the HS measurements. However, this relationship usually follows a $1/\lambda^4$ dependence, which is not reflected in the HS measurements. It could be that the HS calculation method does not properly reflect this wavelength dependence. To confirm this, the measured sample intensities at θ = 14° were normalized by their corresponding zero-angle intensities. From this, the scatter intensity ratio for each wavelength was determined and fitted according to the function $y = a/(\lambda - c)^4 + b$. This is shown in Figure 5.3 below.

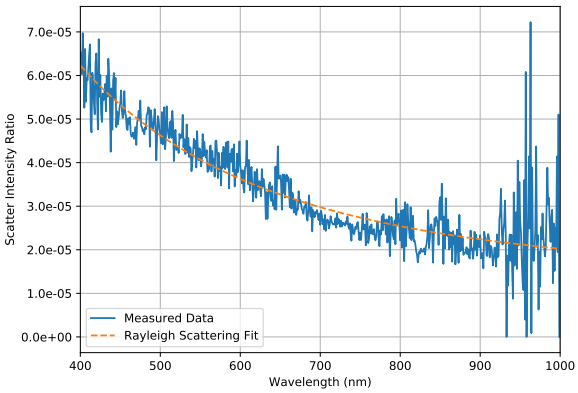

Figure 5.3: The intensity found for each wavelength at θ = 14° from the HS measurement of plain Optiwhite. The values are divided by the zero-angle intensity and are shown as the blue solid line. The orange dotted line is the fit using the function $y = a/(\lambda - c)^4 + b$.

From this, a reasonable fit was found, indicating that the wavelength-dependent scattering is indeed Rayleigh scattering due to impurities. While the scattering intensity follows a near $1/\lambda^4$ dependence, this is not visible in the HS values, which seem to have a near-linear dependence.

Surface scattering

Another possibility for the measured scattering of the plain Optiwhite sample is scattering due to surface roughness. Glass surfaces are known to have a certain degree of surface roughness, which can cause light scattering. Root Mean Square (RMS) roughness is a statistical measure of the surface texture of a material, quantifying the vertical deviations of the surface from the mean plane. Typical commercial glass has an RMS roughness of about 1.2 nm, again being in the Rayleigh scattering regime [44]. Therefore, similar conclusions can be drawn when considering impurity scattering.

In reality, the measured HS is likely due to both impurity scattering and surface scattering effects. To gain more insight into the origin of the scattering, highly polished glass with an RMS roughness of 0.1 to 0.2 nm due to super-polishing could be obtained. For such glass, scattering effects are minimized to the extent that the wavelength dependency is significantly reduced [45].

HS measurement setup discrepancies

While not yet discussed, a possibility also remains that the HS values measured do not correctly represent reality due to unexpected experimental phenomena. From section 5.1 it was mentioned that issues such as a low signal-to-noise ratio may cause slight variations in the results.

However, from looking at the directly measured angle dependent intensity, it is hard to argue that low HS values could be expected due to the simplicity of the setup and the fact that the amount of intensity measured corresponds well with the found HS values where more counts were present in areas with high HS values. As the above argument aligned well when comparing all measured coating, the possibility of measurement setup discrepancies will not be repeated in further sections, as the argument remains the same.

To exclude this possibility, it is advised to improve the setup by eliminating the found issues as discussed in section 5.1. Afterwards, the HS value of coatings with a known HS value could be measured.

5.2.2. Hemispherical Light Transmission

From the HLT results discussed in section 4.2.1, it was found that simulations gave 2.24% less HLT than measurements. Since WUR also measured the HLT of Optiwhite with their setup, yielding similar results to our in-house measurements, there is a strong indication that the simulation underestimates the actual transmission. To investigate whether incorrect simulation input parameters could explain the difference, these parameters will be systematically varied, starting with the refractive index (n) and extinction coefficient (k) of Optiwhite, followed by the thickness of Optiwhite glass. Finally, the possible effect of surface scattering on the difference will be discussed.

Varying n & k of Optiwhite

To explore the effects of slightly varying n & k in the simulation, a scale factor was introduced, where n or k were separately multiplied by a single scale factor across the whole wavelength spectrum. The results from the simulation are shown in Figure 5.4 below.

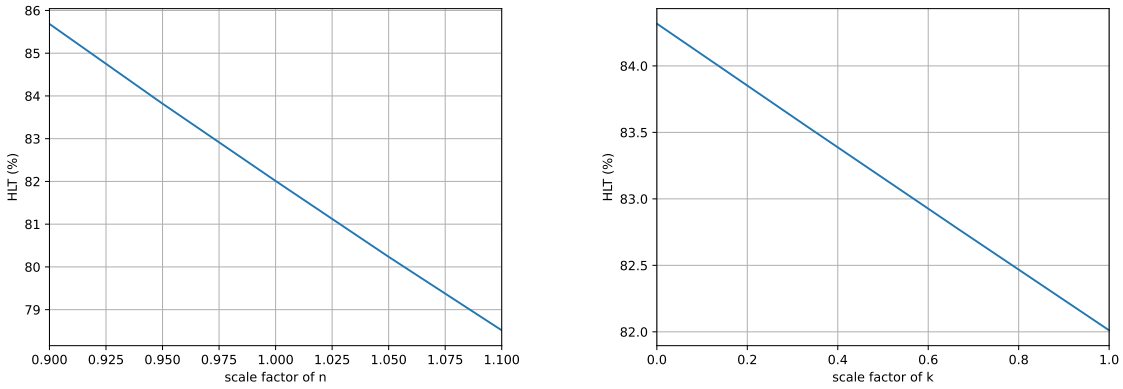

(a) n **(b)** k

Figure 5.4: Simulations of HLT for Optiwhite glass. In (a), the refractive index n is scaled by a single value across the wavelength-dependent spectrum, and in (b), the extinction coefficient k is scaled by a single value. For these simulations, $5 \cdot 10^5$ photons were used.

Scaling both n and k causes changes in the HLT in a linear manner. As the simulations gave an HLT of about 82% and the measurements about 84%, it can be seen that solely changing n or k can result in an HLT value of 84%. However, in the case of k, the value would need to be a factor of 10 smaller. While this is only a scaling of the whole spectrum, in reality, wavelength-dependent shifts are also possible, which may yield more complex results. From scaling the complex refractive index, the possibility of discrepancies in these values could explain the 2% mismatch in HLT between measurements and simulations.

Towards the end of the project, the n & k values of the actual glass samples used in the experiments were received from the manufacturer NSG [46]. Unfortunately, there was no more time to apply this to all simulations. However, from doing HLT simulations of Optiwhite with the new complex refractive index, an HLT value of 83.00% was found. Compared to the old simulation value of 82.09%, the value is indeed closer to the measured value of 84.4%. Unfortunately, this does not completely resolve the mismatch between measurement and simulation, possibly indicating that this value still slightly differs from the true value.

The values from NSG are compared to the values from Treharne used for all simulations in Figure 5.5 below. It can be seen that in the relevant wavelength spectrum of 400 nm to 700 nm used to calculate HLT, the n values are larger while the k values are lower. This difference indicates that two measurements on different glass plates produced by the same manufacturer give different values of n & k. As indicated by NSG, values of k are known to fluctuate during the production process. This, however, does not explain the difference of about 0.01 measured in n.

To gain more insight, an attempt was made to measure the refractive index of Optiwhite using a Woollam M-2000 ellipsometer. However, the results gave no extinction coefficient and an even larger refractive index, yielding less accurate results. It is known in ellipsometry that proper alignment and calibration of the ellipsometer are crucial for accurate measurements. Misalignment can introduce errors in the polarization state of the light, leading to discrepancies [47]. While it is hard to estimate the exact uncertainties, this may indicate that measuring the complex refractive index has a limit on its accuracy, which may prove to be a constraint on producing accurate simulations.

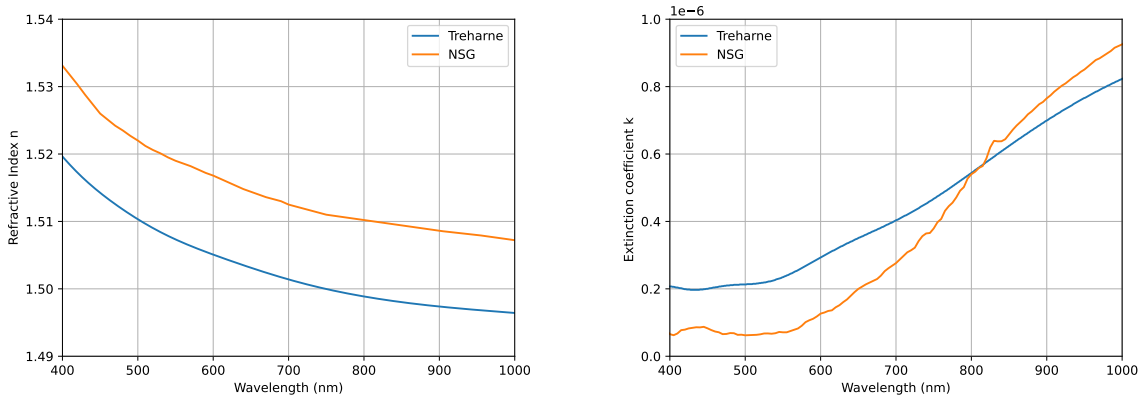

(a) n **(b)** k

Figure 5.5: The refractive index values (a) and the extinction coefficient values (b) for wavelengths between 400-700 nm, taken from Treharne [25] and received from NSG [46].

Thickness of Optiwhite

Another simulation variable is the glass thickness. While this is well-defined as it is easily measured, the effects of small changes were explored. It was found that decreasing the glass thickness from 4 mm to 3.5 mm resulted in a change of HLT value of -0.16%. This rules out small variations in glass thickness causing the current mismatch.

Scattering

Altering the simulation input parameters as discussed above shows the possibility of explaining the found mismatch between measurement and simulation. However, another possibility is due to the assumptions made in the simulation. While scattering is not implemented in the simulation, there was a strong indication from HS measurements that Rayleigh scattering plays a significant role. Therefore, it is important to consider the mismatch between measurement and simulation of the HLT value due to scattering. However, from Figure 4.8, it can be seen that the transmittance at θ = 0° is lower for the simulation than for the measurement. For the perpendicular situation, isotropic Rayleigh scattering is expected to only decrease the transmission due to effects such as total internal reflection (TIR). Therefore, it is hard to argue that the found scattering is the dominant cause of the difference in HLT values.

HLT measurement setup discrepancies

Finally, a reason for the mismatch between measurement and simulation may also be due to imperfections in the experimental setup. While not the focus of this thesis, changing the system parameters of the HLT setup as described in section 3.2.3 may provide more insight into potential setup flaws. Examples include misalignment of the rotation point, misalignment of the sample where a gap is present between the sample and the sphere, or even changing the port size and thickness.

5.2.3. Angle dependent transmission

Until now, only the single HLT value has been discussed, which is a weighted average of the angular transmission as shown in equation 2.20. However, by examining the angular dependence of the transmission, a more detailed comparison between measurement and simulation can be made, potentially providing more insight into the origin of the discrepancies.

As mentioned in the results, the simulation underestimated the transmission at each angle θ, with the largest difference observed at θ = 60°. This is visible in Figure 4.8 from the results. It was also found that scaling the input parameters of Optiwhite could improve the overlap between measurement and simulation, but the effects on the shape of the angle-dependent transmission curve were not considered. Therefore, the refractive index of Optiwhite will be scaled, and the effects on the angular transmittance will be discussed.

Scaling n of Optiwhite

From Figure 5.4a, it can be seen that scaling the refractive index of Optiwhite by around 0.93 gives an HLT of just above 84%, better matching the value found from the measurement. The corresponding angle-dependent transmittance is shown in Figure 5.6 below.

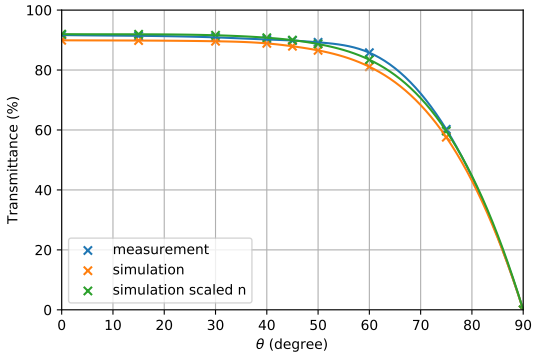

Figure 5.6: Angle-dependent transmission of plain Optiwhite for the measurement, simulation, and simulation where n of Optiwhite was scaled by a factor of 0.93. Here, $1 \cdot 10^6$ photons were used for the simulation.

While the two curves of measurement and simulation now lie closer together, the general shape remains slightly different. The biggest difference is again observed at θ = 60°, where the simulation underestimates the transmission. To achieve a similar HLT value, the simulation therefore overestimates at lower angles. This suggests that only scaling the refractive index of Optiwhite may improve the match of HLT but does not resolve the slight discrepancies between measurement and simulation.

Linear scaling of n of Optiwhite

Since the refractive index was only scaled by a single constant across the whole wavelength-dependent spectrum, it may be possible that the scaling needs to be more complex. For example, multiplying the wavelength-dependent refractive index by a linear function.

To determine if scaling n of Optiwhite by a linear function can explain the difference in angle-dependent transmission, a theoretical refractive index distribution was created based on the scaled refractive index with a factor of 0.93, which gives an HLT value close to the measurement. The theoretical n distribution is the scaled distribution multiplied by a linear function with a similar average value. The result is shown in Figure 5.7a.

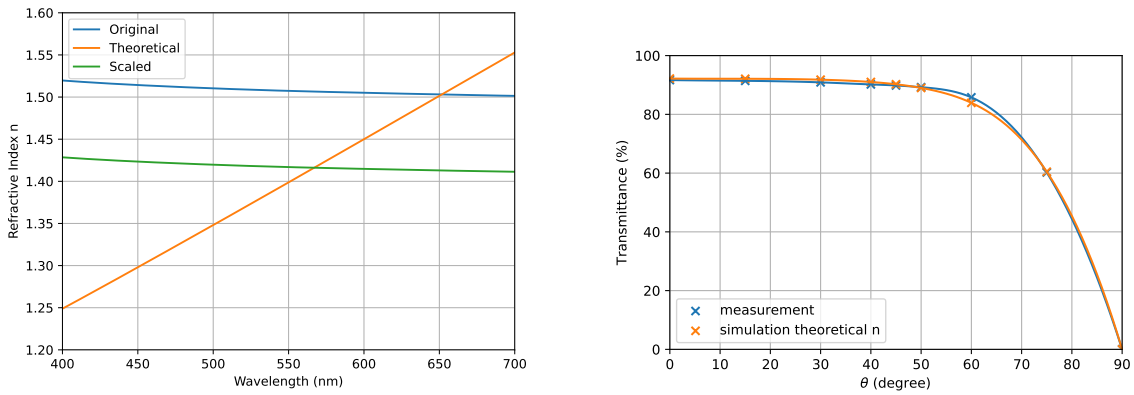

Figure 5.7: In (a), the refractive index of Optiwhite is shown as taken from [25], scaled by 0.93 and a theoretically made refractive index. In (b), the angle-dependent transmission is shown for the measurement and the simulation of plain Optiwhtie using the theoretical refractive index.

Using this theoretical n as an input for the simulation, the HLT was found to be 84.53%, remarkably close to the measured value of 84.48%. When looking at the angle-dependent transmittance corresponding to this simulation, shown in Figure 5.7b, a very similar curve is seen compared to the simulation using the original refractive index, with the same underestimation at θ = 60°. This strongly indicates that this artefact is not due to the incorrect input of the refractive index in the simulation.

Scaling of k of Optiwhite

As mentioned above, scaling the extinction coefficient (k) of Optiwhite could also result in a better match of the HLT value. To explore if this could affect the shape of the angle-dependent transmission curve, k was scaled by a factor of 0.1. The result is shown below in Figure 5.8.

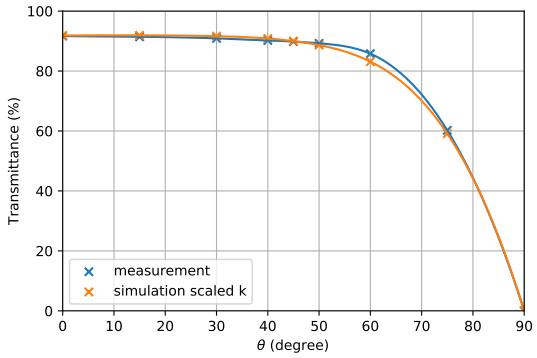

Figure 5.8: Angle-dependent transmission of plain Optiwhite for a simulation where k of Optiwhite was scaled by a factor of 0.1. Here, $1 \cdot 10^6$ photons were used for the simulation.

A very similar result is seen from scaling n of Optiwhite. Scaling k again does not explain the difference in curve shape between measurement and simulation. The simulation again underestimates the transmission at θ = 60°.

To check if a more complex scaling could change the shape of the curve, simulations using k measured by Treharne (used in all simulations) and k measured by NSG were compared, as they have different wavelength dependencies. These were both shown in Figure 5.5. After comparing these, it was seen that this had little effect on the angle-dependent transmission curve shape, thus again not being able to explain the increased mismatch at θ = 60° between simulation and measurement.

It seems that scaling n & k of Optiwhite cannot result in a match in curve shape between measurement and simulation, indicating that the discrepancy has a different origin.

Rayleigh scattering

As altering the simulation input parameters was thus far unsuccessful in describing the difference at θ = 60°, the origin may be due to limitations in the theory used in the simulations. As for the simulations thus far, no scattering can take place, which is also a possible explanation for the found differences. As significant scattering was found from HS measurement, it could potentially increase the transmittance at this angle of incidence. To further explore this, Rayleigh scattering could be implemented in the simulation to discover if this can explain the relative increase seen at θ = 60° from the measurements. Another option could be to measure glass with different scatter impurity contents to gain insight into the possibility of this being the cause of the found differences.

HLT measurement setup discrepancies

Finally, as mentioned before, the possibility also exists that imperfections in the HLT measurement setup itself are the cause of the described phenomena. Therefore, the same recommendations hold as given in section 4.2.1.

5.3. Coating without silica

In this section, the coatings without silica for all four thicknesses (t_{wet}) will be discussed. The discussion is divided into three main sections: First, the Hortiscatter (HS) results and potential reasons for the wavelength dependence of HS will be explored. Next, the comparison between the single-valued Hemispherical Light Transmission (HLT) from measurements and simulations will be addressed. Finally, the angle-dependent transmission will be analyzed in detail, focusing on small discrepancies in angle dependence.

5.3.1. Hortiscatter

Examining the HS results of the coatings without silica particles, it is evident from Figure 4.3 that the simulations yield results similar to those for plain Optiwhite, as shown in Figure 5.2.1. This outcome is expected because the simulations currently do not incorporate any type of scattering. Consequently, no thickness dependence was simulated.

However, the measurement results in Figure 4.3 reveal a wavelength-independent HS of around 10%. No significant thickness dependence was found in the measurements, except for t_{wet} = 200 µm. As mentioned in the results, this particular coating exhibited visible inconsistencies, which will be discussed in more detail later in this section. For now, the t_{wet} = 200 µm coating will not be considered.

Comparing the HS measurements of plain Optiwhite and the polymer coating without silica for t_{wet} = 150 µm, a similar HS is observed for the shortest wavelengths, remaining fairly constant for the polymer coating over all wavelengths. This is illustrated in Figure 5.9, where both are plotted together.

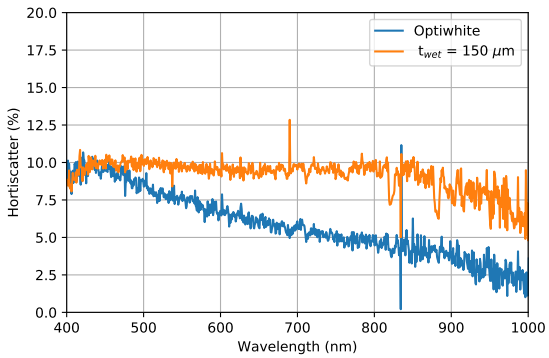

Figure 5.9: Measured HS values of plain Optiwhite glass and the polymer without silica for a wet thickness of t_{wet} = 150 µm.

The decrease in HS from 900 to 1000 nm for the polymer coating without silica is assumed to be due to the spectrometer receiving too few counts, leading to an increased signal-to-noise ratio. To confirm this, measurements with a higher source intensity in this regime can be conducted.

While the HS dependence of the polymer coatings differs from that of plain Optiwhite, a similar origin is suggested since both impurity scattering and surface scattering are not simulated. These factors will be discussed individually.

Impurity scattering

The non-wavelength dependence of scattering suggests the presence of impurities much larger than or close to the wavelength of light, indicating Mie-theory or geometric scattering, where wavelength dependence is minimal [48]. Possible examples include small air bubbles incorporated during the mixing process. However, it is expected that an increase in coating thickness would correspond to an increase in impurity content, which is not reflected in the measurements. To rule out these effects, transmission electron microscope images could be taken to identify large impurities, though this was not possible within the scope of this thesis due to time constraints.

Surface scattering

Another potential cause for the wavelength-independent HS is surface roughness. Profilometer measurements, shown in Figure 3.20a, indicate micron-scale surface roughness, which could lead to wavelength-independent scattering. To gain further insight, experimenting with different coating application methods that result in varying surface roughness types would be beneficial.

Coating inconsistencies

As mentioned in section 4.1.4, the polymer coating without silica for t_{wet} = 200 µm exhibited visibly more surface roughness on the mm^2 scale compared to the other coatings. To explore the possible effect, the HS measurement was repeated at another location, yielding different values, as shown in Figure 5.10.

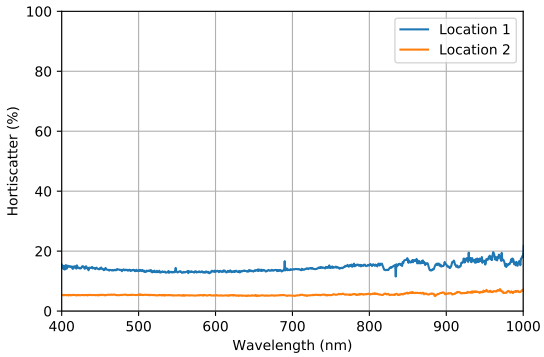

Figure 5.10: HS measurement of the coating without silica for t_{wet} = 200 µm at two different locations.

Non-homogeneous coatings can exhibit significant differences in HS values when measured at different locations. As discussed in section 4.1.1, when the coating inconsistency is larger than the acceptance area of the detector, HS measurements can be highly location-dependent. Ideally, multiple measurements at different locations would need to be averaged, but due to time constraints, this was not feasible.

5.3.2. Hemispherical Light Transmission

From the HLT results discussed in section 4.2.2, simulations consistently showed an HLT of 83.13% for each coating thickness (t_{wet}), with a 0.01% difference within the uncertainty range of simulation reproducibility.

In the measurement results shown in Table 4.1, little thickness dependence was observed. The three thinner coatings had an average HLT of 84.36%, while the thickest coating (t_{wet} = 200 µm) had a slightly higher HLT of about 84.49%. This minor difference is likely due to the visual inconsistencies discussed in section 5.3.1. The potential effects of these inconsistencies will be detailed later in this section.

Overall, a difference of about 1.23% was found between the simulations and measurements, with the simulations underestimating the HLT. This is similar to the 2.24% difference observed for plain Optiwhite, as discussed in section 5.2.2, but now the difference has decreased. To investigate whether incorrect simulation input parameters could explain the difference, these parameters will be systematically varied. First n of Optiwhite will be scaled, then n of the polymer will be varied and finally k will be added to the polymer for different values.

Scaling n of Optiwhite

To assess the impact of slightly varying n of Optiwhite on simulated HLT values, the wavelength-dependent n was scaled by a single factor in the same way as demonstrated in section 5.2.3. The results are shown in Figure 5.11.

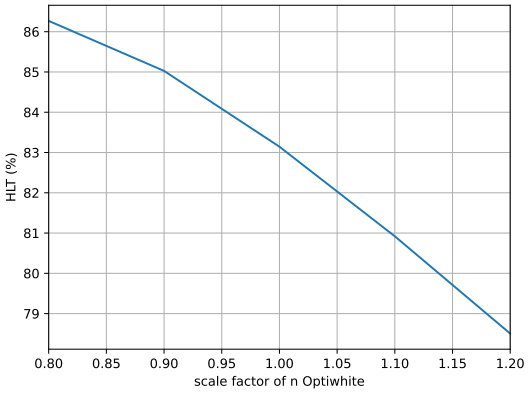

Figure 5.11: Simulations of HLT for the polymer coating without silica particles. n of Optiwhite is scaled by multiplying the entire wavelength-dependent spectrum by a single scale factor. t_{dry} was set to 20 µm, and $1 \cdot 10^6$ photons were used. Five scale factors were simulated, equally spaced between 0.8 and 1.2.

Scaling n of Optiwhite by 0.93 results in an HLT of around 84.4%, closely matching the average value of 84.36% found for the measurements of the first three thicknesses. This same scale factor also provided a good match for plain Optiwhite, strongly indicating that this adjustment might explain the observed differences in HLT between simulation and measurement.

It was also found that similar to what was seen for plain Optiwhite in section 5.2.3, scaling the extinction coefficient (k) had minimal effect on HLT values and behaved linearly. Due to this minimal effect, a detailed analysis of k scaling was not pursued.

Scaling n of the polymer

Introducing the polymer coating into the simulation adds a new variable: its refractive index. For the simulations, a wavelength-independent value of n = 1.4052 was used. Due to the relatively large surface roughness of the coating, measuring this value with an ellipsometer was not feasible, and the refractive index value was provided by Fotoniq. However, the origin of this number is unclear. As no wavelength dependence was used and the composition of the polymer differed slightly from the recipe used by Fotoniq as mentioned in section 3.4, the refractive index of the polymer may vary from the true value.

To explore the effect of changes in the polymer's refractive index, simulations were performed with varying n values, as shown in Figure 5.12.

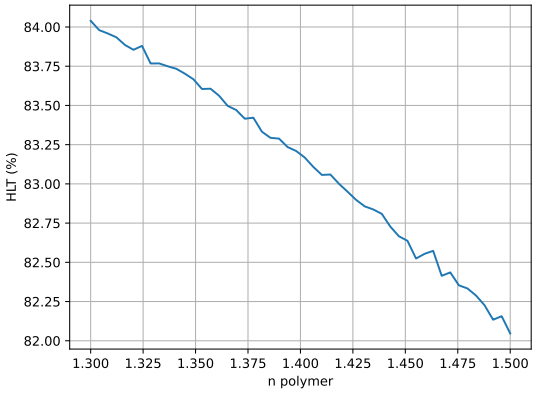

Figure 5.12: Simulations of HLT for the polymer coating without silica particles. The wavelength-independent n of the polymer is simulated between 1.3 and 1.5 in 50 equally spaced steps. t_{dry} was set to 20 µm, and $5 \cdot 10^5$ photons were used.

Apart from the slight variations due to the relatively small amount of photons used for the simulation, a linear dependence is seen between n of the polymer and the HLT. A polymer with a refractive index of n = 1.3 could cause the simulations to yield HLT values similar to the measurements. However, since the refractive index for many common optical-grade polymers falls within the range of 1.4 to 1.6 [49], it is unlikely that the n value for the polymer is dominant in causing the mismatch between simulation and experiment.

If a discrepancy in the polymer's refractive index plays a role, it is more likely to be minimal. To improve simulation accuracy, future measurements of the polymer's refractive index with wavelength dependence should be conducted using an Abbe refractometer with multiple monochromatic light sources. A smooth surface is necessary for these measurements.

Varying k of the polymer

To investigate whether the absence of an extinction coefficient significantly affects simulated HLT values, simulations were performed by adding a constant k value to the polymer across all wavelengths. Note that the original simulation did not make use of an extinction coefficient (k) for the polymer. This was done for t_{wet} = 50 µm and t_{wet} = 200 µm, with results shown in Figure 5.13. The k values varied between 0 and $1 \cdot 10^{-5}$, as highly transparent polymers typically have extinction coefficients in the range of $1 \cdot 10^{-5}$ - $1 \cdot 10^{-7}$ [50].

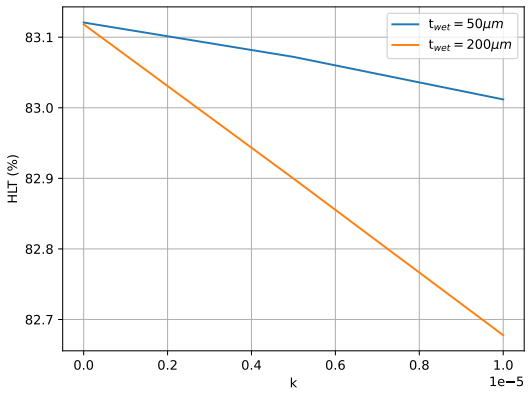

Figure 5.13: Simulated HLT values by introducing an extinction coefficient to the polymer and varying it between 0 and $1 \cdot 10^{-5}$. This was done for two thicknesses: t_{wet} = 50 µm and t_{wet} = 200 µm, corresponding to dry thicknesses of t_{dry} = 5 µm and t_{dry} = 20 µm. $5 \cdot 10^5$ photons were used.

The results show that adding k to the simulation has minimal effects on the final HLT value. Furthermore, an increase in coating thickness would be expected to decrease HLT, but this effect was not significant in the measurements. For this reason, it can be concluded that not including k of the polymer in the simulations will not create significant variations.

Surface scattering

As discussed for plain Optiwhite, the mismatch found might be due to simulation limitations where scattering is not accounted for. The HS results in Figure 4.3a indicate a significant wavelength-independent HS of around 10%. However, similar to plain Optiwhite, the simulated HLT values expect near zero values. While seeming counterintuitive, under certain conditions large-scale surface roughness can actually increase hemispherical transmission [51]. To rule out this effect, it would be interesting to alter the surface roughness on different scales.

HLT measurement setup discrepancies

Similar to before, the mismatch might also stem from unexpected phenomena arising from the experimental setup. Therefore, the discussion on the possibilities of experimental phenomena being the cause of the observed differences remains the same as in section 5.2.3. As this argument can be made for each non-trivial effect discovered, the possibility of the HLT measurement setup causing discrepancies will not always be repeated.

Coating inconsistencies

For the coating with t_{wet} = 200 µm, a slightly higher HLT value of around 0.1% was found compared to other thicknesses. This coating appeared to have more surface roughness on the mm^2 scale, suggesting that large-scale surface roughness might increase HLT. However, it is crucial to explore the location dependence of HLT measurements, as surface roughness on the mm^2 scale may be sensitive to the exact location of the integrating sphere's edge. Due to time constraints, this was not possible, but to determine the potential effect of surface roughness on HLT, multiple measurements should be taken at varying locations to rule out this dependence.

5.3.3. Angle dependent transmission

Thus far, only the single HLT value has been discussed. However, examining the angular dependence of the transmission allows for a more detailed comparison between measurement and simulation. Figure 4.10 shows that the simulation underestimates the transmission at each angle θ, with the largest difference observed at θ = 60°, similar to what was seen for plain Optiwhite in section 5.2.3 where scaling n of Optiwhite improved the HLT match but did not resolve this phenomenon.

To determine if this holds true when a coating is added, the angle-dependent transmittance was simulated, scaling the refractive index of Optiwhite by 0.93 to match the HLT between measurement and simulation. The results are shown in Figure 5.14.

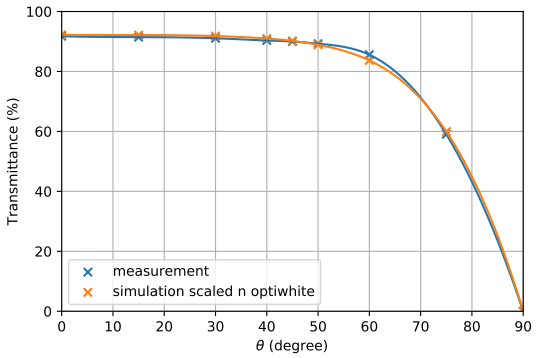

Figure 5.14: Angle-dependent transmission of the polymer coating without silica for t_{wet} = 150 µm. Both the measurement and simulation where n of Optiwhite was scaled by a factor of 0.93 are shown. Here, $1 \cdot 10^7$ photons were used for the simulation.

The same conclusion as for plain Optiwhite can be drawn, where the difference observed at θ = 60° remains. Due to the similarity of the situation compared to plain Optiwhite, and given that other simulation parameters are not expected to have a dominant effect on the difference between measurement and simulation, further discussion on varying these parameters for angle-dependent transmission is omitted.

Surface scattering

As mentioned in section 5.3.2, large-scale surface scattering may increase the HLT. However, it is expected to have angle dependence rather than increasing transmittance equally at all angles [51]. While difficult to compare due to the possible influence of other parameters, the transmission curve of the simulation and measurement with coating seem to differ similarly as seen for plain Optiwhtie. This possibly indicates that the effect of surface scattering increasing the HLT does not play a significant role.

5.4. Coating with d = 160 nm

This section will discuss the results and analysis of the coatings with silica particles of diameter d = 160 nm. The discussion is divided into three main parts. First, the Hortiscatter (HS) results will be examined because the measurements showed significantly higher HS values than simulations and

minimal exponential decay, suggesting potential issues with silica concentration and refractive index variations. Next, the single-valued Hemispherical Light Transmission (HLT) will be compared between measurement and simulation due to observed thickness-dependent discrepancies, indicating the need to explore variations in coating thickness and refractive index. Finally, the angle-dependent transmission will be analyzed in detail as the measurements indicated higher scattering at certain angles, which requires understanding the impact of increased scattering and potential experimental setup imperfections.

5.4.1. Hortiscatter

From the HS results of the coatings with silica particles of diameter d = 160 nm shown in Figure 4.4a, it was found that simulations predicted an exponential dependence of HS, which decreased with longer wavelengths. However, the measurement results indicated minimal exponential decay, with HS values significantly larger than those simulated.

To explore if the different slopes of the exponential wavelength dependence of HS between measurements and simulations could be explained through simulation, variations in some input parameters were tested. Since the parameters significantly influencing scattering are the silica refractive index, silica concentration, and coating thickness, other parameters were not discussed. While the refractive index of the polymer might also influence scattering, it was found later that n of the polymer and silica are directly related, as discussed in the Hemispherical Light Transmission section of this part.

Varying coating thickness

The effect of varying coating thickness on HS values is shown in Figure 4.4a. An increase in HS for thicker coatings follows expectations as more silica particles are present to scatter from. However, the slope of the exponential decay remains unchanged, indicating that coating thickness does not explain the difference in slope between measurement and simulation.

Scaling n silica and varying silica concentration

To investigate the effect of varying n of silica, the wavelength-dependent spectrum was scaled by factors of 1.01 and 1.1. Additionally, a simulation with a silica concentration of 30 wt% was conducted. The results, along with the original simulation for $t_{wet} = 200$ µm, are shown in Figure 5.15.

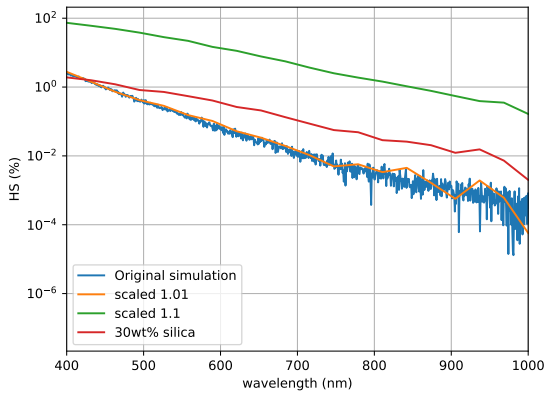

Figure 5.15: HS simulation of the coating with $t_{wet} = 200$ µm, corresponding to $t_{dry} = 35.4$ µm. The original simulation is shown, as well as two simulations where n of silica is scaled by different factors and a simulation where the concentration of silica is increased to 30 wt%. For the non-original simulations, 20 wavelengths evenly spread out between 400 and 1000 nm were simulated.

From this, it can be seen that the HS values increase with increasing n of silica, as expected from Mie theory, which suggests that increasing the difference in refractive index with the surrounding medium generally increases scattering probabilities [14]. An increase in HS values is also observed with higher silica concentration, again as expected with more scatter particles present. While indeed an increase

in simulated HS is observed, the slope of the exponential decay becomes less steep. Comparing this to the steepness from the measurements shown in Figure 4.4b, a significant difference remains.

Varying the relevant simulation input parameters thus suggests that simulations cannot explain the wavelength-dependent HS values from measurements. This discrepancy might be due to incorrect assumptions in the simulations. Potential effects not simulated that may cause increased scattering include impurity scattering, surface scattering, and inhomogeneous coatings due to particle agglomeration. These will be discussed independently.

Impurity scattering

Section 5.3.1 on coatings without silica concluded that impurity scattering is unlikely to play a significant role as no significant differences were found in HS for different coating thicknesses. However, incorporating silica into the coatings might introduce impurities such as small air bubbles. Since the only change was adding a silica solution instead of water, this is unlikely. To confirm, microscopic images of the coating could be taken.

Surface scattering

While impurity scattering is not expected to play a significant role, surface roughness is likely to increase the measured HS values, as discussed in section 5.3.1. Since surface roughness is not included in the simulations and the measured HS was much larger than simulated, this strongly indicates the impact of surface roughness.

Assuming the measured HS for a coating without silica is due to surface roughness, it would be interesting to explore subtracting these values from the HS measured for coatings with silica. This idea is based on removing the surface roughness effect from the measured HS values. Figure 5.16 below shows the HS of the coating without silica subtracted from the coating with silica along with the original measurement and simulation. All coatings are for $t_{wet} = 100$ µm.

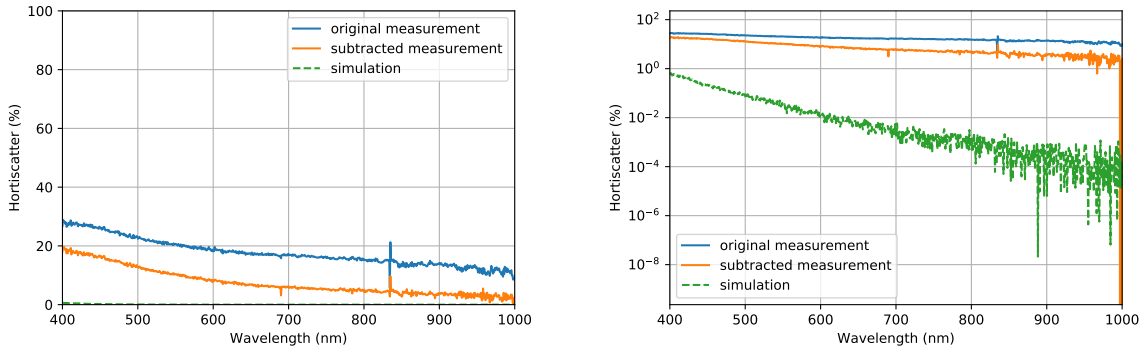

Figure 5.16: The measured HS of the coating containing silica with d = 160 nm, as well as this measurement subtracted by HS measured for the coating without silica. The original simulation of HS for the coating with silica is also shown. For all coatings, $t_{wet} = 100$ µm, and the figures are shown in a normal scale (a) and a log scale (b).

From Figure 5.16b, subtracting the HS value measured for the coating without silica slightly increases the exponential decay, but it does not achieve the same steepness as the simulation.

Thus, simply subtracting the HS for a coating without polymer, assumed to be due to surface roughness, from the measured HS with both particle scattering and surface roughness does not align with measurement and simulation. It could be that the method of calculating HS might not allow for this correction by simple subtraction after processing the data. Comparing the angle-dependent intensity distributions might provide more insight, but this is beyond the scope of this thesis.

Another potential reason for the mismatch is that surface scattering and particle scattering might interact in a complex way, making it impossible to simply add their individual effects.

Particle agglomeration

The simulations assumed that the particle diameter is 160 nm and that the particles are homogeneously dispersed throughout the coating. However, as mentioned in section 4.1.5, visible particle agglomeration was observed. HS measurements avoided visible inconsistencies by placing the detector acceptance area on a visually homogeneous part of the coating. However, non-visible particle agglomeration could still be the cause of the increase in measured HS values. HS measurements showed similar results when avoiding visible inconsistencies, indicating that, if present, any non-visible particle agglomeration is homogeneously spread throughout the coating.

To explore the potential effect of particle agglomeration in simulations, these particle 'clumps' might be approximated by larger single particles. From Mie theory, larger particles generally show less wavelength dependence. A simulation with a particle size of $d = 1$ µm was conducted, as this size is expected to show more scattering but remain invisible to the naked eye. The results are shown in Figure 5.17.

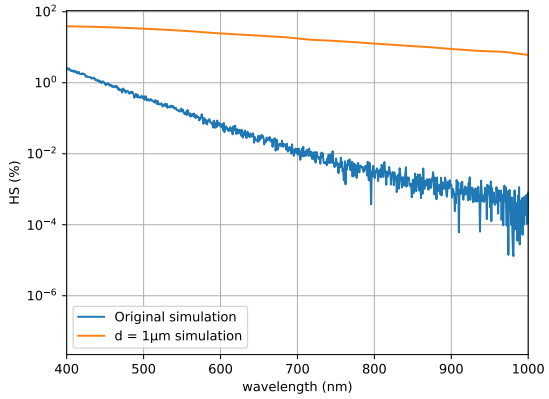

Figure 5.17: HS simulation of the coating with $t_{dry} = 35.4$ µm. The original simulation is shown, as well as a simulation where the silica particle size was set to $d = 1$ µm. For the latter, 20 wavelengths evenly spread out between 400 and 1000 nm were simulated.

The results show similar HS values to those measured, as seen in Figure 4.4b. While the simulation assumes spherical particles, which might not be true for particle agglomeration, it indicates the possibility of this explanation.

Although beyond the scope of this thesis, microscopic photographs of the coating could provide more insight into the possibility of non-visible particle agglomeration. However, the glass including coating is too thick for most electron microscopes. Therefore, a new coating mixture that can be dried without applying it to a glass substrate would be needed for TEM pictures to determine if particle agglomeration is present on a scale not visible to the naked eye.

The origin of particle agglomeration is still unknown. It may result from the evaporation process where heating disturbed the solution. Other research has found that smaller silica particles are more prone to agglomeration [52]. Future work could involve centrifuging the solution for an extended period and using a pipette to extract the desired amount of water from the top of the separated solution.

5.4.2. Hemispherical Light Transmission

From the HLT results in section 4.2.3, a generally good overlap between measurements and simulations was found, with HLT values differing by less than 1% for all thicknesses. However, a thickness dependence on the mismatch between measurement and simulation was observed.

The two simulation input parameters expected to show thickness dependence are the estimated dry thickness and the silica concentration. These will be explored individually, followed by varying the refractive indexes of Optiwhite, the polymer, and silica to examine their effects on the overlap between

measurement and simulation of HLT. As silica has a zero k and varying k of Optiwhite and the polymer had little effect in sections 5.2.2 and 5.3.2, these will not be discussed further.

Dry coating thickness

Starting with the coating thickness, there was an indication that the estimated dry coating thickness used for the simulation does not match the actual dry coating thickness, based on the thickness dependence of the mismatch seen in Table 4.2. To visualize this better, the table is plotted against the corresponding dry thickness in Figure 5.18.

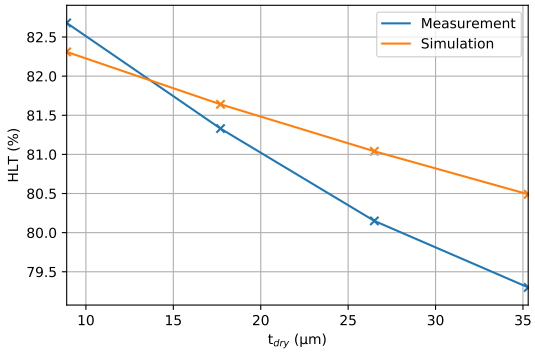

Figure 5.18: Measurements and simulations of the HLT at four different thicknesses t_{dry} for the coatings containing silica particles with d = 160 nm. The data are taken directly from Table 4.2.

The measured HLT values show an almost linear dependence. It is unclear if the slight deviations from the linear trend are due to coating production or measurement inconsistencies. More data points are needed to rule this out. The simulation data show a clear linear dependence of HLT values on t_{dry}.

Comparing the measurement and simulation data reveals that the measurements show a steeper decay with thickness. This suggests that the estimated dry thickness might be inaccurate and that the actual dry thicknesses of the coatings are further apart than estimated. As explained in section 3.4, inaccurate t_{dry} estimations are not unexpected since they are based on a profilometer measurement of a single coating without silica. Profilometer measurements were unfortunately difficult to realize for this project. However, to exclude large uncertainties in coating thickness, it should be measured for each coating instead of predicted based on one measurement. Another possibility is using White light interferometry measurements.

Silica concentration

While different dry thickness estimations might explain the thickness dependence of HLT shown in Figure 5.18, another possibility is that the silica concentration in the coatings differs from expectations. To explore this, the silica weight percentage was doubled in the simulations to see its effect on thickness dependence. This is shown in Figure 5.19.

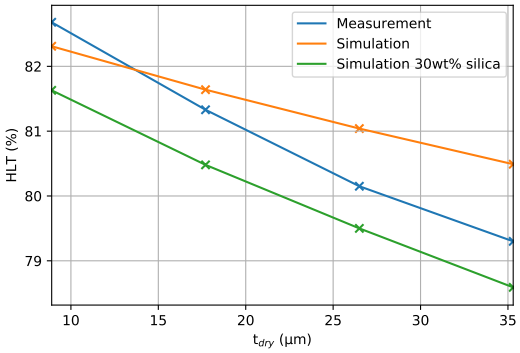

Figure 5.19: Measurements and simulations of the HLT at four different thicknesses T_{dry} for the coatings containing silica particles with d = 160 nm. Apart from the original simulation, a simulation with double the silica content (30 wt%) is shown.

The results show that while the values are slightly lower, a similar thickness dependence in HLT is seen in simulations. However, a concentration of 30 wt% silica is unrealistic. During the coating production process, explained in section 3.4, a scale with an error of 0.0001 g was used, leaving little room for uncertainty. Variations in the exact weighed amounts resulted in fluctuations in the final silica weight percentage of no more than 0.22%. Other potential causes for differences in silica concentration could be inhomogeneity of the silica solution when extracting the desired amount or inhomogeneity in the produced coating mixture before application. While varying silica concentration affects thickness dependence, it is unlikely to be the sole cause of the mismatch.

Varying n of Optiwhite, the polymer, and silica

Although the simulation generally shows good overlap with HLT measurements, previous sections 5.2.2 and 5.3.2 indicated that scaling n of Optiwhite improved the match between measurements and simulations. Therefore, it is interesting to explore the effects of varying relevant simulation input parameters to understand their impact on the overlap. The refractive indexes of Optiwhite, the polymer, and silica were varied, as shown in Figure 5.20.

Figure 5.20a shows a linear dependence in HLT when scaling n of Optiwhite, similar to the case of plain Optiwhite and coatings without silica shown in Figures 5.4a and 5.11, respectively.

In Figure 5.20b, varying n of the polymer reveals a non-linear relationship with a clear optimum. This differs significantly from the coating without silica shown in Figure 5.12, where a linear relationship was found. This can be explained by also looking at Figure 5.20c, where n of silica is scaled for different values. The two are mirror images and seem correlated. This correlation can be explained by the fact that increasing the difference in refractive index with the surrounding generally increases Mie scattering probabilities. When n of the polymer and silica are closest, HLT will be the largest as less scattering occurs. This indicates that the simulations expect a decrease in HLT for increased scattering.

Scaling n of Optiwhite by a factor of 0.93 in the case of plain Optiwhite and coatings without silica provided better simulation HLT results. However, applying this scale factor here increases the HLT value by more than 1%, as seen in Figure 5.20b. Since simulations and measurements already showed reasonable overlap, this would decrease the match.

While solely scaling n of Optiwhite decreases the overlap, a combination of varying multiple simulation parameters might maintain consistent simulated HLT values. Section 5.3.2 suggested minimal variations in n of the polymer. However, Figure 5.20c shows that minimal variations can significantly affect results. Therefore slightly varying n of the polymer together with n of Optiwhite might still prove to show good overlap between measurement and simulations.

Figure 5.20c indicates that HLT values are even more sensitive to small variations in the refractive index of silica. As discussed in section 3.3, the refractive index of silica was decreased from that of amorphous silica using the Lorentz-Lorentz relationship. Assumptions made include that silica is

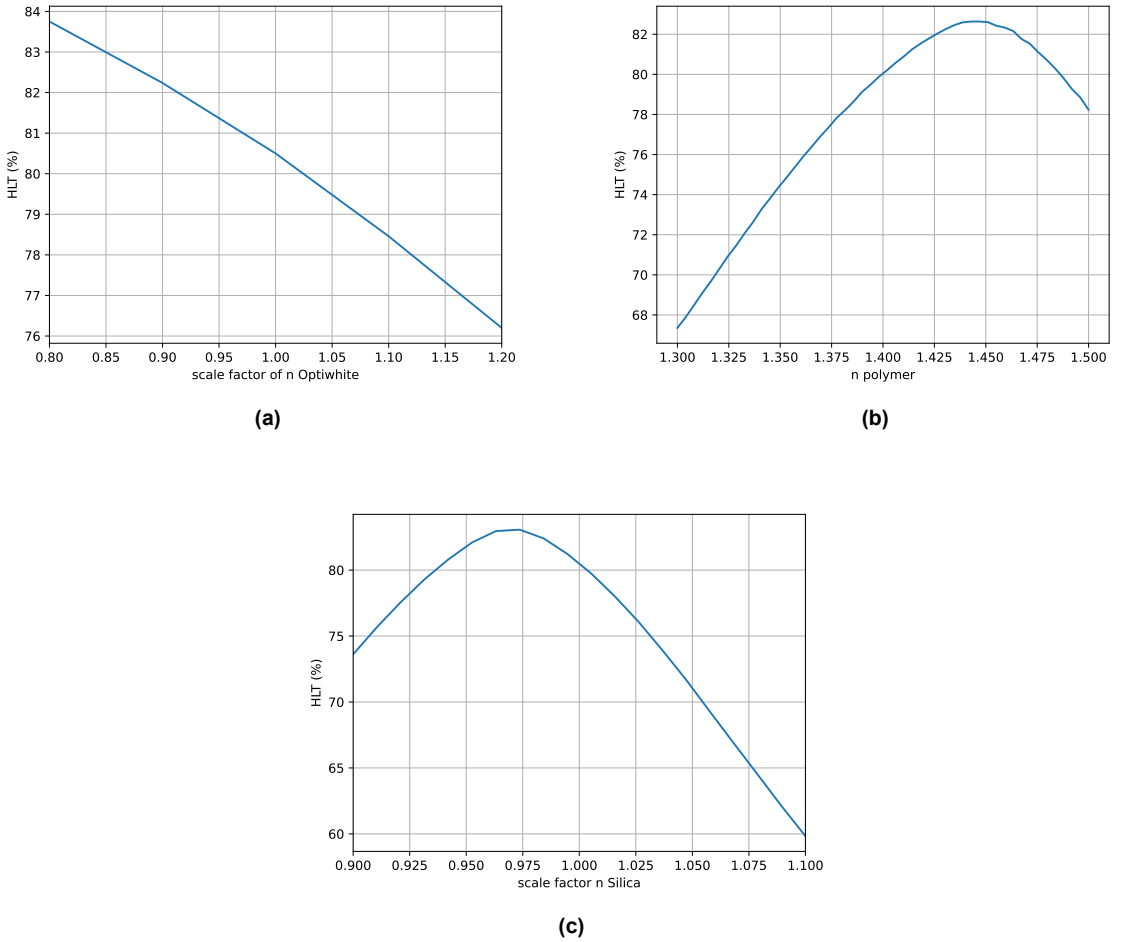

Figure 5.20: Simulations done varying the scale factor of n of Optiwhite (a), varying n of the polymer (b), and varying the scale factor of n of silica (c). For all simulations, $t_{dry} = 35.4$ µm, d = 160 nm, and $1 \cdot 10^6$ photons are used.

homogeneously porous, with pores smaller than the wavelength of visible light and filled with water. It could be that the material is less porous (near the surface) than expected, resulting in a larger n. Thus, while scaling n of Optiwhite by a factor of 0.93, which improved the match between simulation and experiment, may decrease the overlap of HLT between measurement and simulation for coatings with silica particles, this can be compensated by minimal variations in n of silica, or possibly n of the polymer.

To gain more insight, accurate data on the refractive index of both the used silica particles and the polymer is needed. Section 5.3.2 suggested finding n of the polymer, while determining the wavelength-dependent n of silica particles is more challenging. Choosing particles without significant porosity and with a better-determined refractive index might be better for future experiments.

Surface scattering

In sections 5.2.2 and 5.3.2 for plain Optiwhite and coatings without silica, surface roughness was not a likely cause for the mismatch. However, measured HS values for current coatings with silica particles are much larger. Section 5.4.1 suggested a possible complex interaction between surface and particle scattering. This increased scattering might affect measured HLT values. To explore this further, creating coatings with less surface roughness would be interesting.

Particle agglomeration

Section 5.4.1 suggested that particle agglomeration might explain the difference between measurement and simulation. Simulating HS for particles with d = 1 µm provided a reasonable match between measured and simulated wavelength-dependent HS. To explore its effect on HLT, the particle size was set to 1 µm, approximating particles clumped together as one large spherical particle.

The HLT values found are shown in Table 5.1.

t_{wet} (µm)	Measurement (%)	Simulation 160 nm (%)	Simulation 1 µm (%)
50	82.68	82.31	81.51
100	81.33	81.64	80.37
150	80.15	81.04	79.39
200	79.73	80.49	78.53

Table 5.1: Comparison of HLT measurement for $d = 160$ nm and HLT simulation for $d = 160$ nm and $d = 1$ µm.

For most thicknesses, the match between measurement and simulation worsens. However, due to relatively small differences, particle agglomeration cannot be excluded as the chosen particle size was not optimized for the best match with HS results. Also, the approximation of using a larger sphere to represent a group of particles might give inaccurate results. As mentioned in section 5.4.1, microscopic photographs of the coating could exclude this possibility of particle agglomeration.

5.4.3. Angle dependent transmission

Thus far, only the single HLT value has been discussed for the d = 160 nm particle-based coatings. Examining the angular dependence of the transmission allows for a more detailed comparison between measurement and simulation. As shown in Figure 4.12 and discussed in section 4.2.3, simulations tend to overestimate transmission at higher angles θ.

To investigate this discrepancy, several input parameters were varied. First, n of Optiwhite was scaled by a factor of 0.93 and n of silica was scaled by a factor of 1.01. These values were chosen based on realistic variations discussed in section 5.4.2, which maintained the overlap in HLT between measurement and simulation but improved the overlap for samples without silica.

Given that the measured HS was significantly higher than simulated, it is essential to explore whether altering the input parameters to artificially increase scattering could explain the observed difference in angle-dependent transmission. As discussed in section 5.4.1, one possible explanation is that surface roughness enhances particle scattering in a complex manner. In an attempt to reproduce this, the simulated scattering was artificially increased by doubling the weight percentage of silica to 30 wt% and increasing the coating thickness to 100 µm. Both adjustments increase the number of silica particles, thereby increasing scattering. Another possible explanation for the increased scattering is particle agglomeration. Simulations with silica particles of $d = 1$ µm yielded HS results similar to those measured, so this scenario was also simulated.

To compare these transmission curves, each with varying transmission values, they were normalized to the zero-angle transmission. The focus is on determining whether the relative decrease in transmission at higher angles seen in the measurements can be simulated. All normalized angle-dependent simulations with varying input parameters are shown in Figure 5.21.

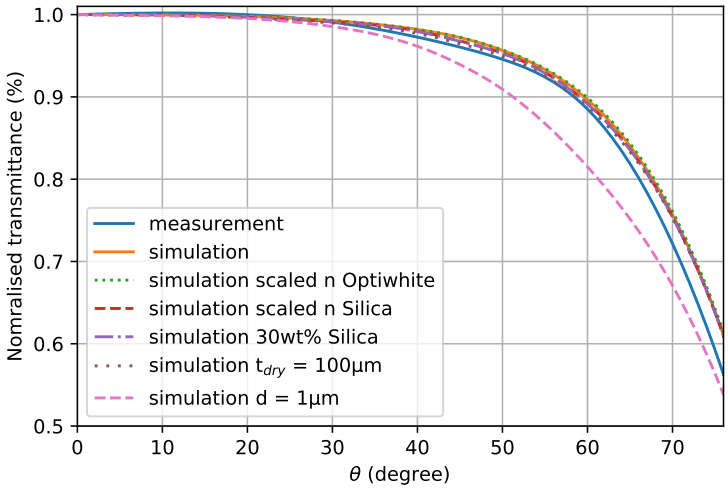

Figure 5.21: Measurements and simulations of the normalized angle-dependent transmission. Apart from the original simulation inputs, results scaling n of Optiwhite by 0.93, scaling n of silica by 1.01, increasing the weight percentage of silica to 30 wt%, increasing t_{dry} to 100 µm, and using silica with $d = 1$ µm are shown. For these simulations, $1 \cdot 10^6$ photons were used.

Comparing the measurement and original simulation, the measurement shows a slight relative decrease at $\theta = 40 - 50°$. This was not initially visible from Figure 4.12 in the results but can also be interpreted as a local increase at $\theta = 60°$, with a general decrease for angles larger than 30°. This is similar to what is seen before where the angle-dependent transmission of plain Optiwhite showed more transmission measured at $\theta = 60°$ than simulated, as seen in Figure 5.6. This effect could not be explained using the simulation, indicating a similar origin. For this reason, this slight increase will not be treated here.

Scaled n of Optiwhite and silica

Scaling n of Optiwhite and silica shows that only scaling n of silica affects the shape of the normalized angle-dependent transmission curve. However, the effects are too minimal to explain the decreased transmission from the measurement. Thus, varying the simulation input parameters that gave the best results for the single-valued HLT did not match the angle-dependent transmission between simulation and measurement.

Increased silica concentration and coating thickness

Increasing the weight percentage of silica and the coating thickness shows a slight decrease for angles higher than $\theta = 40°$, but not at $\theta = 75°$. Thus, artificially increasing scattering in this manner does not explain the measured decrease at 75° relative to the simulation. However, this may not fully encapsulate the true scattering profile. HS measurements in section 5.4.1 found less wavelength dependence than simulated, where increasing the amount of scatter particles is not expected to change the simulated wavelength dependence. Thus incorporating surface scattering into the simulation seems to be necessary for accurately simulating the angle-dependent transmission. LightTools cannot currently work with location-dependent surface roughness, but future attempts could assign an angle-dependent scatter probability when interacting with the top of the coating.

Increasing the particle size

The transmission curve from increasing the particle size to d = 1 µm shows a very different shape than measured. The found average HLT values were similar, as discussed in section 5.4.2, indicating that compared to d = 160nm particles, the transmission at lower angles is higher. Mie theory explains this as more forward scattering for larger particles. Due to the large difference in curve shape, this method of approximating particle agglomeration does not match simulation and measurement well.

Thus, particle agglomeration is less likely the cause of the large HS values measured. However, this does not disprove it, as these simulations approximated agglomeration with single large spherical particles, which may not give accurate results.

HLT measurement setup discrepancies

Because the decrease at $\theta = 75°$ cannot currently be simulated, it might be an artefact from the HLT measurement setup, becoming more prominent for higher scattering coatings. Effects such as misalignment or angle-dependent absorption at the edge of the integrating sphere's opening could be explored by varying alignment and parameters of the integrating sphere, such as port size and wall thickness.

5.5. Coating with d = 400 nm

This section will discuss the results and analysis of the coatings with silica particles of diameter d = 400 nm. The discussion is divided into three main parts. First, the Hortiscatter (HS) results will be examined, as the measurements showed significantly higher HS values compared to simulations, indicating potential issues with surface scattering. Next, the single-valued Hemispherical Light Transmission (HLT) will be compared between measurement and simulation, due to the observed discrepancies. Finally, the angle-dependent transmission will be analyzed in detail to explain the observed differences in angular dependence, which may be influenced by increased scattering and experimental setup imperfections.

5.5.1. Hortiscatter

When examining the HS results for a coating with silica particles of diameter d = 400 nm, shown in Figure 4.5, similar results were found compared to the HS of d = 160 nm particles. The simulation predicted larger HS values compared to d = 160 nm, with a slightly less steep exponential decay. However, the measured HS values were again significantly larger than the simulated ones. As discussed in section 5.4.1, there are two main potential causes for the measured HS being larger: surface scattering and particle agglomeration. Therefore these will individually be discussed

Surface Roughness

For the longest wavelengths, similar scattering was measured for all coatings containing silica particles with d = 400 nm and d = 160 nm. This indicates that surface roughness may dominate in this wavelength regime. For the shortest wavelengths, the HS is almost doubled compared to the HS found for d = 160 nm particles, suggesting that particle scattering starts playing a significant role. The measured HS for both d = 160 nm and d = 400 nm particles is linear on a log scale, demonstrating exponential decay.

Simulations could not produce HS values similar to those measured using the expected particle size. Due to the similarity of the process described for d = 160 nm, the reader is referred to section 5.4.1 for a more detailed analysis. A potential explanation could be that surface scattering and particle scattering interact in a complex way to produce large HS values.

Particle Agglomeration

For these coatings, no visible particle agglomeration was present. However, this does not exclude its presence. As discussed in section 5.4.1, approximating particle agglomeration by simulating HS with silica particles of $d = 1$µm provided a better match between measurement and simulation, as shown in Figure 5.17. Due to the found HS being higher than for d = 160 nm, a slightly larger particle is expected to give similar HS results as measured. Unfortunately, this effect cannot be simulated. Microscopic photos can be taken to rule out the effects of particle agglomeration.

5.5.2. Hemispherical Light Transmission

From the HLT results in section 4.2.4, a worse overlap was found between measurement and simulation compared to the coatings with particles of d = 160 nm. Simulations consistently overestimated the HLT values compared to measurements, with the difference growing larger for increasing coating thickness, from 1% to 3%. For particles with d = 160 nm, the decrease in overlap for larger coating thicknesses was attributed to incorrect assumptions about the dry coating thickness. Due to the similarity of the situation, it is likely to place a role here as well with the same reasoning. For a more detailed analysis, the reader is referred to section 5.4.2.

Varying n of Optiwhite, the Polymer, and Silica

As with the previously discussed coatings, the simulation parameters were varied to explore their effect on HLT values. This is particularly interesting because certain scale factors on refractive indexes were found to improve the overlap between simulation and measurement. By varying these input parameters, it can be determined if the found values give reasonable results for the coatings with d = 400 nm silica particles. The HLT results of varying the scale factor of n of Optiwhite, n of the polymer, and the scale factor of n of silica are shown in Figure 5.22.

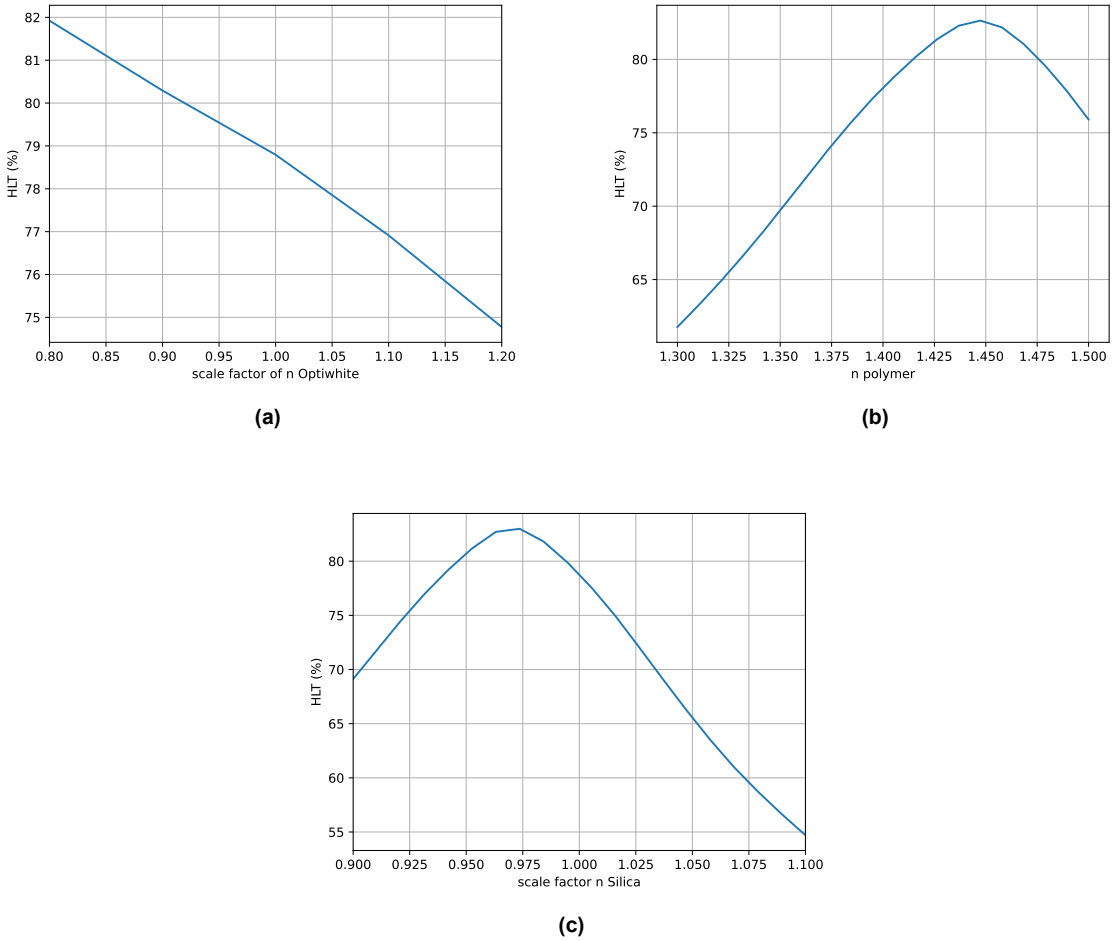

Figure 5.22: Simulations done varying the scale factor of n of Optiwhite (a), varying n of the polymer (b), and varying the scale factor of n of silica (c). For all simulations, $t_{dry} = 35.4$µm, d = 400 nm, and $1 \cdot 10^6$ photons are used.

Similar results were found for d = 160 nm, as shown in Figure 5.20. Scaling n of Optiwhite shows a linear relationship with a similar slope. Scaling both n of silica and n of the polymer again shows a strong correlation, with the curves being mirror images of each other. However, slight variations in n of silica (or of the polymer) have larger effects on the HS for d = 400 nm than for d = 160 nm.

A slight increase in n of silica or a slight decrease in n of the polymer was found to be realistic for d = 160 nm silica coatings, as discussed in section 5.4.2. Using the same values would decrease the HLT value more for d = 400 nm particles compared to d = 160 nm particles due to the increased slope. However, this would increase the overlap between measurement and simulation, as the simulated HLT values for d = 400 nm coatings overestimated the measured values.

While no exact numbers are simulated, the relative change in HLT by tuning the refractive indexes suggests that slight changes, seen to improve the overlap for the other samples, might indeed improve

the match for all simulations thus far. Ideally, this can be verified by simulating the exact HLT values with altered refractive indexes for all coatings. However, to do this properly, uncertainties in the dry coating thickness need to be reduced, as these play a significant role in the simulated values.

While altering the simulation input parameters may explain the difference in measured and simulated HLT, it is important to also keep considering the possibility of the large measured HS playing a role, as well as the possible effects caused by the experimental setup.

5.5.3. Angle-Dependent Transmission

By examining the angle-dependent transmission values, a more detailed comparison between measurement and simulation can be made. Figure 4.14 shows that simulations tend to overestimate transmission for all angles, with the difference increasing at higher angles, except at $\theta = 60°$.

The measurement shows a small local increase at $\theta = 60°$, which was also seen in previous measurements and is expected to have the same origin. For more details, see section 5.2.3.

The more pronounced decrease at $\theta = 75°$ for d = 400 nm particles compared to d = 160 nm is notable, as a relative decrease was found for both coatings. A possible explanation is the visible particle agglomeration found in the coatings with d = 160 nm, discussed in section 4.1.5. These were avoided in HS measurements due to their localized nature, but not in HLT measurements. In this case, the presence of a few larger particles may be the cause of the decreased transmission at higher angles. It was seen in figure 5.21 that a particle of $d = 1$ µm caused a decrease in transmission at higher angles compared to the d = 160 nm particle.

To investigate if the difference between measurement and simulation can be explained by varying the simulation input parameters, the same approach used in section 5.4.3 for d = 160 nm will be repeated. First, n of silica will be scaled by 1.01, as a slight increase was found to potentially improve the overlap between measurement and simulation of the single HLT values. Scaling Optiwhite by 0.93 had no visible effect on the curve, so it will not be discussed further.

Next, the weight percentage of silica will be doubled to 30 wt%, and the thickness of the coating will be increased to $t_{dry} = 100$µm. This will again be an attempt to explore the effects of artificially increasing scattering, as HS measurements found more scattering than simulated.

All normalized angle-dependent simulations with varying input parameters are shown in Figure 5.23.

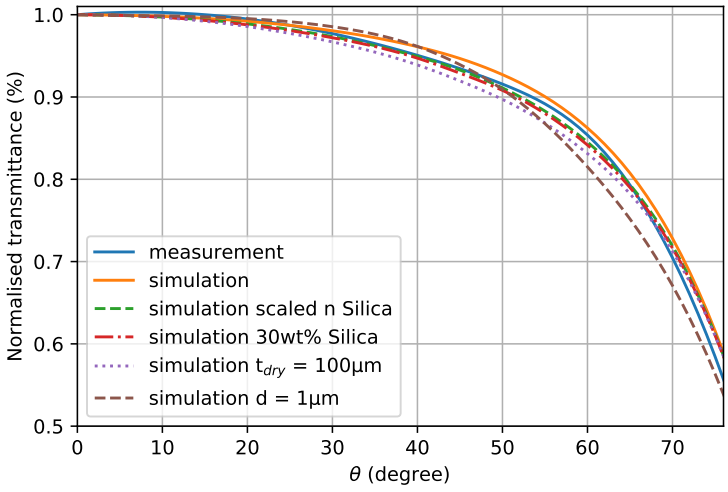

Figure 5.23: Measurements and simulations of the normalized angle-dependent transmission. Apart from the original simulation inputs, results from scaling n of silica by 1.01, increasing the weight percentage of silica to 30 wt%, and increasing t_{dry} to 100 µm are shown. For these simulations, $1 \cdot 10^6$ photons are used.

Scaled n of Silica
Similar effects to those seen for d = 160 nm particles appear, but they are more significant. Scaling n with a minimal factor, can potentially explain the decreased transmission at higher angles but does not explain the decrease at $\theta = 75°$.

Increased Silica Concentration and Coating Thickness
Increasing the weight percentage of silica and coating thickness significantly decreases transmission at higher angles, even overestimating the decrease. However, this does not explain the decrease at $\theta = 75°$.

Particle Agglomeration
From this, the same conclusion is found as for d = 160 nm where the simulations cannot explain the relative decrease found from measurements at $\theta = 75°$. While particle agglomeration has not been proven, it may be able to explain the decrease, as larger particles expect more forward scattering which is expected to decrease the transmission at higher angles.

HLT measurement setup discrepancies
Finally, the possibility remains that the relative decrease in measured transmission is an artefact of the HLT setup, becoming more apparent for coatings that scatter more light. For more details, see section 5.4.3.

5.6. Coating with d = 5 µm
This section will discuss the results and analysis of the coatings with silica particles of diameter d = 5 µm. The discussion is divided into three main parts. First, the Hortiscatter (HS) results will be examined, as the measurements showed significant differences compared to simulations showing complex patterns. Next, the single-valued Hemispherical Light Transmission (HLT) will be compared between measurement and simulation, which was found to have a huge mismatch. Finally, the angle-dependent transmission will be analyzed in detail to understand the differences in angular dependence at lower and higher angles, which may be influenced by increased scattering and experimental setup imperfections.

5.6.1. Hortiscatter
From the HS results of the coatings with silica particles of d = 5 µm, shown in Figure 4.6, different results were found compared to the other particle sizes.

When examining the simulation results, an exponential decay was observed for longer wavelengths, but not for shorter wavelengths, where a more complex pattern emerged. A potential explanation is that in this regime, the particle size is on the same order of magnitude as the coating thickness. Therefore, for small thicknesses, light can generally interact with only one silica particle. As the coating thickness increases, the possibility for multiple interactions becomes larger, especially for shorter wavelengths, causing deformation of the curve. Another explanation for the deformation in simulated HS at lower wavelengths is that when the coating scatters more light, the HS calculation method behaves differently as it approaches an asymptote near an HS value of 100%. Comparing the angle-dependent intensity distributions could provide more insight, but this is outside the scope of this thesis.

For the measurements, an almost wavelength-independent HS was found, which increased with coating thickness. The HS values for the thinnest coating behaved slightly differently, which will be discussed in more detail later in this section.

Surface Roughness
For other particle sizes, a potential explanation for the mismatch between measurement and simulation of HS was a complex interplay between surface scattering and particle scattering. It was found that the exponential wavelength dependence expected from simulations was shifted to higher values for the measurements. Also, the slope of the exponential was decreased.

For the particles with d = 5 µm, a more complex effect is visible. This may be due to the HS calculation method behaving differently as it approaches an asymptote near 100% HS. Where in this case the found effect of considering surface roughness in the past is not changed, but the method of HS calculation

causes different results. Comparing the angle-dependent scatter intensity values directly could give more insight, but this is outside the scope of this thesis.

Particle Agglomeration

For other particle sizes, another potential explanation for the mismatch in HS between measurement and simulation was particle agglomeration. Due to the size of the particles and the dry coating thickness being on the same order of magnitude, big effects due to particle agglomeration are hard to realise. For this reason, it can be concluded that if particle agglomeration plays a role in decreasing the overlap between measurements and simulations of HS, it is not the only one. As surface roughness has been shown with profilometer measurements, as well as its effect on HS being found for the coatings without silica, it is proven to play a role. In the case of particle agglomeration, the only real indication is visible agglomeration from the d = 160 nm particle coatings, which was visible with the naked eye. However, the HS setup did not measure at these locations as the visible particles were spread out throughout the coating with reasonable spacing. From this, it is more likely that surface roughness is the main reason for the discrepancies between measured and simulated HS. As mentioned before, microscopic images can be taken to prove this statement.

Double Coatings

Until now, the double coatings, as explained in more detail in section 3.4, have not been discussed. This is because there was no significant difference in the measured HS when switching the layer in which the silica particles are located. However, when looking at the HS measurement of both coatings, a difference is now visible. This indicates that particles are extruding from the polymer. This would be expected as the particle size of diameter d = 5 µm is on the same scale as the expected coating thickness, being around 9 µm.

A possible explanation for extruding particles causing lower HS values could be the surrounding refractive index. Generally, when the difference in refractive index between the scatter particle and the surrounding increases, the effects of Mie theory, in this case more forward scattering, are enhanced. Here, more forward scattering may reduce the measured HS values.

This can be seen when looking at the total intensity over all wavelengths found at each angle from the HS measurement of the double coatings containing d = 5 µm particles, shown in Figure 5.24.

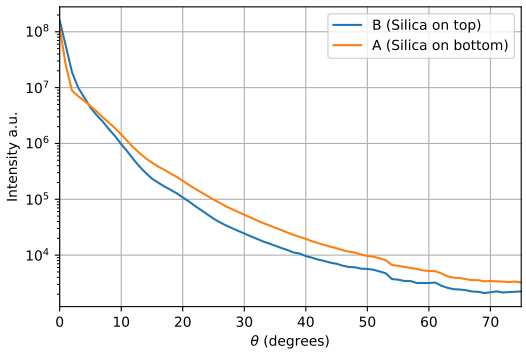

Figure 5.24: The angle dependent intensity distribution from the HS measurement of the double coatings of d = 5 µm particles.

From this, it can be seen that more forward scattering is present when silica is on top, which could explain why the measured HS values are lower.

The fact that particles are extruding in the thinnest coating also explains the difference in the shape of the measured HS distribution seen for the thinnest coating in Figure 4.6 compared to the other thicknesses. If this sample were to have a layer of only polymer without silica on top, as seen in Figure 4.7c, it would better match the pattern seen in the other coating thicknesses. Note that the bottom layer of the double coating is the same coating as t_{wet} = 50 µm from Figure 4.6.

5.6.2. Hemispherical Light Transmission

From the HLT results in section 4.2.5, a significant difference was found between measurement and simulation. For the lowest coating thickness, the simulation found 5.42% larger values, which increased to 9.25% for the thickest coating.

The uncertainty in coating thickness, as discussed for the coatings with silica d = 160 nm in section 5.4.2, cannot explain the current mismatch as none of the simulated thicknesses gives values close to any of the measured values. Due to this large difference, it was found that varying the simulation input parameters, as done for the other particle sizes, is insufficient to explain the difference between measured and simulated HLT. This will become more apparent when examining the angle-dependent transmission in the next section.

5.6.3. Angle-Dependent Transmission

By examining the angle-dependent transmission values, a more detailed comparison between measurement and simulation can be made. From Figure 4.16, significant differences are present between measurement and simulation. Measurements show lower transmission, especially at lower and larger angles. To investigate if varying the simulation input parameters can provide insight into the origin of these discrepancies, a similar approach used in section 5.4.3 will be repeated.

Varying Simulation Parameters

First, n of silica was scaled by 1.01, as this showed promising effects for the previous particle sizes. Additionally, simulations were performed where the silica density was increased to 30 wt% and the dry coating thickness was increased to 100 µm to see if artificially adding more scattering would produce the desired effects. All these variations are shown normalized in Figure 5.25. Because the decrease at lower angles could not be reproduced and is assumed to be an experimental artefact, the measurement data was normalized to the largest value at $\theta = 15°$ to compare the effects found at higher angles.

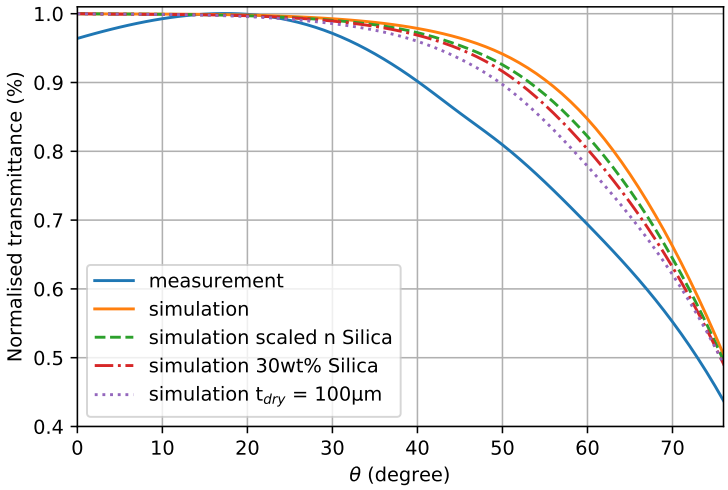

Figure 5.25: Measurements and simulations of the normalized angle-dependent transmission. Apart from the original simulation inputs, the results scaling n of silica by 1.01, increasing the weight percentage of silica to 30 wt%, and increasing t_{dry} to 100 µm are shown. For these simulations, $1 \cdot 10^6$ photons are used.

All varied parameters decrease the transmission at higher angles; however, at $\theta = 75°$, the effects are minimal. While a visible decrease is seen, they individually cannot explain the decrease found in measurements. The increase in transmission from $\theta = 0°$ to 15° and the strong decrease at $\theta = 75°$ could not be explained with simulations. Therefore, two possible explanations are: the simulation assumptions are incorrect where excluding surface scattering causes the discrepancies, or the measurement setup itself is the cause of the differences. These will both be discussed individually.

Surface Scattering

Combining all parameters might achieve a significant decrease at $\theta = 40 - 60°$. However, due to the scale of the difference, the current simulations are likely unable to fully capture the situation. Since a decrease at higher angles was able to be simulated, it could be that the found mismatch is due to the simulation not accurately describing the actual scatter behaviour. This could be seen by comparing the HS of measurements and simulations. In this case, the origin would arise from the simulation not incorporating surface scattering, which may be the reason for the increased, mainly wavelength-independent, scattering.

HLT Measurement Setup Discrepancies

The increase in transmission from $\theta = 0°$ to 15° could not be explained by the current simulation and is assumed to be an artefact of the experimental setup. To test this, another coating with visibly similar scatter properties from Fotonic was measured. From this a similar effect was seen, indicating this setup artefact might only become apparent for high scattering samples. One possibility could be the beam size used in the HLT setup. At $\theta = 0°$, the beam size is only marginally larger than the port of the integrating sphere. As the angle of incidence θ increases, the beam becomes oval-shaped and increases in size. This is a similar effect to what is seen for the change in the shape of the acceptance area of the detector when increasing the angle described in the HS setup optimisation.

It is possible that the beam being too small at low angles decreases the true transmission, as light interacting with the coating just outside the sample port may scatter towards the port. This is consistent with the fact that this low-angle decrease is only seen for coatings that scatter more light. Preliminary tests with a larger beam size suggested this, but the enlarged beam's low intensity produced inconsistent results due to a low signal-to-noise ratio. To confirm that the decrease measured at lower angles can be attributed to the beam size being too small, a larger collimated beam with sufficient intensity should be used.

The decrease at $\theta = 75°$ could not be explained using the simulation for all coatings, and this effect became more dominant for the coatings with particles of d = 5 µm. It is possible that the experimental setup used to measure HLT is unable to accurately measure transmission at high angles. This was not seen for plain Optiwhite, indicating that this issue only becomes significant for high-scattering coatings, or for coatings with more forward scattering, both of which are increased for the coatings with particles of d = 5 µm.

For higher scattering, a possible explanation is absorption at the edge of the sample port of the integrating sphere. Because this wall has a nonzero thickness, light entering the integrating sphere opening at a high angle may be absorbed, which would have entered the sphere for a thinner port wall thickness. This is schematically shown in Figure 5.26 below.

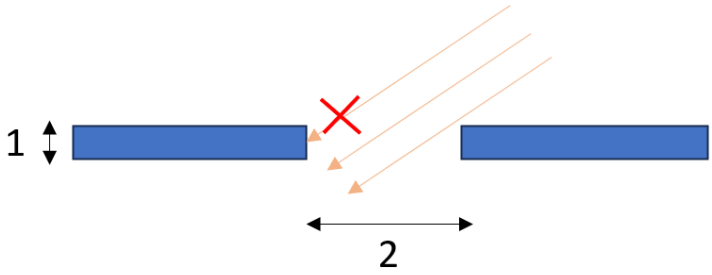

Figure 5.26: Schematic demonstrating the possible effect of the sample port wall thickness absorbing light. 1 is the port wall thickness and 2 is the port diameter.

As the amount of light headed towards the port wall increases for coatings that scatter more light, this may explain the decrease. As this is only relevant for light exiting the sample at close to 90° from the normal, this may also explain a larger decrease for more forward-scattering coatings at higher angles. Light entering the glass at a high angle of 75° only needs to slightly change angle to approach the 90°

exit angle of the sample. More light is scattered this way for forward-scattering coatings, resulting in more absorption at the sample port wall.

Double Coatings

When examining the angle-dependent transmission measured for the double coatings, only a difference was present for the coatings with particle size d = 5 µm, as shown in Figure 4.17c. It was found that for the coatings with silica particles in the top layer, the transmission at higher angles decreases. From HS measurements, it was found that the coatings with silica in the top layer had more forward scattering.

This is consistent with what was assumed before, where more forward scattering could cause a decrease in transmission at higher angles. While this decrease can be explained by the simulations, as seen from comparing the angle-dependent transmission of particles with d = 160 nm and $d = 1$µm in Figure 5.21, the scale of this effect is more likely to have an experimental origin as explained previously. This gives a strong indication that experimental shortcomings in the HLT measurement setup are contributing to the found discrepancies.

6

Conclusion

This thesis investigated the optical properties of monodisperse spherical silica-based coatings using both experimental measurements and Monte Carlo ray tracing simulations, with the primary aim of comparing these methods and identifying potential improvements. This was achieved by varying the particle size and coating thickness in the coatings.

The results revealed significant discrepancies between measured and simulated Hortiscatter (HS) values, with measured HS consistently higher across all particle sizes, showing differences from 5% to 80%. These discrepancies are likely due to the simulations not accounting for surface roughness, which appears crucial in scattering behavior. For smaller particle sizes (160nm and 400nm), the measured HS values exhibited similar wavelength dependence to simulations but with larger values, possibly due to surface roughness. For larger particles (5 µm), the lack of similarity between measured and simulated wavelength dependence of HS suggests complex interactions between particle-based and surface roughness-based scattering in determining HS.

In terms of Hemispherical Light Transmission (HLT), simulations and measurements aligned well, often showing differences below 1% for low-scattering coatings with smaller silica particles (160 nm and 400 nm). Discrepancies were reduced by adjusting the refractive index of the glass and of silica in the simulations. However, this adjustment alone can not fully explain the discrepancies. For high-scattering coatings, the simulations failed to predict outcomes accurately, indicating a significant role for surface scattering. Additionally, the HLT measurement setup might not accurately capture the transmittance for highly scattering coatings. This experimental shortcoming likely contributes to the observed discrepancies, suggesting a combination of both factors at play.

To enhance the accuracy of both simulations and experimental measurements, future work should focus on refining simulation models to incorporate surface roughness and improve predictive capabilities for a broader range of coating compositions. Obtaining precise input parameters, such as the refractive indices of all elements involved, remains crucial yet challenging. Further improvements to the experimental setups, such as better light shielding to improve the signal-to-noise ratio, could also help ensure more accurate measurements.

This research provides valuable insights into the optimization of greenhouse coatings, demonstrating the potential for theoretical models to predict practical outcomes under specific conditions. The findings underscore the need for continued advancements in both simulation accuracy and experimental methodologies to achieve reliable and efficient designs for enhanced plant growth in greenhouses.

References

[1] Photographer: Markus Spiske. Accessed: 2024-06-15. 2024. URL: https://unsplash.com/photos/black-metal-fence-v1Wgbzd5IOo.

[2] United Nations. *Population*. Accessed: 2024-05-09. 2024. URL: https://www.un.org/en/global-issues/population#:~:text=Our%20growing%20population&text=The%20global%20human%20population%20reached,and%202%20billion%20since%201998.

[3] Wageningen University & Research. *Meta-analyse laat zien dat de vraag naar voedsel met 35 tot 56% zal stijgen tussen 2010-2050*. Accessed: 2024-05-09. 2024. URL: https://www.wur.nl/nl/onderzoek-resultaten/onderzoeksinstituten/economic-research/show-wecr/meta-analyse-laat-zien-dat-de-vraag-naar-voedsel-met-35-tot-56-zal-stijgen-tussen-2010-2050.htm.

[4] S. Hemming, V. Mohammadkhani, and T. Dueck. "Diffuse greenhouse covering materials-material technology, measurements and evaluation of optical properties". In: *International Workshop on Greenhouse Environmental Control and Crop Production in Semi-Arid Regions*. Vol. 797. 2008, pp. 469–475.

[5] ReduSystems. *Top Quality Lisianthus Benefits from Diffuse Coating*. Accessed: 2024-05-09. 2024. URL: https://www.redusystems.com/en/articles/top-quality-lisianthus-benefits-from-diffuse-coating.

[6] L. F. M. Marcelis et al. "Quantification of the growth response to light quantity of greenhouse grown crops". In: *V International Symposium on Artificial Lighting in Horticulture*. Vol. 711. 2005, pp. 97–104.

[7] Frank Kempkes, Arthur Maaswinkel, and Patrick M. M. van der Zalm. *Diffuus kasdek-maak het eens helder*. Tech. rep. Stichting Wageningen Research, Wageningen Plant Research, Business unit ..., 2021.

[8] *Greenhouse glass - Determination of optical properties of greenhouse covering materials and screens*. 2018.

[9] B.J.M. Slotboom. "Optimization of Optical Properties of Greenhouse Particle-Based Spray Coating Configuration". Master's thesis. TU Delft, 2023.

[10] Andrew Zangwill. *Modern electrodynamics*. Cambridge University Press, 2013.

[11] Max Born and Emil Wolf. *Principles of Optics: Electromagnetic Theory of Propagation, Interference and Diffraction of Light*. 7th (expanded). Pergamon Press, 1999. ISBN: 978-0521642224.

[12] J. A. Stratton. *Electromagnetic Theory*. 2007.

[13] J. D. Jackson. *Classical Electrodynamics, 3rd ed.* 1999.

[14] G. Mie. "Beiträge zur Optik trüber Medien, speziell kolloidaler Metallösungen". In: *Annalen der Physik* 330.3 (1908), pp. 377–445. DOI: 10.1002/andp.19083300302.

[15] Yuriy A. Akimov. "Mie scattering theory: A review of physical features and limitations". In: *Institute of High Performance Computing (IHPC), Agency for Science, Technology and Research (A*STAR)* (Jan. 2024).

[16] Craig F Bohren and Donald R Huffman. *Absorption and Scattering of Light by Small Particles*. Wiley, 1983.

[17] R. Nave. *Mie scattering.* http://hyperphysics.phy-astr.gsu.edu/hbase/atmos/blusky.html.

[18] Gert-Jan Swinkels et al. *Protocol for measuring light transmission of horticultural screens*. Rapport GTB-1252. Wageningen UR Greenhouse Horticulture, 2012.

[19] Illuminating Engineering Society. *Directional Hemispherical Transmittance*. https://www.ies.org/definitions/directional-hemispherical-transmittance/. Accessed: 2024-02-27.

[20] Michael Hartley. *Spherical Coordinates Image*. Accessed: 2023-04-03. 2023. URL: http://hartleymath.com/calculus3/triple-integrals-spherical-coordinates.

[21] E.P. Vernhout. "Designing, Constructing and Testing a Hortiscatter & UV to PAR Setup". MA thesis. 2023.

[22] SYNOPSYS. *LightTools Illumination Design Software.* https://www.synopsys.com/optical-solutions/lighttools.html..

[23] Pilkington. *Pilkington Optiwhite*. https://www.pilkington.com/nl-nl/nl/products/product-categories/special-applications/pilkington-optiwhite. [Accessed: 23-May-2024]. 2024.

[24] Mikhail N. Polyanskiy. *Refractiveindex.info database of optical constants*. Accessed: 22/05/2024. 2024. URL: https://refractiveindex.info/.

[25] R. E. Treharne. "RF magnetron sputtering of transparent conducting oxides and CdTe/CdS solar cells". Numerical data kindly provided by Dr. Robert Treharne. PhD thesis. University of Durham, 2011.

[26] National Renewable Energy Laboratory (NREL). *NREL Reference Air Mass 1.5 Spectra*. Online. Available at: https://www.nrel.gov/grid/solar-resource/spectra-am1.5.html. Year of access.

[27] Zeiss. *Xenon Arc Lamps*. https://zeiss-campus.magnet.fsu.edu/articles/lightsources/xenonarc.html. Accessed: 2024-05-25. 2024.

[28] Thorlabs. *Off-Axis Parabolic Mirrors and the Angle Between Optical and Focal Axes*. https://www.thorlabs.com/newgrouppage9.cfm?objectgroup_id=14192. Accessed: 2024-05-25. 2024.

[29] R. Langer and D. A. Tirrell. "Designing materials for biology and medicine". In: *Nature* 428.6982 (2013), pp. 487–492. DOI: 10.1038/nature02388. URL: https://www.ncbi.nlm.nih.gov/pmc/articles/PMC4279762/.

[30] Business Research Insights. *Spherical Silica Market Size, Share, Growth, and Forecast [2022-2028]*. Accessed: 2024-05-09. 2022. URL: https://www.businessresearchinsights.com/market-reports/spherical-silica-market-101331.

[31] Pan Hao et al. "Comprehensive understanding of the synthesis and formation mechanism of dendritic mesoporous silica nanospheres". In: *Nanoscale Advances* 2.5 (2020), pp. 1792–1810. DOI: 10.1039/D0NA00219D.

[32] Various. "Safety aspects and handling of nanomaterials in water-based dispersions". In: *Journal of Nanoparticle Research* 22.5 (2020), pp. 150–170. DOI: 10.1007/s11051-020-04872-6.

[33] Alpha Nanotech. *Plain Silica Nanoparticles*. Accessed: 2024-05-09. 2024. URL: https://www.alphananotechne.com/plain-silica-nanoparticles.

[34] Werner Stöber, Arthur Fink, and Ernst Bohn. "Controlled growth of monodisperse silica spheres in the micron size range". In: *Journal of Colloid and Interface Science* 26.1 (1968), pp. 62–69.

[35] A Bielanski, J Deren, and J Haber. "Infrared spectra of surface hydroxyl groups and crystalline structure of oxides". In: *Nature* 189 (1961), pp. 812–813.

[36] W. D. Kingery, H. K. Bowen, and D. R. Uhlmann. *Introduction to Ceramics*. John Wiley & Sons, 1976, pp. 500–501.

[37] C. J. Brinker and G. W. Scherer. *Sol-Gel Science: The Physics and Chemistry of Sol-Gel Processing*. Discusses the retention of water in silica pores due to capillary forces, gel structure, drying process, and surface hydroxyl groups. Academic Press, 1990, pp. 789–795.

[38] X. Zhao et al. "Surface modification of silica nanoparticles with hydroxyl groups: Impact on bulk properties". In: *Journal of Nanoparticle Research* 18.5 (2016), pp. 123–134.

[39] H. Malitson. "Interspecimen comparison of the refractive index of fused silica". In: *Journal of the Optical Society of America* 55.10 (1965), pp. 1205–1208.

[40] M. Daimon and A. Masumura. “Measurement of the refractive index of distilled water from the near-infrared region to the ultraviolet region”. In: *Applied Optics* 46.18 (2007), pp. 3811–3820.

[41] *Understanding Chemical Resistance in Epoxy System*. https://www.coatingsworld.com/issues/2020-06-01/view_technical-papers/understanding-chemical-resistance-in-epoxy-system/. Accessed: 2024-02-28. June 2020.

[42] Jerald W. Caruthers. “On Rayleigh and Mie scattering”. In: *The Journal of the Acoustical Society of America* 130.4$_{supplement}$ (2011), p. 2554. DOI: 10.1121/1.3655229.

[43] G. Berk and F. Zernike. *Light Scattering in Solids*. Covers the theoretical foundations of Rayleigh scattering in solids, including glass. Springer, 1975. ISBN: 978-3-540-07301-4.

[44] Eckhardt Optics. *Optical Scattering and Surface Roughness*. 2023. URL: https://www.eckop.com/optical-scattering-and-surface-roughness.

[45] Victoria Marcune and Shawn Iles. *Understanding Surface Roughness*. 2023. URL: https://www.edmundoptics.com/knowledge-center/application-notes/optics/understanding-surface-roughness.

[46] NSG Group. *NSG Group - Changing our surroundings, improving our world*. Accessed: 2024-06-14. 2024. URL: https://www.nsg.com/.

[47] Bruker. *Ellipsometry Tutorial*. Accessed: 2024-06-14. 2024. URL: https://www.bruker.com/.

[48] J.M. Bennett and L. Mattsson. *Polarization*. Chapter 4 discusses the impact of surface roughness on scattering. New York: Wiley, 1961.

[49] J. E. Mark et al. “Optical Properties of Polymers”. In: *Polymer Handbook*. 4th. Wiley-Interscience, 2005. Chap. V/21, pp. 489–496. ISBN: 978-0471387006.

[50] Edward D. Palik. *Handbook of Optical Constants of Solids*. Academic Press, 1998. ISBN: 978-0-12-544415-6.

[51] P. Kumar et al. “Analytical treatment of light extraction from textured surfaces using classical ray optics”. In: *Optics Communications* 284 (2011), pp. 4874–4878.

[52] Zheng Li and Kamel Abdelmouleh. “Effects of Particle Size on the Agglomeration and Stability of Silica Nanoparticles”. In: *Journal of Nanoparticle Research* 10.7 (2008), pp. 1343–1351. DOI: 10.1007/s11051-007-9347-y.

A

List of Recommendations

A.1. HS Measurement Setup

- **Action**: Implement the possibility of rotating the sample while keeping the normal of the face in the same direction.
  - **Goal/Reason**: To measure possible anisotropic behavior and average out.
- **Action**: Increase the distance between the detector and the diaphragm.
  - **Goal/Reason**: To reduce unwanted light detection.
- **Action**: Improve isolation from external light.
  - **Goal/Reason**: To ensure only light through the diaphragm is detected.
- **Action**: Use a less wavelength-independent light source that doesn't oversaturate the spectrometer for the reference measurement.
  - **Goal/Reason**: Allows the removal of the neutral-density filter.
- **Action**: Increase integration time when possible.
  - **Goal/Reason**: To avoid oversaturation while maximizing data quality.
- **Action**: Perform multiple measurements at multiple locations or increase the detector acceptance area.
  - **Goal/Reason**: To reduce location dependence. Spatial resolution must remain at 1%.

A.2. HLT Measurement Setup

- **Action**: Increase port size.
  - **Goal/Reason**: To minimize possible relative angle-dependent absorption of the sample port wall.
- **Action**: Adjust relevant system parameters and measure a mid/high scatter coating.
  - **Goal/Reason**: To see if unusual effects appear or decrease.
- **Action**: Adjust the setup to measure according to NEN standards.
  - **Goal/Reason**: Ensures the light source switches port while the sample remains stationary.

A.3. Simulation Improvements

- **Action**: Add small Rayleigh scatter particles.
  - **Goal/Reason**: To mimic small impurities for plain Optiwhite or similar coatings.

- **Action**: Implement surface roughness or an average scatter profile to the surface.
  - **Goal/Reason**: Current simulations may not incorporate location dependence at the surface roughness scale.

A.4. Coating Production

- **Action**: Use a centrifuge and pipette to reduce water content and avoid heating.
  - **Goal/Reason**: To prevent agglomeration.
- **Action**: Take microscopic photographs of the produced polymer with particles.
  - **Goal/Reason**: To determine the presence of agglomeration.
- **Action**: Artificially vary surface roughness.
  - **Goal/Reason**: To explore its effects.

B

Pictures of coatings

Pictures of the produced coatings without silica and for the three silica particle sizes can be seen below in figure B.1. For all these coatings the wet thickness (t_{wet}) was 100µm.

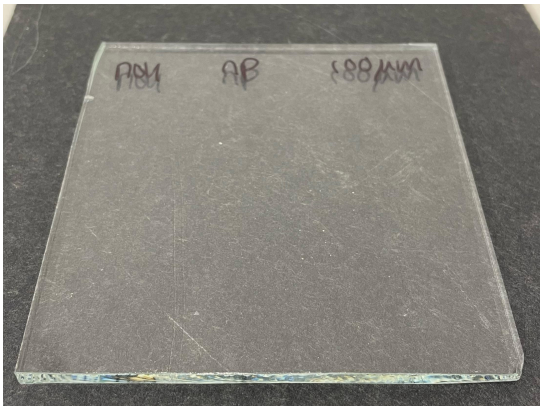

(a) No silica

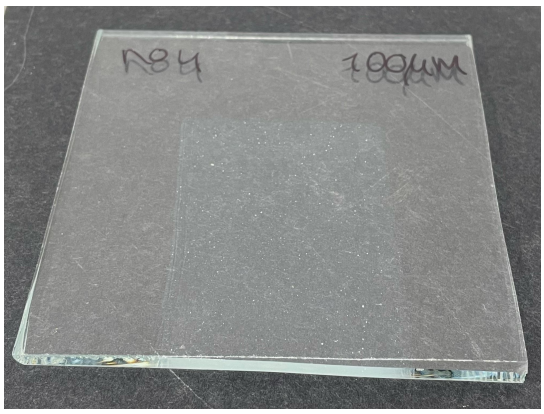

(b) Silica with d = 160nm

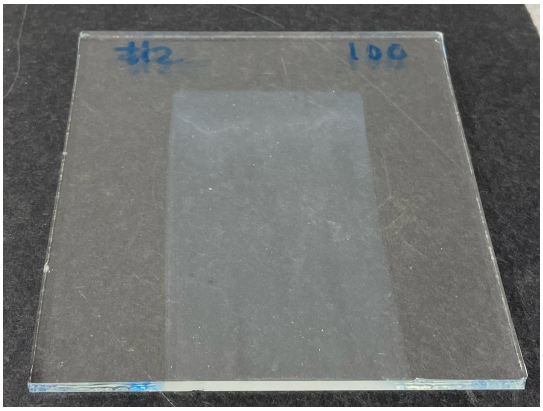

(c) Silica with d = 400nm

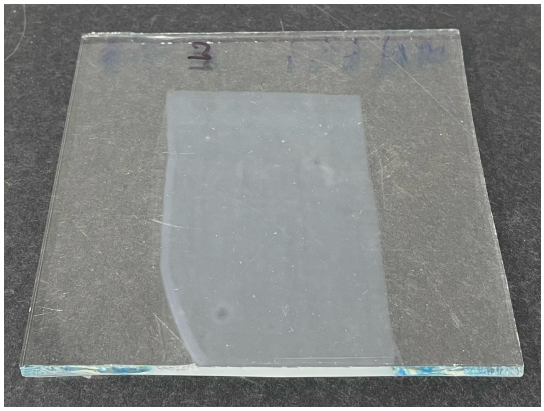

(d) Silica with d = 5µm

Figure B.1: Pictures of the different coating types. (a) without silica particles, and (b)-(d) containing 15wt% silica particles of diameters d = 160nm, 500nm and 5µm respectively. All coatings were bar coated with a wet thickness of 100µm.

C

Python code

C.1. HS analysis code

Below is the code used to analyse HS data

```
from netCDF4 import Dataset
from pathlib import Path
import numpy as np  # Ensure numpy is imported
import sys
from pathlib import Path
import matplotlib.pyplot as plt
import matplotlib.cm as cm
from statistics import stdev

class TRS:
    def __init__(self, file):
        f = file.encode('unicode_escape').decode()  # remove escape characters like \n \t
        self._f = Dataset(Path(f), 'r')

    def info(self):
        for g in self._f.groups:
            print(f"group : {g}")
            for a in self._f[g].ncattrs():
                print(f"\t{a:20} : {getattr(self._f[g], a)}")
            for v in self._f[g].variables:
                self._f[g][v].set_auto_mask(False)
                uLabel = ""
                if 'units' in self._f[g][v].ncattrs():
                    uLabel = f"[{self._f[g][v].units}]"
                print(f"\t{v:20} : {self._f[g][v][:]} {uLabel}")

    # Adjusted to access the wavelength data within the "Ocean Insight spectrometer" group
    @property
    def wavelength(self):
        self._f['Ocean Insight spectrometer']['wavelength'].set_auto_mask(False)
        return self._f['Ocean Insight spectrometer']['wavelength'][:]


    def image(self,i=0):
        self._f['Data']['Image'].set_auto_mask(False)
        Z = self._f['Data']['Image'][i,:,:]
        return Z

    @property
    def rtAngles(self):
        self._f['Setup']['reflecTransAngles'].set_auto_mask(False)
        return self._f['Setup']['reflecTransAngles'][:]


    @property
```

```
    def intTimes(self):
        self._f['Setup']['integrationTimes'].set_auto_mask(False)
        return self._f['Setup']['integrationTimes'][:]

def BlackBody(T,wls):
    h = 6.62607015E-34  # m^2 kg s^-1
    c = 299792458  # m s^-1
    kB = 1.380649E-23  # m^2 kg s^-2 K^-1

    exponent = np.exp(h*c/(wls*1e-9)/kB/T)
    return 2*np.pi*h*c**2/((wls*1e-9)**5)/(exponent-1)

def get_data(filenameSam, filenameSamNoise, filenameRef, filenameRefNoise):
    dataRef = TRS(filenameRef)
    dataSam = TRS(filenameSam)
    dataSamNoise = TRS(filenameSamNoise)
    dataRefNoise = TRS(filenameRefNoise)

    wls = dataRef.wavelength # Wavelengths from spectrometer
    angles =  dataRef.rtAngles #measred angles in degrees
    Int_times_ref = dataRef.intTimes #integration times in seconds
    Int_times_sam = dataSam.intTimes
    Int_times_ref_noise = dataRefNoise.intTimes
    Int_times_sam_noise = dataSamNoise.intTimes


    angles = angles[1:] #two times zero angle which I want to take out, need to change
        measurement procedure later

    Int_times_ref_reshaped = Int_times_ref[:, np.newaxis]
    Int_times_sam_reshaped = Int_times_sam[:, np.newaxis]
    Int_times_ref_noise_reshaped = Int_times_ref_noise[:, np.newaxis]
    Int_times_sam_noise_reshaped = Int_times_sam_noise[:, np.newaxis]



    I_ref = dataRef.image() / Int_times_ref_reshaped           # int times between each sam
        and noise measurement must be equal
    I_ref_noise = dataRefNoise.image() / Int_times_ref_noise_reshaped
    I_sam_noise = dataSamNoise.image() / Int_times_sam_noise_reshaped
    I_sam = dataSam.image() /Int_times_sam_reshaped



    #two times zero angle which I want to take out, need to change measurement procedure
        later
    I_ref = np.delete(I_ref,0,axis = 0)
    I_sam = np.delete(I_sam,0,axis = 0)
    I_sam_noise = np.delete(I_sam_noise,0,axis = 0)
    I_ref_noise = np.delete(I_ref_noise,0,axis = 0)

    I_ref = (I_ref - I_ref_noise)
    I_sam = (I_sam - I_sam_noise)

    I_ref[I_ref <= 0] = 0   #optional, sometimes helps with data noise
    I_sam[I_sam <= 0] = 0

    return I_ref, I_sam, wls


datasets = {

0: {   #before rotation stage was alligned
"sample": r'C:\Users\ingha\Measurement_files\9HS_no2_150.nc'     ,
"sample_noise" : r'C:\Users\ingha\Measurement_files\9HS_no2_150_noise.nc'  ,
"reference" : r'C:\Users\ingha\Measurement_files\9HS_ref.nc',
'reference_noise' : r'C:\Users\ingha\Measurement_files\9HS_ref_noise.nc'
},
}

data_set = 0 #choose data
```

```
A_sam = simulation_dict['Optiwhite']

sample_file = datasets[data_set]["sample"]
sample_noise_file = datasets[data_set]["sample_noise"]
reference_file = datasets[data_set]["reference"]
reference_noise_file = datasets[data_set]["reference_noise"]


I_ref, I_sam, wls = get_data(sample_file, sample_noise_file, reference_file,
    reference_noise_file)

lower_bound = 400  #fill these in based on the image below
upper_bound = 1000
idx_low = np.abs(wls - lower_bound).argmin()
idx_high = np.abs(wls - upper_bound).argmin()

angles = np.arange(0,76,1)
angles_reshaped = angles[:, np.newaxis]


#this part is for the  measurement
TDF_s = (I_sam - (I_ref * I_sam[0,:]/I_ref[0,:])) * np.sin(np.radians(angles_reshaped))
zero_angle_sum = I_ref * I_sam[0,:]/I_ref[0,:] * np.sin(np.radians(angles_reshaped))
TDF_s[0,:] = np.sum(zero_angle_sum, axis = 0)

TDF_r = np.zeros(I_ref.shape)
TDF_r[0,:] = np.ones(len(wls))

TDF_l = np.sin(np.radians(angles_reshaped)) * np.cos(np.radians(angles_reshaped)) / 26.85

TDF_s = TDF_s / TDF_s.sum(axis=0)
TDF_r = TDF_r / TDF_r.sum(axis=0)
TDF_l = TDF_l / TDF_l.sum(axis=0)

TDF_s_adjusted = TDF_s - TDF_l
TDF_r_adjusted = TDF_r - TDF_l
hs_mes = ((1 - np.std(TDF_s_adjusted, axis = 0) / np.std(TDF_r_adjusted, axis = 0)) ** 2) *
    100

I_BB = BlackBody(3200,wls) #wavelength dependent intensities
weighted_hs_mes = hs_mes * I_BB
weighted_hs_mes_mean = np.sum(weighted_hs_mes[idx_low:idx_high])/np.sum(I_BB[idx_low:idx_high
    ])


print("HS mes = " +str(weighted_hs_mes_mean))

plt.plot(wls,hs_mes, label = "measurement", color = default_color)

plt.ylim(0,100)
plt.xlim(lower_bound,upper_bound)
plt.grid()
plt.xlabel("Wavelength (nm)")
plt.ylabel("Hortiscatter (%)")
plt.legend()
plt.show()
```

C.2. HLT analysis code

```
import numpy as np
import matplotlib.pyplot as plt
from Modules_HLT.readNC import HLT
from scipy.interpolate import interp1d
import math

def interpolated_trans(integration_angles, T_a_b):
    # Create an interpolation function
    T_lambda_hem_f = interp1d(x=AOI, y=T_a_b, kind="cubic", fill_value='extrapolate')

    # Interpolate transmission values for the given integration angles
```

```
    interpolated_values = T_lambda_hem_f(integration_angles)
    return interpolated_values

def calc_T_HEM(T_a_b):
    integration_angles = np.linspace(0, 90, 91)
    integration_angles = integration_angles.astype(int)
    integration_radians = [math.radians(deg) for deg in integration_angles]

    interpolated_values = interpolated_trans(integration_angles, T_a_b)
    T_HEM = np.sum(interpolated_values*np.sin(integration_radians)*np.cos(integration_radians
        )) / np.sum(np.sin(integration_radians)*np.cos(integration_radians))
    return T_HEM

file_paths_sam = {
    0: r'C:\Users\ingha\\Measurement_files\\3HLT_optiwhite_sam.nc',
}

file_paths_ref = {
    0: r'C:\Users\ingha\\Measurement_files\\3HLT_optiwhite_ref.nc',
}


samples = np.arange(0, len(file_paths_sam))
tab = np.zeros((len(samples),9))

for s in samples:
    data_sample = HLT(file_paths_sam[s])
    data_reference = HLT(file_paths_ref[s])

    #double beam
    I_1 = np.zeros((9,1044))
    I_2 = np.zeros((9,1044))
    I_3 = np.zeros((9,1044))
    I_4 = np.zeros((9,1044))
    I_T = np.zeros((9,1044))

    for i in range(8):
        I_1[i,:] = data_sample.image()[i] - data_sample.background
        I_2[i,:] = data_sample.reference()[i] - data_sample.background
        I_3[i,:] = data_reference.reference()[i] - data_reference.background
        I_3[i,:] = I_2[i,:]
        I_4[i,:] = data_reference.image()[i] - data_reference.background
        I_T[i,:] = I_1[i,:]/I_2[i,:]*I_3[i,:]/I_4[i,:] * 100


    AOI = np.array([0, 15, 30, 40, 45, 50, 60, 75, 90])

    start_value = 400
    end_value = 700

    wanted_values = np.arange(400,710,10) #we want the values at these wavelengths
    indexes = np.zeros(len(wanted_values))

    for k in range(len(wanted_values)): #finds all the indexes for the wanted wavelengths of
        data_Sam.wavelength
        indexes[k] = min(range(len(data_sample.wavelength)), key=lambda i: abs(data_sample.
            wavelength[i] - wanted_values[k]))

    T_lambda_a_b = I_T[:,indexes.astype(int)]


    A_lambda = np.array([23.64,53.59,56.06,53.25,65.91,75.22,77.42,77.12,
                    79.49,76.17,78.11,78.54,77.84,81.54,80.54,81.75
                    ,80.00,78.44,79.37,74.75,77.15,78.08,77.68,74.96,
                    76.54,74.31,75.63,78.75,76.04,68.72,35.80])

    T_a_b = 0.00045 * np.sum(T_lambda_a_b * A_lambda, axis = 1)

    tab[s,:] = T_a_b

T_a_b = tab[8,:] #adjust first index to which measurement  you want to analyse
```

```
80
81 integration_angles = np.linspace(0, 90, 91)
82 interpolated_values = interpolated_trans(integration_angles, T_a_b)
83
84 T_HEM = calc_T_HEM(T_a_b)
85
86
87 print("The␣Transmittance␣at␣0°␣AOI␣=",T_a_b[0])
88 print("The␣Transmittance␣at␣15°␣AOI␣=",T_a_b[1])
89 print("The␣Transmittance␣at␣30°␣AOI␣=",T_a_b[2])
90 print("The␣Transmittance␣at␣40°␣AOI␣=",T_a_b[3])
91 print("The␣Transmittance␣at␣45°␣AOI␣=",T_a_b[4])
92 print("The␣Transmittance␣at␣50°␣AOI␣=",T_a_b[5])
93 print("The␣Transmittance␣at␣60°␣AOI␣=",T_a_b[6])
94 print("The␣Transmittance␣at␣75°␣AOI␣=",T_a_b[7])
95 print("T_HEM␣=␣" + str(T_HEM))
96
97 plt.scatter(AOI,T_a_b/T_a_b[0], marker = 'x')
98 plt.plot(integration_angles,interpolated_values)
99
100
101 plt.xlabel("Angle␣of␣Incidence␣(degree)")
102 plt.ylabel("Transmittance␣(%)")
103 plt.legend()
104 plt.grid()
105 #plt.title(r"HLT measurement, only Optiwhite")
106 #plt.savefig('figures\measurement_optiwhite.pdf', dpi = 1000)
107
108 plt.show()
```